UNIVERSITY OF CALIFORNIA

SANTA CRUZ

INTERFACIAL ENGINEERING OF NANOPARTICLE SYSTEMS: ASSESMENT OF ELECTRON TRANSFER IN INTER AND INTRANANOPARTICLE PHOTOSYSTEMS AS WELL AS SENSING APPLICATIONS

A Dissertation submitted in partial satisfaction
of the requirements for the degree of

DOCTOR OF PHILOSOPHY

In

Chemistry

Bruce Drury Phebus

September 2015

The Dissertation of Bruce Drury Phebus
Is approved:

_____
Professor Dr. Shaowei Chen, Chair

_____
Professor Dr. Roberto Bogomolni

_____
Professor Dr. Jin Z. Zhang

_____
Dr. Tyrus Miller
Vice Provost and Dean of Graduate Studies

Table of Contents

LIST OF FIGURES

Chapter 2: Sensing Aqueous Cations Using Photo Emission from GQDs page

Chapter 4 Donor-Acceptor Intraparticle Transfer of Metal-Ligand Systems

List of Tables & Schemes

Dedication

I would like to dedicate this dissertation to so many but my time here started the love of my life, my wife. Though there are quite a number who deserve plenty of thanks and kudos for their assistance, all are well liked. She lent her strength of mind, body, and soul to my toil. I will be in her debt for all the years till I reach the soil. Not enough thanks can I distribute, garner, or even bestow. There isn't enough space in the heavens, God knows to write how much I am in debt. Her assistance in my prosperity, my fortune, and in my happiness can little be measured. I doubt I will ever fully appreciate and see; I hope this dedication though a small measure of courtesy can be a start of a lifetime of acknowledgement and thanks.

In addition I am sure she couldn't do it alone. My friends and family are more amazing than I deserve. I thank you all

ACKOWLEDGEMENTS

Appreciation for those that have with their guidance, critiques, suggestions, and time contributed to this work I can scarcely write. Professor Shaowei Chen has been more than welcoming my work in his lab. Providing guidance and insight where it is needed and often none where it was needed too, was something he did all too well. Being lost is part of finding your way around. I am thankful to my committee Professors Roberto Bogomolni and Jin Z. Zhang who have taken more than a few hours to read through and watch presentations to aid in my development. I would like to recognize those students who were trail blazers and helped to show me the way, Xiongwu Kang and Yang Song without whom I would have no idea where most things in the lab are to this day. Those colleagues who worked alongside me through grad school and gave me advice, listened to ideas and provided feedback, Jaclyn Schmitt, Ke Liu, Hanyu Wang, Chris Bailey, and Liat Zavodivker, you helped me through my classes and helped me study for them. Thanks go to Brian Lion who worked ever so hard to synthesize a ligand, though not successful the effort was amazing and I thank him.

Those that helped me mature and develop skills as a researcher and read and watched proposal talks. Chris Deming, your comments were ever so helpful. Peiguang Hu, Chen Limie, and Mauricio, Gabriella Jia-En Lu, Samantha Sweeney, Yi Peng, Rene Mercado, John M. Dinz, Mohammed Khan, Shannon Lee, you all listened to endless discussions and repeated talks with patience. To those that lent their skills and time directly with this work, Rick Perez, Corey Abraham, and Richard

DeLaCruz. You efforts were considerable, I thank you. To Chris Deming, Limei your assistance with spectra was invaluable. To members of the Zhang Lab for discussions on concepts and research, Damon Wheeler, Bob Fitzmorris, Staci Adams and Sarah Lindley, I thank you all. To members of the Li lab, Yi Yang, and Tianyu Liu I thank you for insightful conversations.

INTERFACIAL ENGINEERING OF NANOPARTICLE SYSTEMS: ASSESMENT OF ELECTRON TRANSFER IN INTER AND INTRANANOPARTICLE PHOTOSYSTEMS AS WELL AS SENSING APPLICATIONS

Abstract
Bruce Drury Phebus

Electron transfer within nanochemical systems plays a key role in their uses. This body of work looks to better understand the conditions required for electron transport within these nanochemical systems and under what circumstances does it play a role in their use.

Assessing electron transfer from aqueous graphene nanoparticles to aqueous ions through observation by quenching photoluminescence pointed to interesting requirements for transfer. Sensitivity was observed down to $1.6x10^{-6}$ M for the most strongly quenching ions. More interesting though was a marked dependence on chemical hardness of the ions, with specific chemical hardness required to quench each graphene quantum dot species. Graphene quantum dots sourced from carbon fiber were observed to quench best with ions near that of 8.50 eV chemical hardness, like that of nickelous ions. Nitrogen doped graphene quantum dots were observed to quench best with ions near 7.70 eV in chemical hardness, like that of mercuric ions. The shift to a lower hardness is also noted in a shift toward lower excitation energy of the nanoparticles. For some ions concentration dependence was observed, with ions increasing PL emission initially then subsequently acting as quenchers. This behavior points to multiple quenching sites on the nanoparticles with different complexation values, some leading to stabilization of the PL emission when complexed. EDTA, ethylenediaminetetraacetic acid, was used as a complexing agent to assess possible

recovery of emissions. EDTA was observed to complex ions and recovers some PL emission from some ions, with recovery dependent not only on quenching efficiency of the ion but the complexation constant. The most intriguing behavior was observed for aluminum ions which were observed to further quench with additions of EDTA, then after a critical point emission started to recover. We ascribe this behavior to multiple complexation sites on the nanoparticles with varied concentration and distinct roles in the emission of the nanoparticles.

Looking at inter nanoparticle electron transfer by assessing resistivity of nanoparticle films with varied exposure to solvent vapors. Carbon nanoparticles with notable graphitic character were produced from soot by burning sp2 rich fuels and utilized to selectively sense volatile solvent vapors. Dynamic light scattering and Transmission Electron Microscopy showed the particles to be significantly larger than those produced from other soot sources as well as most known bottom up methods for producing graphene nanoparticles. Raman measurements show considerable graphitic character with Raman G : D peak ratios greater than 1. Doping with nitrogen, undertaken by adding pyridine to the precursor fuel, also yielded a dopant levels of just over 3 % nitrogen, showing pyridine like character. The nitrogen doped particles showed strong specificity to sensing pyridine and piperidine vapors over those of the un-doped toluene soot nanoparticles which showed a strong response to ethanol and especially isopropanol over that of the doped nanoparticles. With the carbon chloride solvent series, carbon tetrachloride, chloroform, and dichloromethane, pyridine doped nanoparticles showed greatest sensitivity toward

dichloromethane with the undoped particles showing little response. In contrast to many other chemiresistor sensor systems, the particles show increasing conductivity when exposed to vapors displaying conductivities like those of some polymers and special cases of graphene oxide. Although these sensing systems are not optimized the remarkable specificity difference between the two different nanoparticle films due to the slight level of doping is illustrative of how a more diverse set of sensors might be made. Clear trends are present in polarity of the solvents and the current response of the sensors.

Assessing electron transfer within a single nanoparticle system was conducted using ruthenium nanoparticles stabilized by the self-assembly of 1-decyne forming ruthenium-vinylidene interfacial bonds and further functionalized by metathesis reactions with 4-ethynyl-*N*,*N*-diphenylaniline (EDPA) and 9-vinylanthracene (VAN). The surface concentrations of the EDPA and VAN ligands were quantified by proton NMR measurements of the organic components after the metal cores were dissolved by dilute potassium cyanide. Photoluminescence measurements showed that when both ligands were bound onto the nanoparticle surface where effective mixing of the π electrons occurred leading to the appearance of excitation and emission profiles that were completely different from those of ruthenium nanoparticles functionalized with only EDPA or VAN. Furthermore, in photoelectrochemical studies, the EDPA moieties exhibited a pair of well-defined voltammetric peaks in the dark that were ascribed to the redox reaction involving the formation of cationic radicals; yet under UV photoirradiation the voltammetric features diminished markedly. These results

strongly suggested that the particle-bound EDPA and VAN moieties behaved analogously to those of conventional molecular dyads based on the same electron-donating and –accepting units, where the intraparticle charge transfer might be facilitated by the conjugated metal-ligand interfacial bonds.

Chapter 1

Introduction

1.1 Introduction of Graphene Quantum Dots

As a rising star in the family of graphene, graphene quantum dots (GQDs) exhibit unique properties conferred by the two-dimensional sp^2 carbon matrix as well as the nanometer-sized quantum confinement and edge effects. Carbon quantum dots are similar in many respects, and the term is often used for particles that might have greater sp^3 character or be less perfectly determined in composition. Graphene quantum dots with significant oxidation can also be referred to as graphene oxide quantum dots, for the sake of simplicity, GQDs will be discussed using a single moniker and described from the GQD perspective. A brief introduction of GQDs will ground the reader in possible applications as well as previous research in this field prior to original research presented in Chapter 2.

Examples of these properties include a high specific surface area, bright photoluminescence (PL), excellent chemical inertness, biocompatibility, and low toxicity.[1-4] GQDs may be used in many fields, such as catalysis, sensing, biological imaging, drug delivery, and photovoltaics, to name a few.[5-8] Toward this end, ready preparation of soluble and luminescent GQDs represents a critical first step where further engineering and functionalization may be carried out. The primary approach to the synthesis of GQDs is based on the breakdown of graphene sheets through a controlled oxidation or reduction process. Bottom-up synthesis which starts with small aromatic precursor molecules to make larger sheet-like structures has also been realized, but the yield is in general low and the organic synthetic procedure is time-consuming and expensive. Within these GQDs, the presence of finite-sized

molecular sp^2 domains and/or CO-related quasi-molecular fluorophores, induced by adsorption of oxygen functional groups, may confine electrons and consequently determine fluorescence properties via the nature of the Csp^2 domains and functional groups on the quantum dots. For instance, Tetsuka *et al.* have synthesized amino-functionalized graphene nanoparticles with a tunable band gab of 420 to 450 nm, which is mainly ascribed to the limited tunability of size and/or shape of the sp^2 domains and adsorption of oxygen functional groups.[9] More recent theoretical and experimental studies show that the distinctive properties of graphene can be achieved by tuning the band gab by altering their size, such as manipulation of the size of the π system by controlling the chemical structures and/or layering of the graphene quantum dots.[10] The oxygen containing groups at the edge, such as carboxyl, hydroxyl, alcohol, and ether groups, impart strong solubility that allows for ease of processing and further functionalization with organic, and inorganic moieties to aid in catalysis or with polymeric and biological species to aid in sensing.[11] Processes that focus only on the insertion or removal of oxygen functional groups may have better luck tuning the HOMO-LUMO structure of the nanoparticles than methods based on size control. Nevertheless, due to the non-stoichiometric nature of GQDs it remains extremely challenging to control the optical properties, which forms one of the key technologies for putting these materials into practical use.[9]

In addition to surface functionalization, doping is an effective method in inducing change of the electronic structure in semiconductor materials, leading to controlled variation of the optical and electronic properties.[12] In the past few years,

many studies have been carried out focusing on the modulation of the GQDs properties. In this paper, we review the recent development in chemical functionalization of GQDs, such as doping with heteroatoms, surface functionalization, hybridization with metallic nanostructures, as well as assembly with other materials. In addition, we include a perspective on the critical issues for further investigation and of chemically functionalized GQDs.

1.2 Doping with Heteroatoms

In general, doping of carbon-based materials is difficult. However, it has proved to be a thriving area of research primarily because of the ability to modulate the electrical, optical, catalytic, and chemical properties of the materials.[13] Of this, doping graphene with heteroatoms, such as H, N, Cl, F and B, can effectively engineer the band gap and thus produce new phenomena and unexpected properties.[14]

Nitrogen-doped graphene quantum dots (N-GQDs) have received significant attention due to the ready manipulation of the electronic structure as compared to pristine carbon which may be exploited for diverse potential applications in, for instance, electrocatalysis, tunable photoluminescence and biocompatibility. In N-GQDs, chemically bonded N atoms introduces a new energy level in the electronic structure that dramatically alters the GQD HOMO-LUMO structure, tunes the optical properties and offers active sites for new chemical reactivity.[8, 13, 15]

A variety of approaches have been reported to produce N-GQDs, such as annealing and hydrothermal treatment of GQDs in the presence of nitrogen containing compounds to introduce nitrogen into defects sites both repairing the

graphitic structure and doping the material at the same time. Electrochemical reduction/oxidation in the presence of nitrogen containing compounds has also been found to replace oxidized carbons with nitrogen dopants embedded within the lattice.

N-doped graphene was first synthesized by annealing reduced graphene oxide (GO) in a tube furnace at 300 °C for 1 h in an ammonia atmosphere.[16] In another study, Qu *et al.*[10] electrochemically prepared N-GQDs with oxygen-rich functional groups at an N/C atomic ratio of about 4.3%. Unlike their green luminescent N-free counterparts, N-GQDs emitted blue luminescence due to the relatively strong electron-withdrawing ability of pyridinic-N and pyrrolic-N atoms in the N-GQDs; and they also possessed an electro-catalytic activity for oxygen reduction reactions (ORR). Highly blue-luminescent N-GQDs with a quantum yield of 24.6% have also been obtained by using hydrothermal treatment of GO in the presence of ammonia at 180 °C without strong acid or further surface modification.[17] In a more recent study, N-GQDs with a diameter of 1–7 nm and an N/C atomic ratio of ~5.6% were prepared by cutting N-doped graphene via a simple hydrothermal approach, and exhibited bright fluorescence with unique upconversion properties.[18]

In N-GQDs, active sites may be induced by defects and holes on the surface and N heteroatom functionalization, which allow for tailored PL and efficient catalytic activity in ORR in alkaline media. For instance, based on first-principles DFT calculations in conjunction with the SHE model, Saidi *et al.*[19] showed that graphitic nitrogen is the most active sites for reduction with overpotentials of 0.79-0.90 V and there is a correlation between the OH*, OOH*, and O* binding energies

which impose a lower limit on the overpotential of oxygen reduction. In another study, Li *et al.*[18] used a solution based organic chemistry approach to synthesize N-GQDs with well-defined structures. They demonstrated that there is a correlation between the catalytic activity and the size of the nanoparticles. However, the bonding configuration of the nitrogen dopants varied between a phenazine-like and anthracene-like functional group. Although the primary difference between the three particles generated was the size of the nanoparticles, the nitrogen substructure as well as the distance between the nitrogen dopants remained invariant.

In addition to their use as catalysts in fuel cell electrochemistry, N-GQDs also exhibit superior photoluminescence characteristics that allow them to be used in biomedical settings due to strong photo-catalyst activity and high depth penetration. Other possible uses include conversion and storage of energy and other optoelectronic applications. For instance, Liu *et al.*[20] used dimethylformamide (DMF) as both the solvent and nitrogen source to prepare N-GQDs, and found that the N-GQDs could be used as efficient two-photon fluorescent probes for cellular and deep-tissue imaging. In these N-GQDs, doping nitrogen induces strong electron donating groups in the forms of dimethylidio, amines, amides and others that are capable of electron donating through resonance, resulting in a red shift of the fluorescence emission, due increase in the HOMO energy level. The photons at longer wavelength (lower energy) are less scattered by biotissues and consequently more practical for imaging applications; and the large rigid π-conjugated electronic structure of GQDs can also

improve the intramolecular charge transfer efficiency and therefore enhance the two-photon absorption to achieve larger imaging depth in TPFI.[20]

In further studies, co-doping of GQDs by sulfur and nitrogen has been found to lead to unique PL that is markedly different from that of singly doped N-GQDs. For instance, Qu *et al.*[12] developed a facile hydrothermal route to the synthesis of S, N co-doped GQDs by using citric acid as the C source and urea or thiourea as the N and S sources, respectively. The resulting S, N co-doped GQDs were found to exhibit a high quantum yield of 71% and excitation-independent emission when the excitation wavelength was varied between 340 and 400 nm, and a single exponential decay under UV excitation. In contrast, when excited within the range of 420–520 nm, the PL emission color varied with the excitation wavelength, due to apparent absorption in the visible region. In fact, a broad absorption band could be identified in the visible region with the S, N co-doped GQDs which might be ascribed to the sulfur dopants that altered the surface states of GQDs.

The S, N co-doped GQDs may also be used for the preparation of effective photocatalysts. For instance, nanocomposites based on the S, N co-doped GQDs supported on TiO_2 exhibited apparent photocatalytic activity in the degradation of rhodamine B under visible light, also as observed by Sun *et al.*,[12] and the degradation rate was three times higher than that of N-GQD/TiO_2 and ten times higher than that of P25 TiO_2.

Whereas prior research is mostly focused on nitrogen doping of graphene derivatives other heteroatoms have also been used as dopants, such as F,[14] and B[21-22]

that exhibit high electronegativity. With the introduction of additional energy levels between the Cπ and Cπ* orbitals, the band gap of GQDs can be tuned accordingly, thus producing new optical and electronic properties.

The procedure of doping GQDs with other heteroatoms is similar to that discussed above for N-GQDs, such as the electrochemical and hydrothermal methods. For instance, water-soluble boron-doping of graphene quantum dots (B-GQDs) have been prepared by electrochemical exfoliation of graphite in a borax electrolyte ($Na_2B_4O_7 \cdot 10H_2O$), which exhibit rich fluorescence because of the introduction of highly electron-deficient B dopants and their peculiar interactions with surrounding carbons.[21] Experimentally it was observed that a borax solution of B-GQDs emitted apparent green fluorescence, and upon evaporation, formed bright green fluorescent crystals composed primarily of borax with imbedded GQDs. However, removal of the borax electrolyte left behind only a blue and yellow luminescent solution. The reason for the strong photoluminescence is that B-GQDs associate with one another in the absence of the isolating borax matrix. Within the borax salt they form dative valence bonds with the bridgehead O atoms of boron. These B-GQDs could be used as a chemosensor for detecting Al^{3+}, as well as a biomarker for cellular imaging.[21]

1.1.2 Functionalization of Surface and Edge Moieties

Surface and edge chemical functionalization has also proven to be a successful and effective approach to manipulating the PL properties of GQDs. Charge transfer between functional groups and the adjustment of the electronic structure provides a tuning of the GQDs band gap thus resulting in a shift of their PL

emission wavelength.[7] Although heteroatoms such as N, F, Cl, and B-doped GQDs exhibit tunable PL emission from their undoped counterparts, the incorporation of heteroatoms within the graphene lattice is challenging. Such insertion may disrupt the carbon sp^2 hybridization. Full control of GQD optical properties is still lacking, with regards of both the excitation wavelength and emission wavelengths. However, surface modulation of GQDs can not only effectively tune their photoluminescence emission, but also greatly improve their quantum yields, which mainly includes tuning surface oxidation, and surface functionalization with organic molecules.[7]

1.2 Reduced GQDs

1.2.1 Chemical Reduction

Surface oxidation/reduction reactions can be used to alter the photoluminescence properties and improve the optical performance of GQDs.[23-24] Feng, *et al.*[24] It has been found that the degree of reduction of the GQDs is critical for its properties. The amount of sp^2 carbon in GQDs can be controlled by varying the reduction time, which is useful for optimizing the electrical and optical properties. Kim *et al.*[25] report the synthesis of rGQDs and their applications in the preparation of bulk heterojunction (BHJ) in solar cells with enhanced power conversion efficiency (PCE). The results indicate enhanced optical absorptivity which is due to the rich functional groups in and on the GQDs leading to increased short-circuit current, while the improved conductivity of rGQDs led to an increase of the fill factor. Apparently, the extent of reduction of GQDs needs to be balanced for optimal absorptivity (short-circuit current, J_{sc}) and conductivity (fill factor, FF). Experimentally, partially

reduced GQDs yielded a power conversion efficiency (PCE) in BHJ devices that is superior to that of a reference device without GQDs.

1.2.2 Photochemical Reduction

Compared with conventional chemical reduction, photochemical reduction is a green approach, requiring no chemicals and easy to control via the wavelength, brightness, and duration of irradiation. Bright blue luminescent GQDs with high QY have been synthesized through a photoreduction pathway using alcohols as the reducing agent assisted by UV irradiation.[26] In addition, photochemical reduction is much faster (of the order of min) than traditional chemical reduction with $NaBH_4$ or $N_2H_4 \cdot H_2O$ that usually needs several hours. Furthermore, the prepared GQDs might be more biocompatible due to the lack of toxic reagents in the synthesis. Therefore, photochemical reduction looks to be used as an eco-friendly synthesis method for GQDs of high QY.

1.3 Chemically Modified GQDs

Whereas enhanced photoluminescence of GQDs by chemical reduction has been well known, the fundamental mechanism remains largely unclear at this time. Nevertheless, it is known that the O/C ratio is reduced.[24] Edge groups likely show less acidic character which may weaken quenching by water or ions in solution. Surface functionalization or modification is an alternative method by introducing functional groups onto the GQD surface of the GQDs, leading not only to tunneling and enhancement of the luminescence but also to manipulate the GQDs properties.[27] Note that GQDs are generally decorated with rich functional groups, such as

carboxylic acid moieties, ethers, aldehydes, phenols, esters, quinones, exoxides, azines, ethers, and others at the edge and at times within the structure. These functional groups impart excellent water solubility and allow for subsequent functionalization using these groups as precursors. Considering the extraordinary surface chemistry properties, GQDs could be further functionalized with various inorganic or organic species to build nanostructured functional materials for a variety of important applications.[28]

1.3.1 Inorganically Functionalized GQDs

GQDs functionalized with inorganic molecules are generally prepared by simple surface contact, conjugated bonding, and dative bonding. For instance, ZnO nanowire arrays functionalized GQDs(GQDs@ZnO NWs) have been prepared by anchoring GQDs on ZnO NWs and controlling the amount of GQDs.[28] First, ZnO NWs were modified with 3-aminopropyltriethoxysilane (APTES) to introduce amine groups on the surface, which were then covalently coupled with GQDs by carboxylic acid activation via ethyl(dimethylaminopropyl) carbodiimide/ *N*-hydroxysuccinimide (EDC/NHS) to produce a unique photoelectrode based on GQD-sensitized ZnO nanowire arrays (GQDs@ZnO). The corresponding photoelectrochemical cell, without any sacrificial agent, exhibited a significantly higher photo-induced open-circuit voltage and short-circuit current density than that based on an unmodified plain ZnO NW photoelectrode.

In another study, Cs_2CO_3 functionalized GQDs (GQDs–Cs_2CO_3) were used as efficient electron-selective layers in inverted polymer solar cells (iPSCs).[29] In this set

up the Cs^+ ion is adsorbed on the GQD surface. Compared with Cs_2CO_3 buffered devices, the GQDs–Cs_2CO_3 buffered devices show 56% improvement in power conversion efficiency, as well as 200% enhancement in stability, due to improved electron-extraction and suppression of leakage current. The immobilization of Cs^+ ions in GQDs–Cs_2CO_3 retards the Cs^+ ion diffusion into the polymer layer and thus improves the device stability.

In addition, graphene has been shown to conjugate with layered protonated titanate (LPT) and to form nanoflowers (GQDs-LPT). These structures look to be promising systems for drug delivery with innate photoluminescence.[30] The high specific area for the nanoflowers could lead to significant surface loading for drugs, coupled with GQD's as covalently bound fluorophores for tracking purposes.

1.3.2 Polymer-Functionalized GQDs

Polymers have also been used to functionalize GQDs. The typical synthetic routes include (i) ligand exchange between polymers and GQDs; (ii) polymers grafted to/from GQDs; (iii) GQDs capped with polymers; or (iv) GQDs grown within a polymer template.[31] These routes can be divided into two types: surface passivation of GQDs by polymers and simple hybridization of GQDs with polymers.

1.3.3 Surface Passivation of GQDs by Polymers

It have been shown that surface passivation of GQDs by polymers can enable them to become strongly fluorescent in the visible and near-infrared spectral regions. Many organic polymers have been used to both enhance the photoluminescence and passivate the surface of GQDs, such as poly(ethylene glycol) (PEG), poly(propionylethyleneimine-co-ethyleneimine) (PPEI-EI), chitosan, heparin, poly(acrylic acid) (PAA) and polydopamine (PDA), etc.[32] Of these, GQDs functionalized with PEG have been studied extensively. Surface-passivated For instance, GQDs with oligomeric PEG diamine (PEG_{1500N}) have been synthesized by a three-step method.[33] Oxidation and breakdown of GO into GQDs was the first step using HNO_3. This precursor GQD solution was then surface-passivated by PEG, and lastly reduced by hydrazine hydration generating rGQDs. The PEG-functionalized GQDs (PEG-GQDs) showed strong blue and green emission under the excitation at 365 nm or using a 980 nm laser, respectively. The former might be ascribed to a band-gap transition, while the up-conversion emission of GQDs was similar to that of anti-Stokes PL. Evidence for this include the static energy difference between the excitation and emission energies.

In another study, PEG-GQDs were prepared by connecting the hydroxyl groups (–OH) of PEG to the carboxyl groups (–COOH) of GQDs,[33] which showed strong blue PL under 365 nm with a quantum yield of about 28.0%, as well as up-conversion PL under a fluorescence microscope with emission centered at 464 nm

when excited with an 808 nm laser. Furthermore, the PEG-GQDs appears to have higher photon-to-electron conversion capability compared with unpassivated GQDs.

PEG-GQDs can also be used as drug carriers and cell imaging reagents. The surface-passivation of PEG on GQDs can not only enhance the PL intensity but also improve solubility and provide surface sites for a high loading capacity (2.5 mg / mg) for drugs via hydrogen bonding,[32] thanks to the high surface area.

Polydopamine-functionalized GQDs (PAD-GQDs) were mussel-inspired and have also been used as a biocompatible drug carrier by Nurunnabi *et al.*[34] Introduction of PDA to GQDs helped to interconnect them with each other. The results showed excellent stability of the PL intensity. The stability of GQDs that remained uncoated in the PBS solution rapidly lost fluorescence with time by 45% over 14 days. After coating with PDA, the GQD emission intensity remained markedly stable over the same 14 days. Possible applications of the PDA-GQDs involved biocompatible imaging agents as well as a drug carrying vector.

1.4 GQDs Hybrids with Polymers

Compared to chemical functionalization by surface-passivation with polymers, GQDs hybrids with polymers are much simpler. Hybrid composites can also tune the photo- and electroluminescence of GQDs for enhanced practical applications. For instance, to prepare a hybrid composite material consisting of GQDs embedded in a polymeric matrix such as poly(ethyleneglycol)bis(carboxymethyl) ether, GQDs were first synthesized via a microwave assisted hydrothermal process and were subsequently mixed with water and poly(ethyleneglycol)bis(carboxymethly)

ether.[31] Experimental results revealed that the GQDs were evenly dispersed inside of the polymeric matrix. The obtained GQDs–PEG_{600} showed excitation wavelength-dependent photoluminescence. When compared with self-passivated GQDs the composite exhibited a blue shift and broadening of the PL emission which might involve additional emission peaks in the range of 570–600 nm. Mihalache *et al.* proposed that these features might be explained by the appearance of new electronic states induced at the surface by the polymeric matrix surrounding the GQDs. Such a switching property may be exploited for nonvolatile memory applications.

Memory devices based on other GQD–polymer hybrids have also been made by using an insulating polymer, polymethyl methacrylate (PMMA), as the host material for the GQDs,[35] which exhibited a nonvolatile, rewritable, and repeatable memory effect with an applied bias voltage.

Notably GQDs–polymer hybrids can be synthesized by simple mixing or doping methods. For instance, GQDs–polymer composite materials may be prepared by simple mixing of GQDs with a water-soluble dual-responsive (pH and temperature), polythiophene (PT) graft copolymer, polythiophene-g-poly[(diethylene glycolmethylethermethacrylate)-co-poly(N,N-dimethylaminoethylmethacrylate)].[36] The carboxyl groups (–COOH) of GQDs were attached to the dimethylamino groups of the polymer chains, leading to quenching of the fluorescence by an energy transfer process, and a delayed up-converted emission of GQDs began to show a gradual increase of the PL intensity with increasing aging time. In addition, these

nanocomposites exhibited strong photoconductivity and with the polymer matrix they have enhanced cell viability as well.[36]

In another study, GQDs doped polypyrrole (GQDs-PPy) was synthesized as a counter electrode for high-performance dye-sensitized solar cells via an electrochemical codeposition method.[7] GQDs could electrostatically absorb Py as nucleation sites to promote the PPy growth, resulting in many "nano-islands" for a highly porous structure. The porous GQD-doped PPy counter electrode showed an apparent increase of the electrocatalytic active centers and enhanced reactant diffusion for improved electrode kinetics and thermodynamics.

1.5 GQD Functionalized With Small Organic Molecules

1.5.1 Amine-Functionalized GQDs.

The amine-functionalized method is commonly applied to modify graphene-based materials, which effectively decreases the surface defects for fluorescence enhancement. It has been demonstrated that small amine compounds, when employed as passivation agents to modify GQDs, resulted in increasing emission efficiencies of the GQDs.[23,27] These particles are extracted through an ammonia-mediated bond-scission reaction from precursor GO. The af-GQDs show multiple emission colors under a single-wavelength UV excitation. With a quantum yield over 40%, the optical properties are precisely controlled only by the quantitative functionalization of the af-GQDs.[9] With discrete particle configurations, fully tuned GQDs could have powerful applications in LED devices as well as photovoltaic and biological sensing applications.

The effects of surface chemistry on GQDs and its PL mechanism were investigated through modification or reduction,[23] where the GQDs emission changed from green to blue. The experimental results demonstrated that the carboxylic and epoxy groups of the GQDs changed into –CONHR and –CNHR in these modified GQDs (m-GQDs). During modification with alkylamines GQDs with carbonyl, epoxy and amido moieties were converted into –OH groups in r-GQDs. As a result, the non-radiative recombination of localized electron-hole pairs decreased and the integrity of the surface π electron network was enhanced, which proved that the intrinsic state emission played a key role in the preparation of GQDs. The results of time-resolved measurements were also consistent with the suggested PL mechanism. The up-conversion PL of GQDs can be successfully applied in near-IR excitation for bioimaging using two or multiphoton luminescence.[11] In fact, Jiang *et al.*[37] found that af-GQDs could be used in bioimaging by size control of GQDs through functionalization with amines using hydrogen peroxide and ammonia as starting materials. In the synthesis hydrogen peroxide cuts GO into GQDs and ammonia passivates the resulting GQDs. Notably, the af-GQDs were observed to possess superior antimycoplasma activity which was comparable to commercial BM0Cyclin.

af-GQDs can also be used as fluorescent probes for Cu^{2+} sensing, as reported recently.[38] Before hydrothermal treatment in ammonia, the GQDs showed greenish-yellow fluorescence with a low quantum yield of 2.5%; and after treatment they were converted to amino-functionalized GQDs (af-GQDs) with a high QY of 16.4%. With Cu^{2+} ions having a high binding affinity to N and O on the surface of af-GQDs as

compared to other transition-metal ions with improved kinetics, the selectivity of af-GQDs for Cu^{2+} is higher than that of unmodified GQDs. With biocompatibility, they were also promising tags for in situ sensing.

1.5.2 Other Small Organic Molecules

Other small organic molecules used to functionalize GQDs include aryl derivatives (such as phenyl, 4-carboxyphenyl, 4-sulfophenyl and 5-sulfonaphthyl), pyrrole, alcohols, thiols, and so on. GQDs modified with different aryl groups, including phenyl, 4-carboxyphenyl, 4-sulfophenyl and 5-sulfonaphthyl, was synthesized via the Gomberg–Bachmann reaction.[39] The aryl-modified GQDs were nanocrystals with lateral dimensions in the range of 2–4 nm, and an average thickness < 1 nm. Modification of the GQDs through the addition of aryl groups changes the functional groups at the edge that protect the PL activity. More importantly, because of the resonance effects between the aryl groups and graphene basal planes, the PL bands of GQDs might be systematically tuned with their fluorescence quantum yield and pH tolerance greatly improved.

Surface functionalization of GQDs with small organic molecules also showed low toxicity that is comparable to that of the pristine counterpart, thus they can be used in bioimaging, biosensing and other biomedical fields. Examples include 3,9-dithia-6-monoazaundecane functionalized GQDs (DMA-GQD) was used to detect Pb^{2+} with high sensitivity and selectivity.[40] GQDs produced from polycyclic aromatic hydrocarbons have also been reported by Zhou *et al.* which were used in bioimaging as well as sensing of Fe^{3+} and hydrogen peroxide through quenching of the GQD

PL.[41] GQDs functionalized with 3-aminobenzeneboronic acid (APBA-GQDs) resulted in nanoparticles with extraordinary brightness at QY ~49.7%, that were utilized for selective sensing of glucose.[42] APBA-GQDs were selective for glucose as compared to six other sugars tested: D-fructose, mannose, galactose, sucrose, lactose and maltose. The minimum detection limit was estimated to be as low as 5.0 μM which is enough to detect glucose in microdialysate. In other studies, Peptide–GQD Conjugates were prepared as effective optical probes for the profiling of kinase (casein kinase II (CK2)) activity based on a Zr^{4+}-mediated signal transition.[43] Direct covalent bonding of a peptide to GQDs activated the GQDs after phosphorylation by CK2, and Zr^{4+} ions were introduced to serve as a linkage between the phosphorylated peptides via coordination interactions. The Zr^{4+} ions and phosphate groups then aggregated the GQDs and effectively quenched the PL of the particles. Due to the high sensitivity of PL and strong dynamic range of PL systems high sensitivity was achieved for kinase sensing.

The photoluminescence of most GQDs reported to date is through single photon excitation in the (near)ultraviolet region, which is harmful to living cells. Developing visible-light or near-IR excitable GQDs is critically needed in biolabeling research. Also at issue is emission which usually falls into the visible range, whereas emission in the near IR is needed for deep tissue imaging applications.

In another study, pyrrole-functionalized GQDs (p-GQDs) were prepared by Chen *et al.* by a two-step hydrothermal approach with heating by microwave irradiation and the GQDs immersed in an ammonia medium.[7] The most distinct

feature of the functionalized GQDs is that both the excitation and emission wavelengths are in the visible region. The photoluminescence emission of the p-GQDs is reported at 550 nm when excited at λ_{ex} 490 nm, giving rise to an emission within the visible-light region. Most importantly, the PL emission of these p-GQDs is excitation-independent and fairly stable within a wide range of pH 4–10 and in the presence of an ionic strength of 1.2 M KCl. It should be noted that quenching due to other ions was not tested. With ionic and pH stability, the p-GQDs could make excellent probes for bio-imaging and bio-labeling, which Chen *et al.* demonstrated by imaging live HeLa cells.

In order to investigate the mechanism of luminescence enhancement of such functionalized GQDs and compare the effects of different small functional groups on the GQD properties, Qian *et al.*[27] prepared a series of functionalized GQDs with amines, diamines, dialcohols and dithiols, and compared their photoluminescence, cell toxicity and bioimaging applications. The precursor GQDs were synthesized through oxidation by acid then purified by dialysis. The resultant nanoparticles displayed bright green fluorescence. After functionalization with 1,2-ethylenediamine the PL of the GQDs was noted to shifted to the blue and the QY improved to 17.6 %. In contrast, GQDs functionalized with dithioglycol showed slight QY enhancement relative to the precursor GQDs. These observations indicate that amino groups play a key role in the improvement of the PL efficiency. GQDs functionalized with diamine showed a strong correlation with the carbon chain length. Comparing 1,2-ethylenediamine to 1,4-butanediamine, one may notice that increasing

chain length improved the PL properties although all functionalized GQDs were noted to have improved PL properties compared to the precursor GQDs. So they speculated that amino groups likely acted to enhance the PL efficiency. Experiments also showed that protonated 1,2-ethylenediamine could transfer protons from the funtionalizing amines to the GQD matrix leading to enhanced PL emission. Biological experiments demonstrated that GQDs functionalized with 1,2-ethylenediamine showed low toxicity and enhanced PL for bioimaging.

1.6 GQDs in Biological Systems

1.6.1 GQDs Functionalized with Biological Molecules

Glutathione-functionalized GQDs (GSH-GQDs) were synthesized in one step using pyrolysis of citric acid (CA) and glutathione (GSH) as precursors in one pot.[44] This synthesis approach was noted to have two advantages, improved QY of 33.6 % with blue emission and improved bio-compatibility. Liu *et al.* demonstrated that they could sense adenosine triphosphate (ATP) in vitro.[44]

In addition to direct functionalization with small molecules, GQDs can also be modified by co-reacting or anchoring with other biomolecules. Hyaluronic acid (HA) has been anchored to GQDs to synthesize HA-functionalized GQDs (HA-GQDs),[45] which showed apparent PL activity and allowed subsequent binding to the CD44 receptor, hyaluronan, with high affinity. The in vitro model of balb/c female mice and A549 cells manifested bright PL as compared to normal cells. HA-GQDs nanoparticles were tested, both in vivo and in vitro, and results showed that HA was

capable of targeting tumor cells. Subsequently the prepared HA-GQDs were tested as a drug carrier.

GQDs-based composites have usually been developed as fluorescent sensors for the detection of chemicals. Fluorescent sensor based on GQDs imprinted into a polymer exhibited a detection limit of 9 ng/ml for the sensing of paranitrophenol in water and was noted to have good linearity between 0.02-3.00 μg/mL.[46] A silica-coating was applied to the GQDs to combine its chemical inertness as well as binding affinity for analytes. The silica-coated GQDs were fabricated using GO reacted to form acid chloride functional groups then treated with 3-aminopropyltriethooxysilane and triethylamine. The composite used as sensors by attaching the silica coated GQDs were imprinted with paranitrophenol and irradiated yielding the imprinted polymer sensor. The final sensor was noted to have selectivity to paranitrophenol. The mechanism was speculated to be due to GQDs that transferred excitons to paranitrophenol which acted as quenchers.

With bright and tunable PL, GQDs have the potential to act as effective components for electrochemiluminescence (ECL) devices, as well as luminophores sensor, due to high specific surface area and abundant surface states. Dong *et al.* developed a coreactant ECL sensor using single-layer GQDs as well as L-cysteine (L-Cys) as a sensitizer to detect Pb^{2+} with a limit of 70 nM and a linear dynamic range of 100 nM to 10 μM.[47] The sensor worked by utilizing a cathodic current to induce ECL and achieve high sensitivity that was pH sensitive.

1.6.2 GQDs Noncovalent Functionalization

The above GQD functionalization mainly relies on covalent interactions with species bound directly to the carbon matrix of the GQDs. Functionalization can also be achieved by noncovalent interactions. When organic molecules are covalently bound to the surface of GQDs, the extended aromatic character will be perturbed resulting in changes in the optical and electrical properties. Noncovalent functionalization by π-interactions will have minimal effect on the electronic network making it attractive for systems where retention of the graphitic characteristics is needed.[48] For instance, a fluorescence-based sensing platform was constructed by noncovalent assembly of hemin on GQDs through electrostatic and π–π stacking interactions, which exhibited a good dynamic range and good lower limit of detection.[41] With the aid of hemin, H_2O_2 could destroy the passivated surface of GQDs and subsequently quench the PL signal. As the FL quenching of hemin-functionalized GQDs was dependent on H_2O_2 concentration, a label-free, green and simple FL biosensor was established for the determination of H_2O_2 and glucose.[48]

1.7 Hybrid with Metal and Metallic Compounds

1.7.1 GQDs Combined With Metals

Gold and silver nanoparticles have been known to strongly influence the optical properties of fluorophores interacting with the metallic nanoparticles. Enhancement of the photoluminescence will depend on the size, shape and composition of the metallic nanoparticle as well as their proximity to the flourophores. Gold nanocubes (AuNCs) have been used as metal cores for GQDs to

study possible fluorescence enhancement. The structures synthesized by Deng *et al.* consisted of a AuNC core overcoated with a silica shell, followed by a dense layer of GQDs.[49] Controlling the thickness of the silica coating was the primary means of tuning the interaction between the GQDs and the metallic core. Similar to classical fluorophores, the GQDs were observed to show enhanced emission when close to the core. The prepared AuNCs@SiO_2@GQDs were then functionalized with epidermal growth factor receptor which allowed specific visualization of the nanoparticles on cancer cells.

The fluorescence of GQDs in solution can be quenched by metals making them possible sensitizers. Metals such as (in atomic order): Na[40], Mg[40], K[40], Ca[40], Sc[1], Cr[1], Mn[1, 40], Fe[1, 40], Co[1, 40], Ni[1, 40], Cu[1, 40], Zn[1], Ru[1], Ag[1, 40, 50], Cd[1, 40], Eu[51], Hg[1, 40], & Pb[40]. It is speculated that sp^2 dangling bonds at defect sites are responsible for the trap states and hence, emissive. Interaction with the ion allows for transfer of the excited electron to the acceptor ion. It is noted that to act as a good quencher partly filled d orbitals are needed to act as acceptors. Ions with fully filled orbitals were not observed to act as quenchers.

On the other hand, if a chemical can restore the PL of GQDs by competition with GQDs for the metal ions, then it can also be detected by a reverse PL sensor. For example, GQDs can be utilized to sense europium ions through quenching of the GQD photoluminescence by Eu^{3+} and restored by phosphate. The lanthanide ion was noted as likely coordinating with multiple GQDs aggregating them as observed by AFM and thus inhibiting emission. With the addition of phosphate the GQDs were

outcompeted, and aggregation was reversed, as observed by AFM, leading to recovery of the GQD photoluminescence. This is ascribed to the strong affinity of phosphate for Eu^{3+} with its oxygen-donor atoms as compared to the carboxylate groups located at the edge of the GQD.[51]

1.7.2 GQDs-Supported Metallic Nanoparticle Composites

Reports of synergistic effects electro catalytic applications for carbon-based materials can be provided by graphitic carbon surfaces. An example of graphitic carbon used in this manner was done by Hou *et al.* produce GQDs–Au nanoparticles multilayers–modified glassy carbon electrode were fabricated to detect malachite green (MG). Its preparation involved two steps: (1) Electrodes were modified with GQDs and (2) electrodes were electrodeposited with Au nanoparticles in a $HAuCl_4$ solution. By layer-by-layer methods, the anodic potential of MG was reduced and the anodic current was obviously increased.[52]

GQDs were used as a support for metallic nanoparticles due to the large surface area, leading to effective enhancement of the electrocatalytic activity. These hybrid structures are important to various emerging technologies. Spectroscopic studies have shown covalent nature of the interactions between metallic nanoparticles and GQDs.[29] In a recent study, it has been shown that effective cathode catalysts for oxygen reduction might be prepared by platinum nanoparticles supported on GQDs (Pt/GQDs).[53] GQDs were prepared by acid etching of carbon fibers and used as effective substrate supports for Pt nanoparticles which were synthesized by thermolytic reduction of platinum(II) chloride in ethylene glycol. The prepared

Pt/GQDs nanocomposites exhibited a markedly enhanced electrocatalytic performance with a more positive onset potential, higher specific activity as well as stability than leading commercial Pt/C catalysts.

Composites of GQDs and magnetite nanoparticles were prepared by Wu *et al.*[54] in a one-step co-precipitation by dropwise addition of ferric salts to GQDs in an ammonium hydroxide solution. The resultant composites showed strong "peroxidase-like" activity due to unique synergistic properties between the GQDs and magnetite.[32] The resultant composite showed higher stability and was more robust than natural peroxidases. When the GQDs/Fe_3O_4 was used for removal of phenolic compounds in aqueous solutions, it showed promising efficiency as compared to native horseradish peroxidase. With such a strong catalytic activity in hand and a simplistic synthesis it is possible to utilize this composite in industrial applications for wastewater cleanup.

In another study, the composites of GQDs, Fe_3O_4, and apoferritin-encapsulated Cu (Cu-apoferritin) were developed as electroactive probes for ultrasensitive detection of avian leukosis virus subgroup J (ALVs-J).[55] GQDs were utilized for their strong interaction with amino functionalized magnetites as well as for ease of subsequent functionalization with ALVs-Jantibodies (Ab_1) and Cu-apoferritin and bovine serum albumin. Once the Fe_3O_4@GQDs nanoparticles were functionalized, the nanoparticles were subsequently immobilized by virus particles (ALVs-J) as well as secondary ALVs-Jantibodies (Ab_2). Wang *et al.*[55] further utilized Cu-apoferritin nanoparticles to increase the loading of electroactive compounds further amplifying the signal.

In addition to electrocatalytic performance, the hybrid of GQDs and metal nanoparticles also possess photocatalytic activity in solar cells. A variety of photocatalytic systems have been designed, e.g., TiO2 nanotube array and CdS-modified TiO2 nanotube arrays (CdS/ TiO2-NA) with GQDs anchored inside, were prepared through a facile impregnation method.[56] The evaluation of the activity showed the rate of hydrogen evolution during photocatalytic water splitting was greatly improved after loading GQDs into TiO2-NA and CdS/TiO2-NA. GQDs weaken the effect of light-filtering and simultaneously maintain the charge separation function. The morphology of the TiO2 nanotube arrays was well maintained after functionalization with GQDs, which is important for high diffusion. The hybrids of GQDs and ZnO nanowires (NWs) might also be used in photovoltaic devices, exhibiting an open circuit voltage of 0.8 V.[57] Hybrids of GQDs and cesium carbonate (Cs2CO3) were used as an additive to buffer iPSC on the cathode, due to a well matched band gap with ~3.3 eV and modified indium tin oxide at 3.8 eV. The HOMO level of [6,6]-phenyl- C61-butyricacidmethylester (3.7 eV) could also act as an efficient sensitizer.[58] For example, with Cs2CO3 as a buffer layer, the photo conversion efficiency of GQDs–Cs2CO3 hybrids showed 22% improvement up from 2.59% to 3.17%, which was attributed to enhanced exciton dissociation and suppressed recombination.

1.9 References

1. Huang, F.; Xu, P.; Liang, H., Using dual-polarization interferometry to study surface-initiated DNA hybridization chain reactions in real time. *Biosensors and Bioelectronics* **2014,** *51* (0), 317-323.

2. Chong, Y.; Ma, Y.; Shen, H.; Tu, X.; Zhou, X.; Xu, J.; Dai, J.; Fan, S.; Zhang, Z., The in vitro and in vivo toxicity of graphene quantum dots. *Biomaterials* **2014,** *35* (19), 5041-8.

3. Yamijala, S. S. R. K. C.; Bandyopadhyay, A.; Pati, S. K., Electronic properties of zigzag, armchair and their hybrid quantum dots of graphene and boron-nitride with and without substitution: A DFT study. *Chem Phys Lett* **2014,** *603* (0), 28-32.

4. Zhao, M.; Yang, F.; Xue, Y.; Xiao, D.; Guo, Y., A time-dependent DFT study of the absorption and fluorescence properties of graphene quantum dots. *Chemphyschem* **2014,** *15* (5), 950-7.

5. Al-Ogaidi, I.; Gou, H.; Aguilar, Z. P.; Guo, S.; Melconian, A. K.; Al-kazaz, A. K. A.; Meng, F.; Wu, N., Detection of the ovarian cancer biomarker CA-125 using chemiluminescence resonance energy transfer to graphene quantum dots. *Chem Commun* **2014,** *50* (11), 1344-1346.

6. Benítez-Martínez, S.; Valcárcel, M., Graphene quantum dots as sensor for phenols in olive oil. *Sensors and Actuators B: Chemical* **2014,** *197* (0), 350-357.

7. Chen, S.; Hai, X.; Xia, C.; Chen, X. W.; Wang, J. H., Preparation of excitation-independent photoluminescent graphene quantum dots with visible-light excitation/emission for cell imaging. *Chemistry* **2013,** *19* (47), 15918-23.

8. Ju, J.; Chen, W., Synthesis of highly fluorescent nitrogen-doped graphene quantum dots for sensitive, label-free detection of Fe (III) in aqueous media. *Biosens Bioelectron* **2014,** *58*, 219-25.

9. Tetsuka, H.; Asahi, R.; Nagoya, A.; Okamoto, K.; Tajima, I.; Ohta, R.; Okamoto, A., Optically Tunable Amino-Functionalized Graphene Quantum Dots. *Adv Mater* **2012,** *24* (39), 5333-5338.

10. Li, Y.; Zhao, Y.; Cheng, H.; Hu, Y.; Shi, G.; Dai, L.; Qu, L., Nitrogen-Doped Graphene Quantum Dots with Oxygen-Rich Functional Groups. *J Am Chem Soc* **2012,** *134* (1), 15-18.

11. Lin, L.; Rong, M.; Luo, F.; Chen, D.; Wang, Y.; Chen, X., Luminescent graphene quantum dots as new fluorescent materials for environmental and biological applications. *TrAC Trends in Analytical Chemistry* **2014,** *54* (0), 83-102.

12. Qu, D.; Zheng, M.; Du, P.; Zhou, Y.; Zhang, L.; Li, D.; Tan, H.; Zhao, Z.; Xie, Z.; Sun, Z., Highly luminescent S, N co-doped graphene quantum dots with broad visible absorption bands for visible light photocatalysts. *Nanoscale* **2013,** *5* (24), 12272-12277.

13. Tang, L.; Ji, R.; Li, X.; Teng, K. S.; Lau, S. P., Energy-level structure of nitrogen-doped graphene quantum dots. *J Mater Chem C* **2013,** *1* (32), 4908-4915.

14. Feng, Q.; Cao, Q.; Li, M.; Liu, F.; Tang, N.; Du, Y., Synthesis and photoluminescence of fluorinated graphene quantum dots. *Appl Phys Lett* **2013,** *102* (1), 013111.

15. Li, Y.; Zhao, Y.; Cheng, H.; Hu, Y.; Shi, G.; Dai, L.; Qu, L., Nitrogen-Doped Graphene Quantum Dots with Oxygen-Rich Functional Groups. *Journal of the American Chemical Society* **2011,** *134* (1), 15-18.

16. Agapito, L. A.; Kioussis, N.; Kaxiras, E., Electric-field control of magnetism in graphene quantum dots: \textit{Ab initio} calculations. *Phys Rev B* **2010,** *82* (20), 201411.

17. Hu, C.; Liu, Y.; Yang, Y.; Cui, J.; Huang, Z.; Wang, Y.; Yang, L.; Wang, H.; Xiao, Y.; Rong, J., One-step preparation of nitrogen-doped graphene quantum dots from oxidized debris of graphene oxide. *J Mater Chem B* **2013,** *1* (1), 39-42.

18. Li, M.; Wu, W.; Ren, W.; Cheng, H.-M.; Tang, N.; Zhong, W.; Du, Y., Synthesis and upconversion luminescence of N-doped graphene quantum dots. *Appl Phys Lett* **2012,** *101* (10), 103107.

19. Saidi, W. A., Oxygen Reduction Electrocatalysis Using N-Doped Graphene Quantum-Dots. *The Journal of Physical Chemistry Letters* **2013,** *4* (23), 4160-4165.

20. Liu, Q.; Guo, B.; Rao, Z.; Zhang, B.; Gong, J. R., Strong Two-Photon-Induced Fluorescence from Photostable, Biocompatible Nitrogen-Doped Graphene Quantum Dots for Cellular and Deep-Tissue Imaging. *Nano Lett* **2013,** *13* (6), 2436-2441.

21. Fan, Z.; Li, Y.; Li, X.; Fan, L.; Zhou, S.; Fang, D.; Yang, S., Surrounding media sensitive photoluminescence of boron-doped graphene quantum dots for highly fluorescent dyed crystals, chemical sensing and bioimaging. *Carbon* **2014,** *70* (0), 149-156.

22. Zhang, Y.; Wu, C.; Zhou, X.; Wu, X.; Yang, Y.; Wu, H.; Guo, S.; Zhang, J., Graphene quantum dots/gold electrode and its application in living cell H2O2 detection. *Nanoscale* **2013,** *5* (5), 1816-1819.

23. Zhu, S.; Zhang, J.; Tang, S.; Qiao, C.; Wang, L.; Wang, H.; Liu, X.; Li, B.; Li, Y.; Yu, W.; Wang, X.; Sun, H.; Yang, B., Surface Chemistry Routes to Modulate the Photoluminescence of Graphene Quantum Dots: From Fluorescence Mechanism to Up-Conversion Bioimaging Applications. *Advanced Functional Materials* **2012,** *22* (22), 4732-4740.

24. Feng, Y.; Zhao, J.; Yan, X.; Tang, F.; Xue, Q., Enhancement in the fluorescence of graphene quantum dots by hydrazine hydrate reduction. *Carbon* **2014,** *66* (0), 334-339.

25. Kim, J. K.; Park, M. J.; Kim, S. J.; Wang, D. H.; Cho, S. P.; Bae, S.; Park, J. H.; Hong, B. H., Balancing Light Absorptivity and Carrier Conductivity of Graphene Quantum Dots for High-Efficiency Bulk Heterojunction Solar Cells. *Acs Nano* **2013,** *7* (8), 7207-7212.

26. Sun, H.; Wu, L.; Gao, N.; Ren, J.; Qu, X., Improvement of Photoluminescence of Graphene Quantum Dots with a Biocompatible Photochemical Reduction Pathway and Its Bioimaging Application. *ACS applied materials & interfaces* **2013,** *5* (3), 1174-1179.

27. Qian, Z.; Ma, J.; Shan, X.; Shao, L.; Zhou, J.; Chen, J.; Feng, H., Surface functionalization of graphene quantum dots with small organic molecules from photoluminescence modulation to bioimaging applications: an experimental and theoretical investigation. *Rsc Adv* **2013,** *3* (34), 14571-14579.

28. Guo, C. X.; Dong, Y.; Yang, H. B.; Li, C. M., Graphene Quantum Dots as a Green Sensitizer to Functionalize ZnO Nanowire Arrays on F-Doped SnO2 Glass for Enhanced Photoelectrochemical Water Splitting. *Adv Energy Mater* **2013,** *3* (8), 997-1003.

29. Yang, H. B.; Dong, Y. Q.; Wang, X.; Khoo, S. Y.; Liu, B., Cesium carbonate functionalized graphene quantum dots as stable electron-selective layer for improvement of inverted polymer solar cells. *ACS applied materials & interfaces* **2014,** *6* (2), 1092-9.

30. Zheng, X. T.; He, H. L.; Li, C. M., Multifunctional graphene quantum dots-conjugated titanate nanoflowers for fluorescence-trackable targeted drug delivery. *Rsc Adv* **2013,** *3* (47), 24853-24857.

31. Mihalache, I.; Radoi, A.; Munteanu, C.; Kusko, M.; Kusko, C., Charge storage and memory effect in graphene quantum dots – PEG600 hybrid nanocomposite. *Organic Electronics* **2014,** *15* (1), 216-225.

32. Wang, Z.; Xia, J.; Zhou, C.; Via, B.; Xia, Y.; Zhang, F.; Li, Y.; Xia, L.; Tang, J., Synthesis of strongly green-photoluminescent graphene quantum dots for drug carrier. *Colloids and Surfaces B: Biointerfaces* **2013,** *112* (0), 192-196.

33. Shen, J.; Zhu, Y.; Yang, X.; Zong, J.; Zhang, J.; Li, C., One-pot hydrothermal synthesis of graphene quantum dots surface-passivated by polyethylene glycol and their photoelectric conversion under near-infrared light. *New J Chem* **2012,** *36* (1), 97-101.

34. Nurunnabi, M.; Khatun, Z.; Nafiujjaman, M.; Lee, D.-g.; Lee, Y.-k., Surface Coating of Graphene Quantum Dots Using Mussel-Inspired Polydopamine for Biomedical Optical Imaging. *ACS applied materials & interfaces* **2013,** *5* (16), 8246-8253.

35. Kou, L.; Li, F.; Chen, W.; Guo, T., Synthesis of blue light-emitting graphene quantum dots and their application in flexible nonvolatile memory. *Organic Electronics* **2013,** *14* (6), 1447-1451.

36. Routh, P.; Das, S.; Shit, A.; Bairi, P.; Das, P.; Nandi, A. K., Graphene Quantum Dots from a Facile Sono-Fenton Reaction and Its Hybrid with a Polythiophene Graft Copolymer toward Photovoltaic Application. *ACS applied materials & interfaces* **2013,** *5* (23), 12672-12680.

37. Jiang, F.; Chen, D.; Li, R.; Wang, Y.; Zhang, G.; Li, S.; Zheng, J.; Huang, N.; Gu, Y.; Wang, C.; Shu, C., Eco-friendly synthesis of size-controllable amine-functionalized graphene quantum dots with antimycoplasma properties. *Nanoscale* **2013,** *5* (3), 1137-42.

38. Sun, H.; Gao, N.; Wu, L.; Ren, J.; Wei, W.; Qu, X., Highly Photoluminescent Amino-Functionalized Graphene Quantum Dots Used for Sensing Copper Ions. *Chemistry – A European Journal* **2013,** *19* (40), 13362-13368.

39. Luo, P.; Ji, Z.; Li, C.; Shi, G., Aryl-modified graphene quantum dots with enhanced photoluminescence and improved pH tolerance. *Nanoscale* **2013,** *5* (16), 7361-7.

40. Qi, Y.-X.; Zhang, M.; Fu, Q.-Q.; Liu, R.; Shi, G.-Y., Highly sensitive and selective fluorescent detection of cerebral lead(ii) based on graphene quantum dot conjugates. *Chem Commun* **2013,** *49* (90), 10599-10601.

41. Zhou, L.; Geng, J.; Liu, B., Graphene Quantum Dots from Polycyclic Aromatic Hydrocarbon for Bioimaging and Sensing of Fe3+ and Hydrogen Peroxide. *Particle & Particle Systems Characterization* **2013,** *30* (12), 1086-1092.

42. Qu, Z.-b.; Zhou, X.; Gu, L.; Lan, R.; Sun, D.; Yu, D.; Shi, G., Boronic acid functionalized graphene quantum dots as a fluorescent probe for selective and sensitive glucose determination in microdialysate. *Chem Commun* **2013,** *49* (84), 9830-9832.

43. Wang, Y.; Zhang, L.; Liang, R.-P.; Bai, J.-M.; Qiu, J.-D., Using Graphene Quantum Dots as Photoluminescent Probes for Protein Kinase Sensing. *Anal Chem* **2013,** *85* (19), 9148-9155.

44. Liu, J.-J.; Zhang, X.-L.; Cong, Z.-X.; Chen, Z.-T.; Yang, H.-H.; Chen, G.-N., Glutathione-functionalized graphene quantum dots as selective fluorescent probes for phosphate-containing metabolites. *Nanoscale* **2013,** *5* (5), 1810-1815.

45. Abdullah Al, N.; Lee, J.-E.; In, I.; Lee, H.; Lee, K. D.; Jeong, J. H.; Park, S. Y., Target Delivery and Cell Imaging Using Hyaluronic Acid-Functionalized Graphene Quantum Dots. *Molecular pharmaceutics* **2013,** *10* (10), 3736-3744.

46. Zhou, Y.; Qu, Z. B.; Zeng, Y.; Zhou, T.; Shi, G., A novel composite of graphene quantum dots and molecularly imprinted polymer for fluorescent detection of paranitrophenol. *Biosens Bioelectron* **2014,** *52*, 317-23.

47. Dong, Y.; Tian, W.; Ren, S.; Dai, R.; Chi, Y.; Chen, G., Graphene quantum dots/L-cysteine coreactant electrochemiluminescence system and its application in sensing lead(II) ions. *ACS applied materials & interfaces* **2014,** *6* (3), 1646-51.

48. He, Y.; Wang, X.; Sun, J.; Jiao, S.; Chen, H.; Gao, F.; Wang, L., Fluorescent blood glucose monitor by hemin-functionalized graphene quantum dots based sensing system. *Analytica chimica acta* **2014,** *810*, 71-8.

49. Deng, L.; Liu, L.; Zhu, C.; Li, D.; Dong, S., Hybrid gold nanocube@silica@graphene-quantum-dot superstructures: synthesis and

specific cell surface protein imaging applications. *Chemical communications* **2013,** *49* (25), 2503-5.

50. Ran, X.; Sun, H.; Pu, F.; Ren, J.; Qu, X., Ag nanoparticle-decorated graphene quantum dots for label-free, rapid and sensitive detection of Ag+ and biothiols. *Chemical communications* **2013,** *49* (11), 1079-81.

51. Bai, J. M.; Zhang, L.; Liang, R. P.; Qiu, J. D., Graphene quantum dots combined with europium ions as photoluminescent probes for phosphate sensing. *Chemistry* **2013,** *19* (12), 3822-6.

52. Hou, J.; Bei, F.; Wang, M.; Ai, S., Electrochemical determination of malachite green at graphene quantum dots–gold nanoparticles multilayers–modified glassy carbon electrode. *J Appl Electrochem* **2013,** *43* (7), 689-696.

53. He, G.; Song, Y.; Liu, K.; Walter, A.; Chen, S.; Chen, S., Oxygen Reduction Catalyzed by Platinum Nanoparticles Supported on Graphene Quantum Dots. *ACS Catalysis* **2013,** *3* (5), 831-838.

54. Wu, X.; Zhang, Y.; Han, T.; Wu, H.; Guo, S.; Zhang, J., Composite of graphene quantum dots and Fe3O4 nanoparticles: peroxidase activity and application in phenolic compound removal. *Rsc Adv* **2014,** *4* (7), 3299-3305.

55. Wang, X.; Chen, L.; Su, X.; Ai, S., Electrochemical immunosensor with graphene quantum dots and apoferritin-encapsulated Cu nanoparticles double-assisted signal amplification for detection of avian leukosis virus subgroup J. *Biosensors and Bioelectronics* **2013,** *47* (0), 171-177.

56. Yu, Y.; Ren, J.; Meng, M., Photocatalytic hydrogen evolution on graphene quantum dots anchored TiO2 nanotubes-array. *Int J Hydrogen Energ* **2013,** *38* (28), 12266-12272.

57. Dutta, M.; Sarkar, S.; Ghosh, T.; Basak, D., ZnO/Graphene Quantum Dot Solid-State Solar Cell. *The Journal of Physical Chemistry C* **2012,** *116* (38), 20127-20131.

58. Bin Yang, H.; Qian Dong, Y.; Wang, X.; Yun Khoo, S.; Liu, B.; Ming Li, C., Graphene quantum dots-incorporated cathode buffer for improvement of inverted polymer solar cells. *Sol Energ Mat Sol C* **2013,** *117* (0), 214-218.

Chapter 2

Sensing Aqueous Cations Using Photo Emission from GQDs

2.1 Introduction of Photo Quenching GQDs

Photoluminescent, PL, materials offer a good mechanism for analytical work due to the extreme sensitivity of the technique.[1] Due to the necessity of ligands to stabilize semiconductor quantum dots, the structures are insulated from the solvent and subsequently the analytes mitigating direct interaction.[2] With Graphene quantum dots, GQDs, they are innately soluble, have low toxicity,[3] and so do not require functionalization to stabilize them and are optically tunable.[4] With the electronic structure of GQDs directly interacting with the solvent as well as analytes there in, they can potentially act as powerful sensors.[5-7] There are simple synthesis requirements for GQDs compared to systems using quantum dots, QDs, which often require addition of ligands[8-9] to attain a sensitive system. The incredibly high surface area for GQDs readily allows for interactions with analytes, and the sorbtive surface has a π-system that is potentially fully conjugated across the whole nanoparticle.[10] This π-system may allow for an aggregate interaction with multiple ions quenching a single nanoparticle or using chelating interactions one ion may be able to quench multiple GQDs. It is understood that the π-system of the GQD could interact with the ions, in conjunction with, functional groups on the GQDs.[10] Functional groups situated on these nanoparticles are extremely varied, including aldehydes, esters, phenols, carboxylics, and others.[11-12] With hetero atoms added to the mix, the number of functional groups jump considerably. Many of these groups, singularly or in concert, could act as chelators with the ions in solution. These functional groups

provide a means for the ions to interact with the π-system which provide a possible rout for the exciton to transfer an electron to the ion.

The capacity to sense a variety of ions in aqueous solution might best be accomplished using an ion selective electrode. But deciphering between similarly charged ions can be difficult. A PL method could provide a means of detecting specific ions despite interference, using more than one photo channel. Also a PL method properly constructed might be able to distinguish more exotic ions.

Previous papers have noted that graphene quantum dots (GQDs) can be used as ion sensors via their quenching of their photoluminescence.[13] However a detailed understanding of what it takes to produce quenching and through what mechanism this quenching occurs is still not clear. We aim with this research to better understand the mechanism behind which these aqueous ions quench the PL of the GQDs.

2.2 Experimental

2.2.1 Method Used to synthesize GQDs and nGQDs

Synthesis of GQDs: In order to maintain consistency a few batches of GQDs were synthesized and combined to make a stock solution of GQDs that was used specifically for this project. Graphene fiber, 1 g per 100 ml of solvent, oxidizing solvent was composed of 40 ml of Con Nitric Acid, 60 ml Con Sulfuric Acid. The fiber was sonicated for two hours then heated with a reflux column with stirring 16±1 h at 110 °C. The solution was then neutralized using sodium hydroxide, as well as sodium hydroxide with sodium carbonate. Sodium sulfide was then allowed to

crystalize out of solution and the supernatant was poured off and dialysized for three days to purify. No flocculates were observed nor could be extracted by centrifugation. The sample was then dried by rotary evaporator as well as vacuum desiccator, after which the GQDs looked like fine black sand and could be weighed easily. A stock vial of 20 mg to which 20 ml of DI water was added, this stock solution was used for all ion sensitivity tests. In tests where a known mass was not necessary, the dry nanoparticles were used.

Nitrogen doped GQDs were made using a method developed originally by Qu *et al.*[14] modified slightly here as follows: 180 mg urea, 210 mg citric acid, dissolved in 2.5 ml DI water, along with 2.5 ml Propylene glycol in a 20 ml Teflon bomb heated to 160 ° C for four hours.

2.2.2 Materials Used to synthesize GQDs and nGQDs

Water Supplied by Barnstead Nanopure water system
GQD Fiber, Fibre Glast
Propylene Glycol 99.5 % Fisher
$NaHCO_3$ 99.7 % Fisher
Na_2CO_3 99.9 % Fisher
NaOH 98 % Fisher
HNO_3 Fisher
H_2SO_4 Fisher
Urea 99.4 % Fisher

Ions:
$Zn(II)(NO_3)_2$ Acros 98 %
$Ba(II)(NO_3)_2$ Acros chemicals no purity
$Cu(II)SO_4$ in house no maker
$Fe(II)SO_4$ Fisher 98+% pure
Ruthenium Chloride ($RuCl_3$, 35–40% Ru, ACROS)
$La(NO_3)_3 * 6\ H_2O$ alfa inorganics
$SrCl_2 * 6$ H2O Matheson Coleman Bell 98 % (couldn't refind)
$ZnSO_4 * 7\ H_2O$ CP Bakers Eberbach Ann Arbor MI 99 %
$Cu(II)(NO_3)_2\ 2.5\ H_2O$ Fisher 98.6 %

$NiSO_4$ * 6 H_2O 98 % +Fisher used for nGQDs
$NiCl_2$ * 6 H_2O 98 %+ Matheson Coleman Bell
$Ni(II)OAc_2$ * 4 H_2O 98 % + Matheson Coleman Bell
$CoCl_2$ * 6 H_2O 98.1 % Fisher Scientific or Chemical lot # 897930
$Co(II)(NO_3)_2$ * 6 H_2O 98 %+ Matheson Coleman Bell
$Co(II)(OAc)_2$ * 4 H_2O 98 % + Matheson Coleman Bell
$Fe(III)(NO_3)_3$ * 9 H_2O Fisher Scientific or Chemical lot #712221
$Mn(OAc)_2$ * 4 H_20 98 % + Matheson Coleman Bell
$Cr(III)(NO_3)_3$ * 9 H_2O 98 % + Matheson Coleman Bell
$Mg(II)(NO_3)_2$ * 6 H2O 98 % + Matheson Coleman Bell
$Mg(II)(OAc)_2$ * 4 H2O 98 % + Matheson Coleman Bell
$MgSO_4$ * 7 H2O 99 % + J T Baker Chemical Co
$Cs(NO_3)_3$ Alfa Aesar 99.8 % lot # A23R036 stock # 12884
$Pb(OAc)_2$ 99.8 % Alpha Aesar lot # E05N19
$CdCl_2$ Matheson Coleman Bell 99 % +
$Ce(III)(NO_3)_3$ * 6 H2O 98 % + Matheson Coleman Bell
$LiNO_3$ 99 % + Fisher Scientific Company
$Li(OAc)_1$ * 2 H2O 98 % Acros organics + lot#199842500
$Al(III)$ $(OAc)_1(OH)_2$ * 1/3 H3 Matheson Coleman Bell 140.657 mw
HgCl2 mw 271.60 Matheson Coleman Bell 99 %
$BaCl_2$ * 2 H2O 99.4 % Fisher Scientific lot#706151
$Ba(OAc)_2$ mw 255.43 98 % Acros organics lot#222805000
$AgNO_3$ 99 % + Fisher Scientific

2.2.3 Experimental Quenching Procedure

A solution of 1 mg/ml was used as the source solution for GQDs, with 100 µl auto pipetted (accurate to ±2%) into 3 ml of DI water. PL measurements are taken prior to the addition of salt each and every time. Initial intensity is taken to be unity and used to standardize all further spectra. Additions of salt are carried out, using a Hamilton microliter syringe and stirred with the said syringe tip. Once 10 µl was reached, an auto-pipette was used. Additions of salt solution were done in successively larger increments; 0.5, 0.5, 1.0, 1.0, 2.0, 2.0, 3.0, 5.0, 5.0, 10.0, 20.0 µl, totaling 50 µl (for most experiments), which allowed a larger range to be probed

without reducing resolution at low concentrations. Solvent dilution is factored into concentration values but not for PL values.

Obtaining changes in percent intensity vs. concentration (cipic) values in order to compare quenching efficiency between different analytes was done as follows: PL excitation values were 464 nm for GQDs sourced from carbon fiber and nGQDs were excited at 384 nm. For PL emission intensities three averaged values were used, 529, 530, and 531 nm for carbon fiber GQDs, and 454, 455, and 456 nm were used for nGQDs. For a single experiment the initial intensity value was taken to be unity and subsequent values were scaled as percent's thereof.

2.3 Results & Discussion of Photo Quenching Experiments with GQDs and nGQDs

Quenching of PL emission from graphene quantum dots for our samples were consistent and very repeatable. Figure 2.1 shows Spectra acquired with additions of $CuCSO_4$ from a 0.01 M solution to the 4 ml cuvette. Included is a plot of peak intensity values, post cipic normalizations, for two runs plotted concurrently, with the y-axis as percent of initial intensity (PII). They show consistent quenching behavior and a repeatable experimental procedure. The slope for the first experiment PL decline value is calculated as -1.34×10^4 M^{-1} cipic. The second run, conducted on a different day, the slope is calculated as -1.10×10^4 M^{-1} cipic. Although notably different, the two runs show consistent repeatable behavior, however slope values in cipic values should not be evaluated to more than two significant figures.

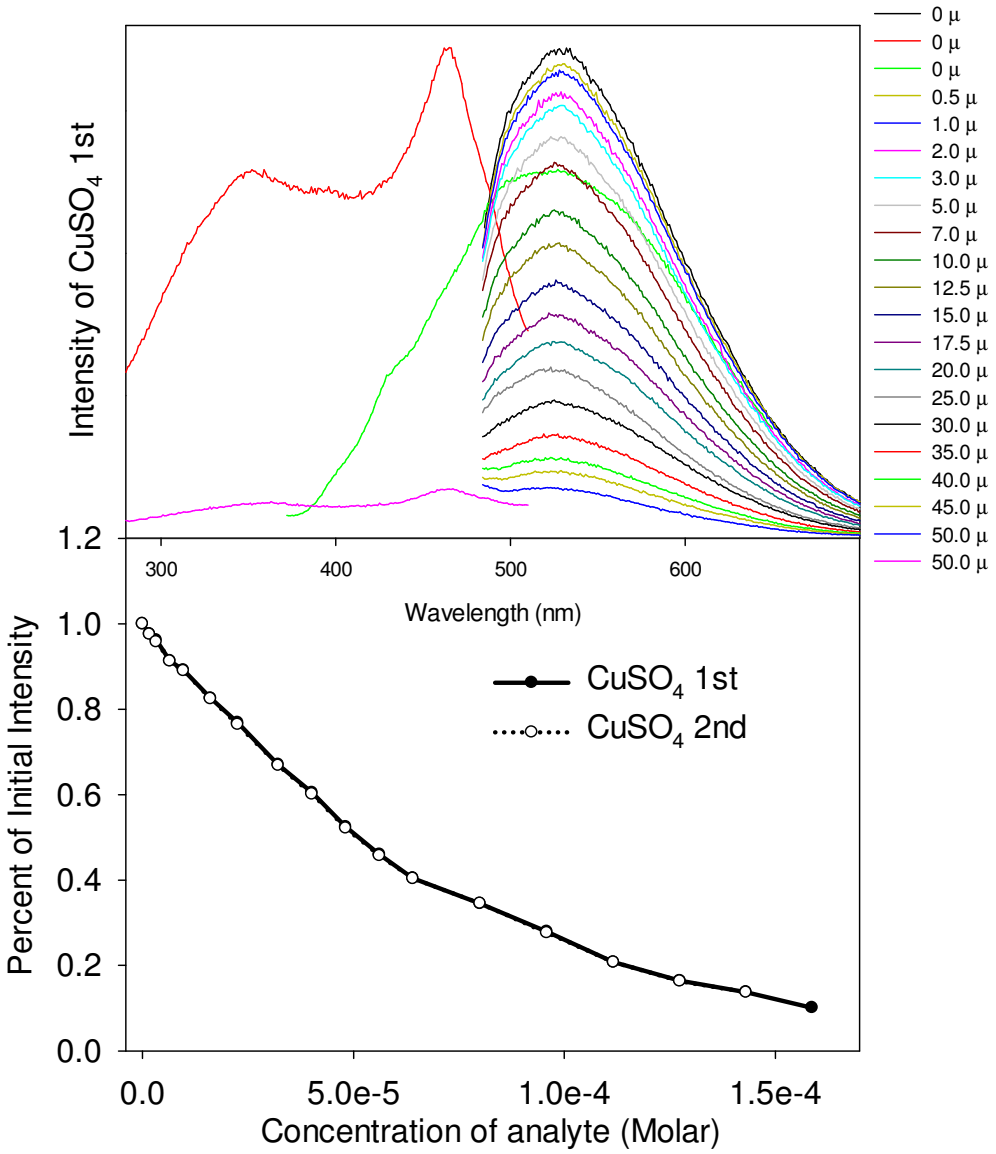

Figure 2.1: Top panel: the excitation and emission profile of graphene quantum dots with subsequent emissions after addition of $CuSO_4$ salt analyte. Excitation is at 464 nm and emission at 530 nm, with a weaker excitation at 350 nm. Bottom panel: the same experiment shown in the top panel along with a second run to show repeatability. Analyte additions are as follows (two initial spectra 0.0), 0.5, 0.5, 1.0, 1.0, 2.0, 2.0, 3.0, 2.5, 2.5, 2.5, 2.5, 5, 5, 5, 5, and 5 µl giving a final 45 µl volume for the 2^{nd} run with an added 5 µl totaling 19 emission spectra for the first. Concentrations varied from an initial $1.6x10^{-6}$ M (0.5 µl) $CuSO^4$ to a final concentration of $1.6x10^{-4}$ M most runs concluded at 50 µl like that of the first run shown. A final excitation scan is shown, illustrating that there is no shift in the excitation position as well as that the second excitation band quenches with the primary.

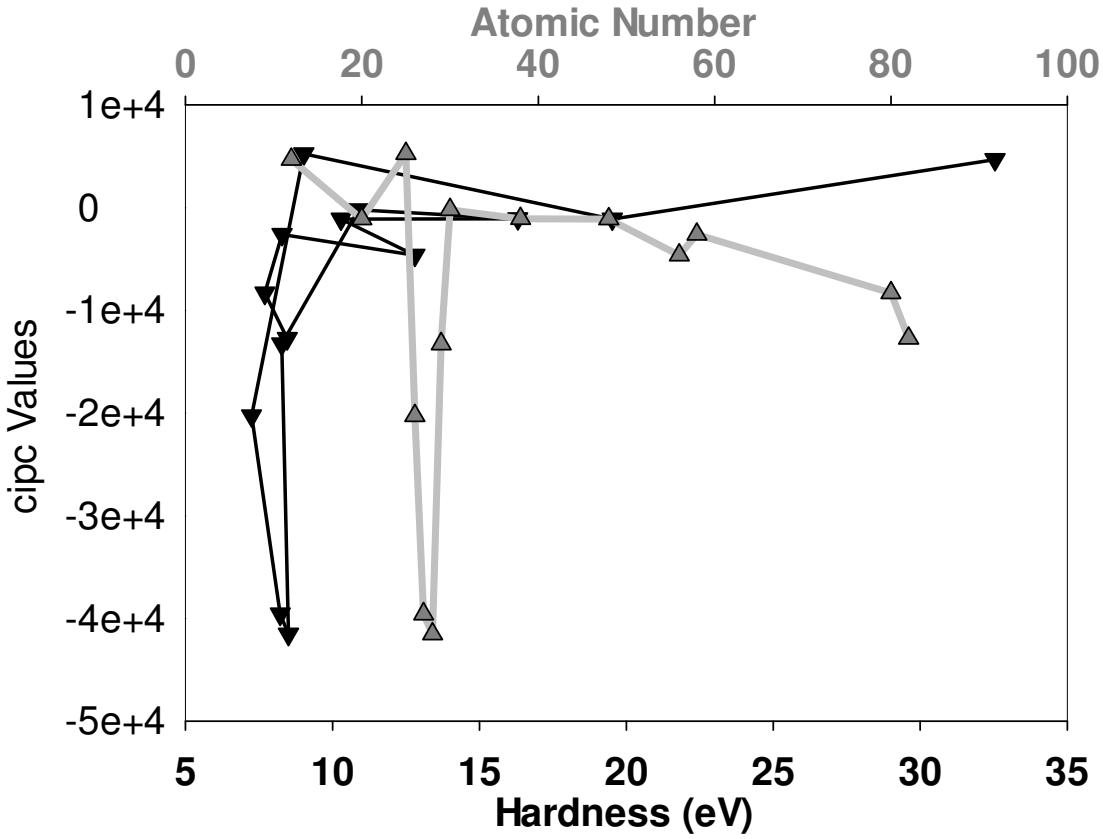

Figure 2.2: A double trace of GQDs, with the plotting of y-axis as quenching value (cipic) for dications. The gray trace with up facing arrows corresponds with the atomic number and is plotted using the top x-axis which can be used to identify individual data points, in order they are: Mg^{2+}, Ca^{2+}, Mn^{2+}, Fe^{2+}, Co^{2+}, Ni^{2+}, Cu^{2+}, Zn^{2+}, Sr^{2+}, Cd^{2+}, Ba^{2+}, Ce^{2+}, Hg^{2+}, and Pb^{2+}. Quenching is noted to have a periodicity that when replotted with the abscissa being chemical hardness strongly quenching salts line up.

Compiled cipic values are plotted for number of different quenching salts, dications cations only are shown in Figure 2.2. A trace drawn through the values from lowest atomic number to highest in order to illustrate the trend in quenching that points to a hardness of 8.50 eV, similar to the most efficient quencher; hardness values were taken from Pearson as well as Parr and Pearson.[15-16] This explanation accounts for why plumbous ions, 8.46 eV, would also act as quenchers with a value

nearly identical for nickel, which was the strongest quencher of the ions tested. We point to the empty orbital which has to have the proper characteristics to accept electrons to act as a quencher. Accepting an electron requires an orbital that extends out beyond the filled valence shell as well as the proper size to interact efficiently with the active site on the nanoparticle. Nickel and cobalt both have empty d orbitals acting as their empty valence shells. Cerium is a good example of a quencher that has a chemical hardness of 8.28 eV, which is close to the optimum quenching value, yet has a poor quenching cipic value, -2.6×10^{3} M^{-1} compared to -4.2×10^{4} M^{-1} for nickel. We ascribe its low quenching value to having an empty s orbital buried deep below the valance cloud of the filled orbitals. With only an empty acceptor orbital contained within a filled valence band it appears to be unavailable to act as a quencher due to shielding electrons. One ion, manganese, did not quench and showed a steady improvement upon the PL emission intensity of the GQDs. The improvement in PL emission was not observed for nGQDs. Perhaps manganese stabilized emission edge defects.

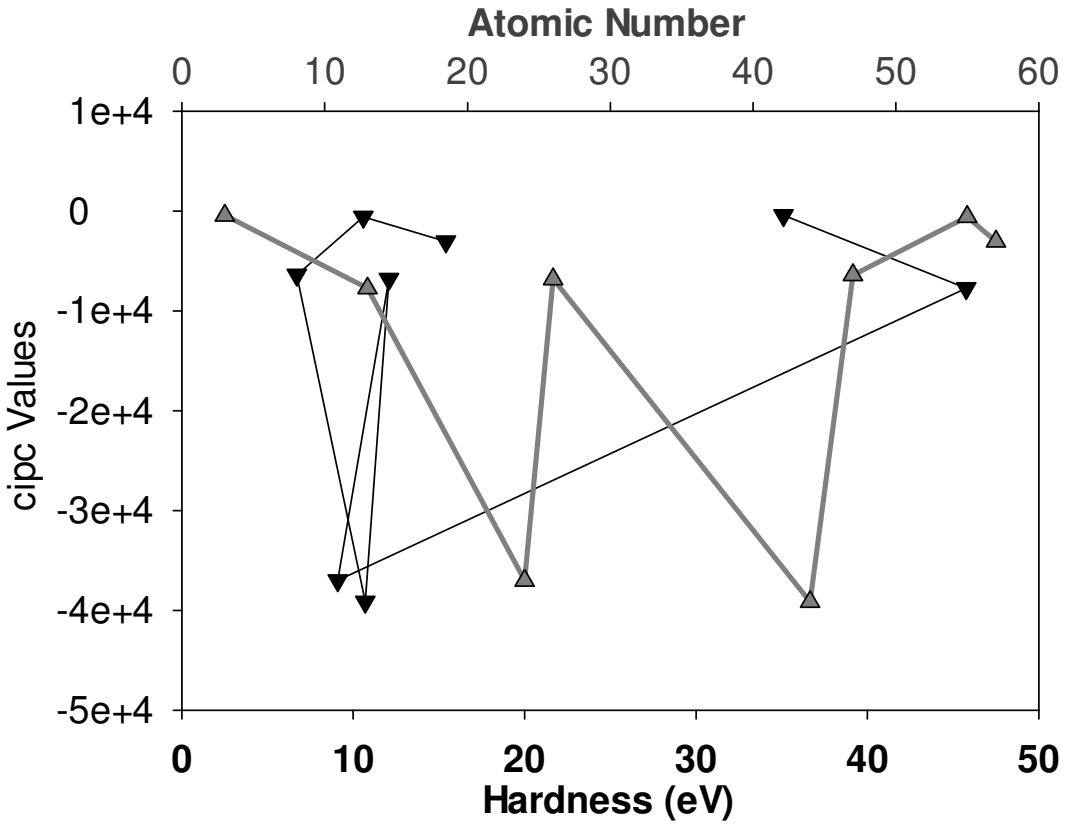

Figure 2.3: A double trace of GQDs values for mono and triply charged cations and is plotted upward facing triangles using the top axis and the downward facing triangles plotted with the bottom axis, in order they are: Li^{1+}, Al^{3+}, Cr^{3+}, Fe^{3+}, Ru^{3+}, Ag^{1+}, Cs^{1+}, and La^{3+}. The data shows similar periodicity, to the di-cations, but centered on a different optimum quenching hardness, 10.6 eV for ruthenium, and chromium at 9.1 eV which showed similar quenching.

The maximum quenching rate seems to reach a critical value for our experiments of approximately -3.9×10^4 M^{-1} cipic, found by averaging the four strongest quenchers we tested, chromium, nickel, cobalt, and ruthenium. Tables of these values can be found in Table 2.1. Of note is that we found no mono charged cations observed to quench, as plotted in Figure 2.3, and no singly charged cations were noted to have empty orbitals of p or d character of those tested. The quenching trend is still observable with the removal of the singularly charged cations looking at

the triply charged cations alone. Also of note is the lack of strong quenching by iron which is contrary to observations by Huang *et al.*[13]

We also looked at PL recovery using ethylenediaminetetraacetic acid (EDTA) and achieved similar results to those of Huang *et al.*,[13] confirming many of their results. We aimed to also go further in discerning what mechanism controls quenching and how it might be better utilized selectively sense ions. Huang *et al.* noted that the quenching effect was not recovered when a Fe^{3+} salt was used as the quencher, however we did observe recovery for our nanoparticles, Figure 2.4. They state that the likely cause is the small Ksp $4x10^{-38}$ for $Fe(OH)_3$, likewise with $6.3x10^{-31}$ for $Cr(OH)_3$ which we did not see recover from additions of EDTA with a bound to unbound ratio of 23.4, binding ratios obtained from Martel and Smith[17]. It should be noted that we did not test $Ru(OH)_3$ with a ksp $1x10^{-36}$. The explanation of Ksp or EDTA binding doesn't seem sufficient to describe why some nanoparticles show recovery and some do not. One more complex example is $Al(OH)^3$ with a ksp $3x10^{-34}$, which has a markedly different result compared to expectations if a small ksp results in a marked lack of response to addition of EDTA especially as EDTA is not as strongly binding of Al^{3+} 16.5 bound to unbound ratio vs. Fe^{3+} 25.1. Clearly solubility constants are insufficient to explain the quenching and recovery results.

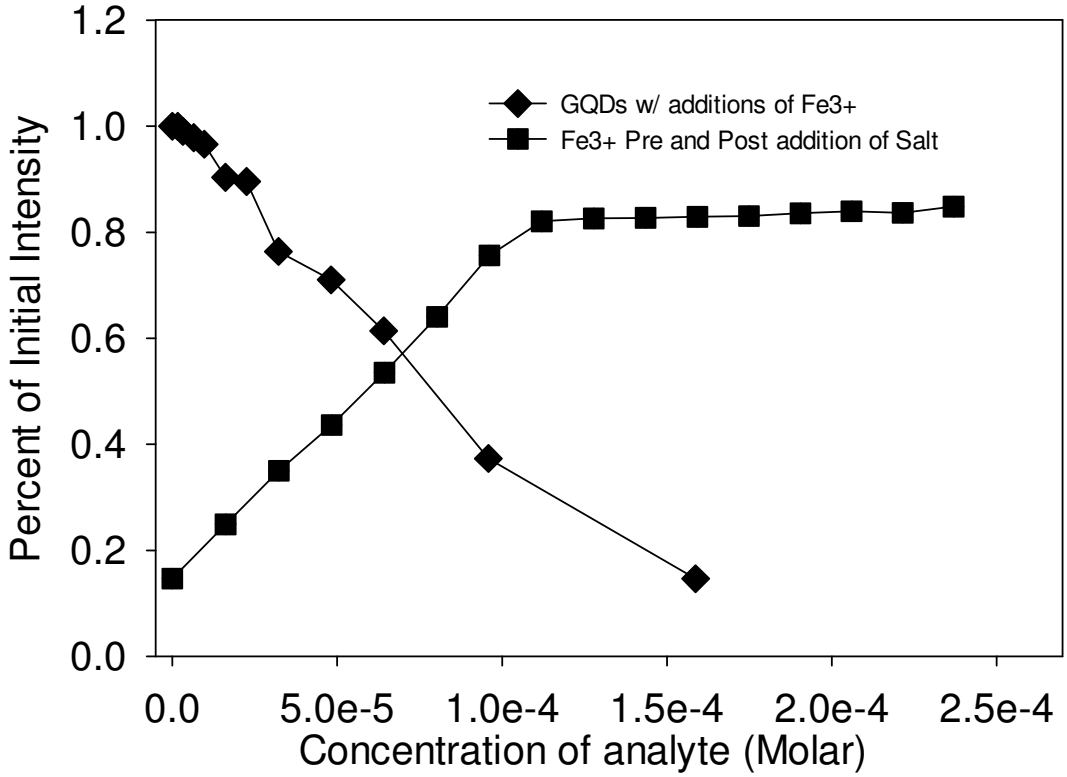

Figure 2.4: Black diamonds show quenching starting with the standard GQD concentration starting at 1 PII, quenched with additions of Fe^{3+} ions. Recovery of PL, shown as black squares, from a concentration of $1.6x10^{-4}$ M in Fe^{3+}, with 5 µl additions of 0.01 M EDTA. The quenching recovery is not complete, and remains at just over 80 % of the original intensity. Both plots use concentration plotted on the x-axis.

A unique response was observed for aluminum. Initial additions of the salt to the GQDs acted as a PL enhancer after a critical point (7 µl $2.25x10^{-5}$ M). At which point the response turned negative and the ions began to act as a PL quencher. With additions of EDTA the EDTA acted to further quench the sample, then after a critical point (15 µl, $4.74x10^{-5}$) the PL recovery began. The concentration of added EDTA was just over double the value of 7 µl, at 15 µl, which could point to a titration effect with the EDTA binding in concert with the aluminum ions in a ratio of 1 Al, 2 EDTA,

1 GQD quenching, but it isn't certain. Four other samples showed similar concentration dependent behavior, which were zinc ions, strontium, cadmium, as well as barium. Zinc and strontium both showed initial increases in PL followed by quenching. With peak intensity, 104 and 107 percent of initial intensity, PII, reached at $3.2x10^{-5}$ M for $Zn(NO_{3,})_2$ and $ZnSO_4$ respectively with subsequent additions quenching. Cadmium showed initial increases to 106 PII at $1.6x10^{-5}$ M for $CdCl_2$ followed by a steady decrease. For both zinc and cadmium additions of EDTA decreased PL steadily rather than recover it. Strontium showed behavior similar to that of aluminum. Showing an increase to 104 PII at 1.6 $x10^{-5}$ M followed by a steady decline, additions of EDTA did show behavior opposite that of aluminum, additions of EDTA showed an initial recovery followed by a steady decline. Interaction between these GQDs and ions points to complex behavior likely with multiple binding sites on the GQDs with differing affinities.

Relatively few ions are noted to form complexes with more than one EDTA molecule, we used Martell *et al.*[17] for our listing of complexing values, only one ion of those tested complexes with more than one EDTA molecule, ferric ions. With a complexation constant smaller for the multi ligand structure, we don't consider it to be of strong significance.

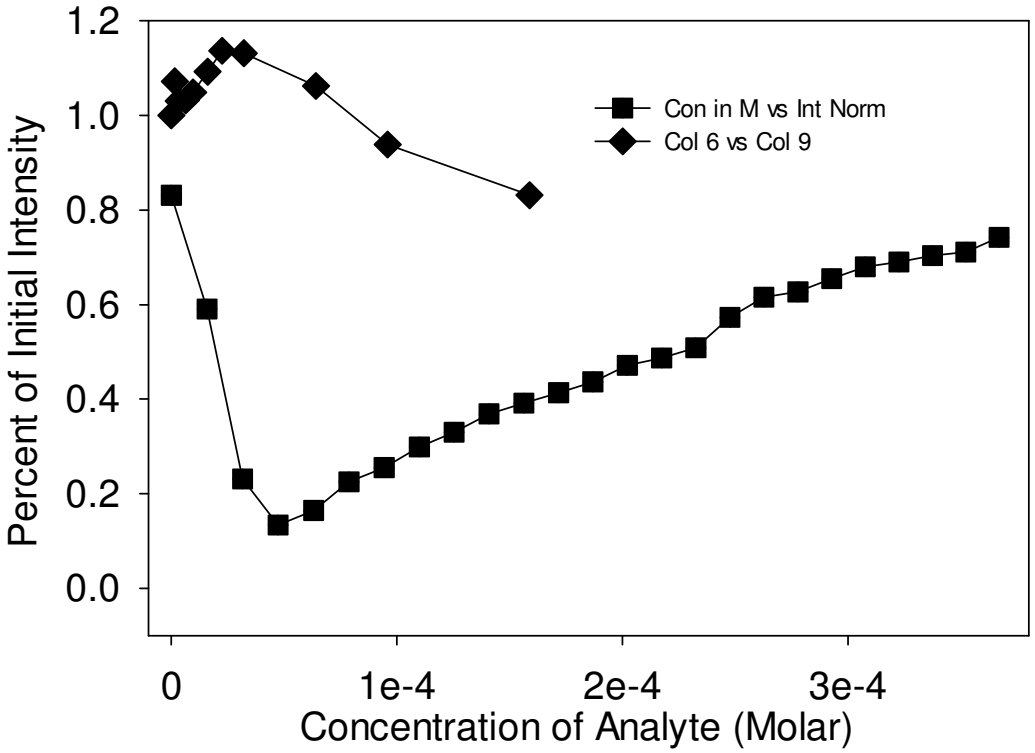

Figure 2.5: Black diamonds show quenching starting with the standard GQD concentration starting at 1 PII, quenching with additions of Al^{3+} ions. With an initial increase and subsequent decrease in PL, using only additions of Al^{3+} the concentration dependent behavior is observable. Black squares show changes in PL due to additions of EDTA. Both plots use concentration plotted on the x-axis.

A number of possible explanations present themselves for the increase in PL followed by decreases for aluminum's response in Figure 2.5. As the samples are made from pitch fiber a great verity of nanoparticles could be formed yielding a bimodal population that has a concentration of 1.6 $x10^{-5}$ M approximately. Further evidence could be shown by zinc ions with two interacting with one site as the maximal intensity was reached at twice the concentration, $3.2x10^{-5}$ M. Aluminum has the most profound quenching and recovery and is the only one noted to decrease

upon addition of EDTA with a subsequent increase in PL. Further evidence for two sets of active sites were the two excitation values for the GQDs, Figure 2.1.

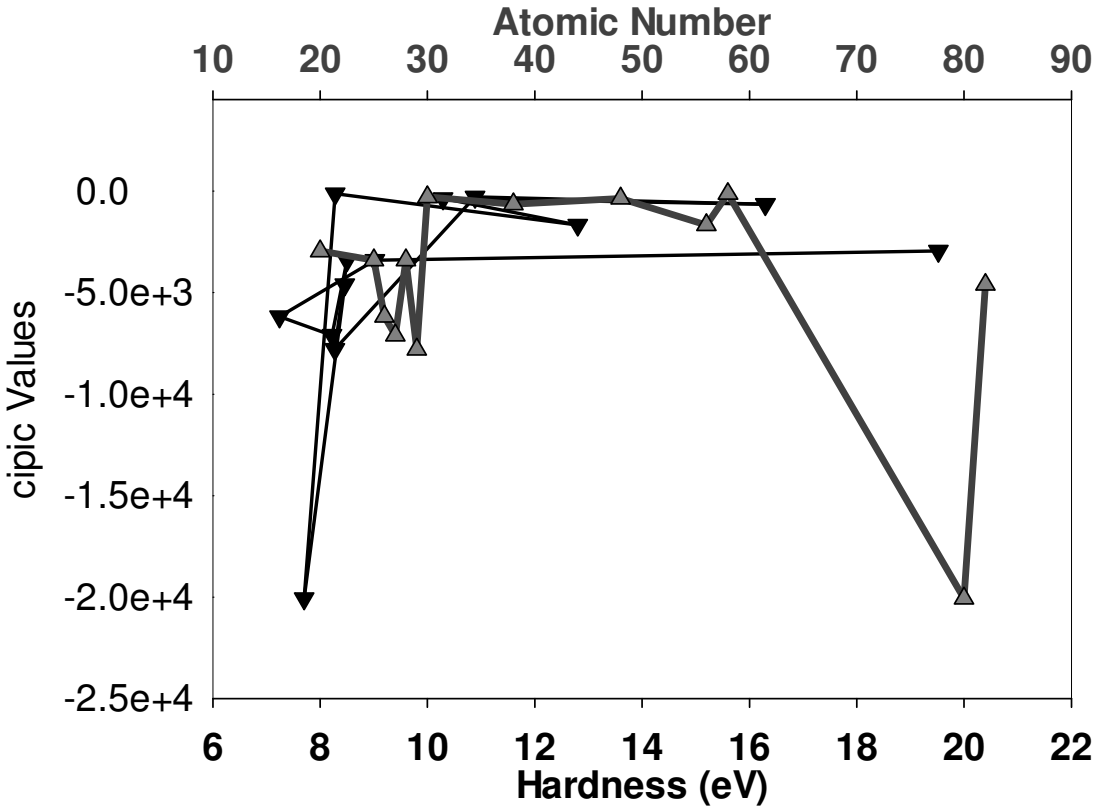

Figure 2.6: A double trace of nCNP cipic values, acting as the y-axis for dications. The gray trace with up facing arrows corresponds with the atomic number and is plotted using the top axis which can be used to identify data points, in order they are: Ca^{2+}, Mn^{2+}, Fe^{2+}, Co^{2+}, Ni^{2+}, Cu^{2+}, Zn^{2+}, Sr^{2+}, Cd^{2+}, Ba^{2+}, Ce^{2+}, Hg^{2+}, and Pb^{2+}.. When replotted using chemical hardness the optimum quenching salts line up, however a different hardness is observed to be optimal. Mercuric ions at 7.7 eV show the strongest quenching.

With a markedly different emission and excitation the nCNP sample were exited showed a strong response to mercuric ions, possibly optimized for a larger size. Also of note were the poor response to nickelous ions which was consistent for sulfate, acetate and chloride forms, but it can be explained when its hardness of 8.5

eV is compared. Ferrous ions with a lower hardness value of 7.2 eV which is short of that of 7.7 eV for mercuric ions, cobaltous and cupric ions 8.2 eV and 8.3 eV respectively, are a bit higher but the nickelous ions are considerably harder.

For Figure 2.6 mercuric ions show the optimum quenching value at 7.7 eV for mercuric ions with a cipic value of -2.0×10^3 M^{-1}, with PL spectra shown in Figure 2.7. The nCNP are possibly optimized for larger ions, but inconclusively. Also of note is the poor response to nickelous ions which was consistent for sulfate, acetate and chloride forms but it can be explained when its hardness of 8.5 eV is compared. Ferrous ions (cipic values of -6.2×10^3 M^{-1}) with a lower hardness value of 7.2 eV which is short of that of 7.7 eV cobaltous (8.2 eV, cipic value of -7.1×10^3 M^{-1}) and cupric (8.3 eV, cipic value of -6.2×10^3 M^{-1}) ions, are a bit harder but the nickelous ions are even harder still, making them poorer quenchers. Plumbous ions are larger and are possible evidence that the nCNPs are more sensitive to larger ions, with a cipic value of -4.6×10^3 M^{-1} and a chemical hardness of 8.5 eV. The lead ions still quenches better than the previously mentioned nickelous ions. Although not optimum in chemical hardness, lead may have a more optimum size and let it quench moderately.

Excitation and emission values also point to why some ions may quench better than others. The weaker excitation band for the GQDs at 350 nm is 3.54 eV; a value which is greater than the 384 nm, 3.24 eV, excitation for the nGQDs which have a lower chemical hardness for optimum quenching. Although the values don't match

exactly the difference in quenching hardness, 8.50 eV (GQDs) vs. 7.70 eV (nGQDs) is approximately 10 percent less similar to the difference in excitation values.

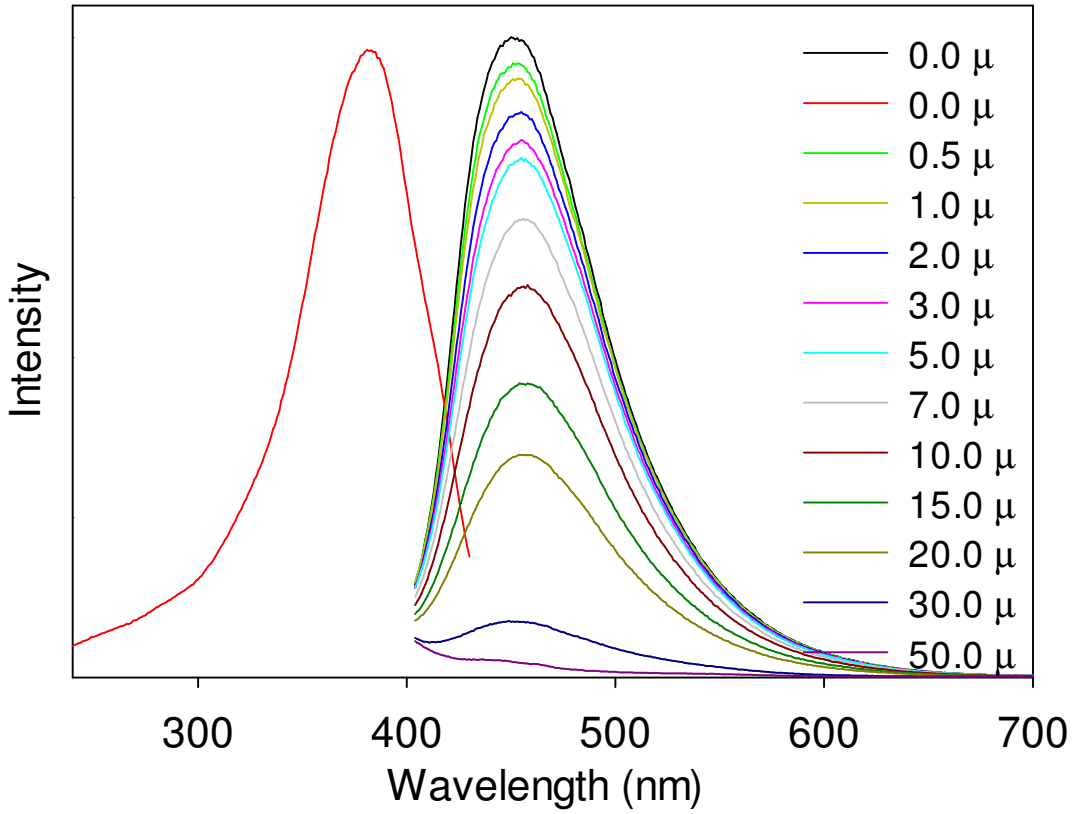

Figure 2.7: Photoluminescence quenching of nGQDs by Mercury chloride with additions labeled in µl. Excitation for nGQDs is at 384 nm and emission is at 455 nm. No shift in peak position is noted or new peaks emerging like that of GQDs sourced from carbon fiber.

Looking at EDTA recovery in regard to all of the experiments yielded a similar trend to that of the quenching, Figure 2.2. In order to recover from quenching, it does require that the salt caused quenching to recover from. However the strong recovery of ferrous ions was slightly anomalous and could be due to the significantly greater binding constant for EDTA to iron at a value of 25.1, as compared to copper at 18.8. The other strong quenchers, cobalt at 16.3 and nickel at

18.6, have similar bound to unbound ratios. The anomalous behavior of aluminum ions stands out even more when plotted as cipic values, Figure 2.9. The explanation that complexation of the aluminum ion by EDTA modifying its hardness and moderating its interaction with the GQDs is further supported due to its extreme hardness, 45.77 eV, making it the hardest of any of the tested ions. Only manganese comes close with a hardness of 32.55 eV which showed no quenching and no response to EDTA additions. The optimum recovery occurring with cupric ions over that of cobaltous and nickelous ions can be ascribed to greater EDTA binding with copper ions showing a bound to unbound ratios of 18.6 vs. 16.3 and 16.5 for cobalt and nickel respectively.

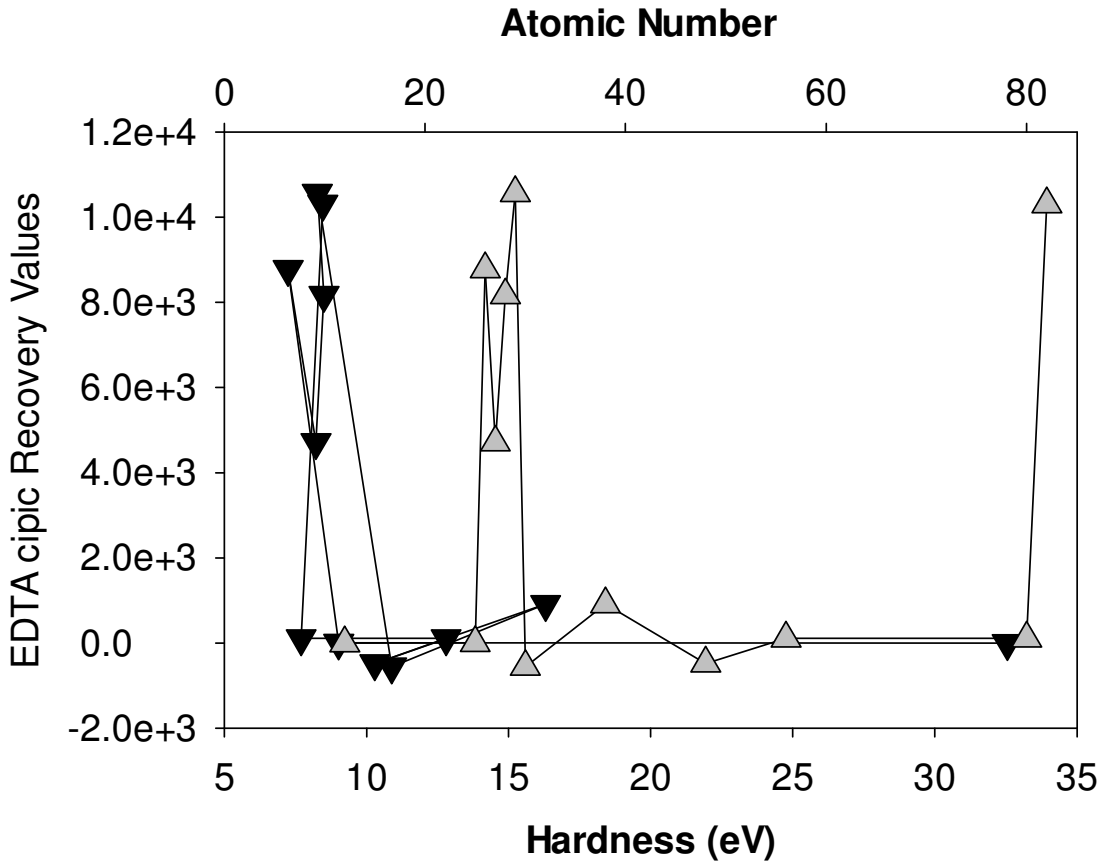

Figure 2.8: A double trace plotting dications, with the plotting of y-axis as a recovery value, cipic. The gray trace with up facing arrows corresponds with the atomic number and is plotted using the top axis which can be used to identify individual data points, in order they are: Mg^{2+}, Mn^{2+}, Fe^{2+}, Co^{2+}, Ni^{2+}, Cu^{2+}, Zn^{2+}, Sr^{2+}, Cd^{2+}, Ba^{2+}, Hg^{2+}, and Pb^{2+}. Recovery of PL is strongest for cupric ions not nickelous ions or cobaltous ions.

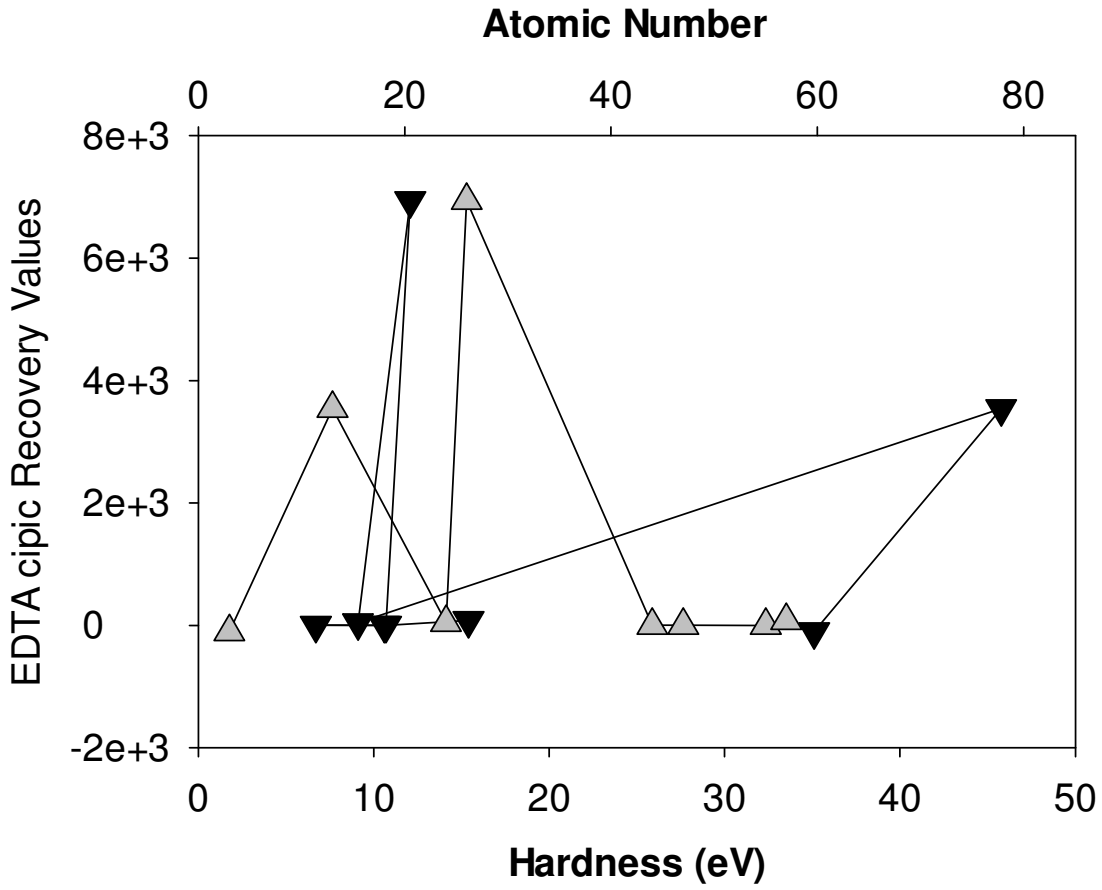

Figure 2.9: A double trace with the plotting of y-axis as recovery value, cipic. The gray trace with up facing arrows corresponds with the atomic number and is plotted using the top axis which can be used to identify individual data points, in order they are: Li^{1+}, Al^{3+}, Cr^{3+}, Fe^{3+}, Ru^{3+}, Ag^{1+}, Cs^{1+}, and La^{3+}. Fe^{3+} ions show strong recovery as well as Al^{3+} ions when sufficient additions of EDTA.

Table 2.1: Compiled cipic Quenching Values For all Sensing Experiments

Ion	Charge	GQD cipic Value	nGQD cipic Value	EDTA Recovery slope	Atomic Number	Hardness in eV	Binding Ratio EDTA
Mg	2+	4.7E+03	-	-3.8	**12**	**32.55**	8.8
Ca	2+	-1.1E+03	-3.0E+03	-	**20**	**19.52**	10.7
Mn	2+	5.3E+03	-1.1E+03	7.4	**25**	**9.02**	13.8
Fe	2+	-2.0E+04	-6.2E+03	8781.8	**26**	**7.24**	25.1
Co	2+	-4.0E+04	-7.1E+03	4712.6	**27**	**8.22**	16.3
Ni	2+	-4.2E+04	-3.4E+03	8169.5	**28**	**8.50**	18.6
Cu	2+	-1.3E+04	-7.8E+03	10568.4	**29**	**8.27**	18.8
Zn	2+	-1.9E+02	-6.6E+02	-552.7	**30**	**10.88**	16.5
Sr	2+	-1.1E+03	-6.5E+02	912.4	**38**	**16.30**	8.7
Cd	2+	-1.1E+03	-3.7E+02	-479.1	**48**	**10.29**	16.5
Ba	2+	-4.6E+03	-1.7E+03	111.7	**56**	**12.80**	7.9
Ce	2+	-2.6E+03	-1.3E+02	-	**58**	**8.28**	15.5
Hg	2+	-8.3E+03	-2.0E+04	109.6	**80**	**7.70**	21.7
Pb	2+	-1.3E+04	-4.6E+03	10309.4	**82**	**8.46**	18.0
Li	1+	-4.4E+02	-4.2E+03	-103.4	**3**	**35.12**	2.8
Al	3+	-7.7E+03	-1.3E+04	3542.3	**13**	**45.77**	16.5
Cr	3+	-3.7E+04	-5.0E+03	43.5	**24**	**9.10**	23.4
Fe	3+	-6.8E+03	-4.6E+03	6938.8	**26**	**12.08**	7.3
Ru	3+	-3.9E+04	-1.1E+04	0.0	**44**	**10.70**	NA
Ag	1+	-6.4E+03	-4.6E+03	0.2	**47**	**6.70**	0.2
Cs	1+	-5.8E+02	-9.2E+03	-0.1	**55**	**10.60**	15.5
La	3+	-3.0E+03	-3.1E+02	77.8	**57**	**15.40**	NA

Calculations can be done to assess the number of active quenching sites using a theoretical end point for titration of 50 µl with 0.01 M salt (0.5 µmole), speculating based on quenching with cupric ions. Starting with 100 µl at 1 mg/ml (0.1 g) assuming one salt ion per quenching site yields a concentration of yields a molecular weight per quenching site of 200,000 Daltons, which if a protein, would be approximately 5 nm in radius, not an unreasonable value.

2.4 Conclusions

We have produced graphene quantum dots from carbon fiber which displayed photoluminescent properties in aqueous media. Additions of soluble salts were shown to have distinguishable quenching of emission in an unoptimized system with concentrations as low as $1.6x10^{-6}$ M for the strongest quenchers. Strongly quenching ions were observed to show an optimum chemical hardness, for GQDs at 8.50 eV corresponding to nickel dications. Quenching was shown to falls off as chemical hardness deviates from the optimum value. A second set of nanoparticles doped with nitrogen was produced with photoluminescent properties and were observed to quench with similar sensitivity as low as $1.6x10^{-6}$ M for the strongest quenchers. Comparison between the two sets of nanoparticles showed similar quenching, but with markedly different optimal hardness values. Mercury dications with a chemical hardness of 7.70 eV showed the strongest quenching for nGQDs. A possible bias toward larger ions was also observed for the nGQDs. Recovery of a significant portion of the photoluminescent intensity was also noted with the addition of EDTA to the solution, with similar trends in reverse, however, with optimum recovery clustered near that of optimum quenching. Complexation values for ions with EDTA likely play a role in slightly altering the optimum recovery hardness.

2.5. References

1. Mirzov, O.; Scheblykin, I. G., Photoluminescence spectra of a conjugated polymer: from films and solutions to single molecules. *Phys Chem Chem Phys* **2006,** *8* (47), 5569-5576.

2. Frigerio, C.; Ribeiro, D. S. M.; Rodrigues, S. S. M.; Abreu, V. L. R. G.; Barbosa, J. A. C.; Prior, J. A. V.; Marques, K. L.; Santos, J. L. M., Application of quantum dots as analytical tools in automated chemical analysis: A review. *Analytica chimica acta* **2012,** *735* (0), 9-22.

3. Yang, S.-T.; Cao, L.; Luo, P. G.; Lu, F.; Wang, X.; Wang, H.; Meziani, M. J.; Liu, Y.; Qi, G.; Sun, Y.-P., Carbon Dots for Optical Imaging in Vivo. *J Am Chem Soc* **2009,** *131* (32), 11308-11309.

4. Tetsuka, H.; Asahi, R.; Nagoya, A.; Okamoto, K.; Tajima, I.; Ohta, R.; Okamoto, A., Optically Tunable Amino-Functionalized Graphene Quantum Dots. *Adv Mater* **2012,** *24* (39), 5333-5338.

5. Sun, H.; Wu, L.; Wei, W.; Qu, X., Recent advances in graphene quantum dots for sensing. *Materials Today* **2013,** *16* (11), 433-442.

6. Evoy, S.; DiLello, N.; Deshpande, V.; Narayanan, A.; Liu, H.; Riegelman, M.; Martin, B. R.; Hailer, B.; Bradley, J. C.; Weiss, W.; Mayer, T. S.; Gogotsi, Y.; Bau, H. H.; Mallouk, T. E.; Raman, S., Dielectrophoretic assembly and integration of nanowire devices with functional CMOS operating circuitry. *Microelectron Eng* **2004,** *75* (1), 31-42.

7. Balapanuru, J.; Yang, J. X.; Xiao, S.; Bao, Q.; Jahan, M.; Polavarapu, L.; Wei, J.; Xu, Q. H.; Loh, K. P., A graphene oxide-organic dye ionic complex with DNA-sensing and optical-limiting properties. *Angewandte Chemie* **2010,** *49* (37), 6549-53.

8. Kakkar, P. M. J. S. R., A review on CdSe quantum dots in sensing. *Adv. Mat. Lett.* **2014,** *5* (11), 612-628.

9. Abdul Ghani, S. F.; Wright, M.; Paramo, J. G.; Bottrill, M.; Green, M.; Long, N.; Thanou, M., Three bisphosphonate ligands improve the water solubility of quantum dots. *Faraday discussions* **2014**.

10. Xiaohua, F.; D., P. B.; Lingjie, L.; Chen, S., Chemical Functionalization of Graphene Quantum Dots. *Sci. Adv. Mater.* **2015**.

11. Li, Y.; Zhao, Y.; Cheng, H.; Hu, Y.; Shi, G.; Dai, L.; Qu, L., Nitrogen-Doped Graphene Quantum Dots with Oxygen-Rich Functional Groups. *J Am Chem Soc* **2012,** *134* (1), 15-18.

12. Qian, Z.; Ma, J.; Shan, X.; Shao, L.; Zhou, J.; Chen, J.; Feng, H., Surface functionalization of graphene quantum dots with small organic molecules from photoluminescence modulation to bioimaging applications: an experimental and theoretical investigation. *Rsc Adv* **2013,** *3* (34), 14571-14579.

13. Huang, H. D.; Liao, L.; Xu, X.; Zou, M. J.; Liu, F.; Li, N., The electron-transfer based interaction between transition metal ions and photoluminescent graphene quantum dots (GQDs): A platform for metal ion sensing. *Talanta* **2013,** *117*, 152-157.

14. Qu, D.; Zheng, M.; Du, P.; Zhou, Y.; Zhang, L.; Li, D.; Tan, H.; Zhao, Z.; Xie, Z.; Sun, Z., Highly luminescent S, N co-doped graphene quantum dots with broad visible absorption bands for visible light photocatalysts. *Nanoscale* **2013,** *5* (24), 12272-12277.

15. Pearson, R. G., Absolute electronegativity and hardness: application to inorganic chemistry. *Inorg Chem* **1988,** *27* (4), 734-740.

16. Parr, R. G.; Pearson, R. G., Absolute hardness: companion parameter to absolute electronegativity. *J Am Chem Soc* **1983,** *105* (26), 7512-7516.

17. Martell, A. E.; Smith, R. M., *Critical stability constants*. Plenum Press: New York, **1974**; p v. <1-6 >.

Chapter 3

Sensing Solvent Vapors with Carbon Quantum Dots from sp^2 Carbons Soot

3.1. Introduction of Chemiresistor Sensors from Carbon Quantum Dots

Electronic nose detection requires sensors with both great sensitivity and extremely varied selectivity, such that a broad number of analytes can be detected. Chemiresistor are a class of sensors that adsorb analyte molecules and vary their resistance[1] and are often used in electronic nose applications.[2-3] Discrimination between vapors requires a discernable response from a number of detectors, with greater specificity to each vapor improving on identification. With carbon quantum dots a wide range of functionalities can be exhibited so these structures may act as a promising substrate, provided they can be made to respond differentially to a variety of compounds.

Graphene has attracted extensive interest due to its unique physical properties such as exceptional mechanical strength,[4-6] extremely high surface area,[7] excellent thermal and electrical conductivity,[8-9] and robust chemical stability.[10] As carbon is a cheap and abundant element, efficient synthesis methods could provide a wide variety of graphene-based products at a low cost and with minimal environmental impact. Vapor deposition has proven to be an effective means of generating large area films of graphene[11-12] which is ideal for applications where uniformity over volume maters. Other methods, such as physical exfoliation by desorption[13] and, more famously, by pealing layers of graphite off with tape[6] still prove to be a good means of obtaining small amounts of graphene for research purposes. However, if graphene is to be a commercially viable material, synthetic methods must be developed that will allow for a more large-scale synthesis. Lastly, there are high energy techniques, such as

ablation of graphite targets suspended in solvent[14-15] which yield nano-diamonds, and ablation of graphene sheets in a vacuum famously yielding fullerenes[16-17]. The last two are methods for yielding 0D carbon nanoparticles. These methods are top down approaches for the synthesis of carbon materials with focus on one dimensional carbon systems.

The difficulty of processing graphene often necessitates using a precursor material most often graphene oxide (GO). This material can then be reduced to form reduced graphene oxide (rGO) which ideally would have the same properties as that of graphene, but often falls short[18] making for an inefficient cycle. The synthesis of graphene and graphene oxide (GO) has primarily followed a top-down approach, with Hummer's method being one of the most prevalent[19]. Although much improvement has been reported since its original development such as by Chen *et al.*,[20] this method still has the disadvantage of having to use graphene as a precursor. Solvation-assisted exfoliation has been utilized to synthesize large graphene-coated surfaces which can be utilized for the manufacturing of devices.[12, 21] Although these methods are promising for large-scale applications, they still suffer from the same disadvantage of requiring graphene to be broken down as well as post-processing. Because of this shortcoming, bottom-up approaches for synthesizing graphene nanomaterials are drawing extensive attention for large-scale applications.

The most common bottom-up approach for the synthesis of graphene involves the reduction of GO to rGO. GO is both extremely interesting as a precursor to rGO, and in its own right as a material.[22-24] The incredible solubility of GO compared to

that of graphene is one of its main advantages,[25] allowing for facile chemical processing as well as the possibility of elemental doping.[26] Doping of graphene with elements such as, nitrogen, boron, oxygen, sulfur, phosphorous, which could confer even more interesting properties to graphene such as catalytic activity[27] and tuned photo-luminescence.[28] Additionally, bottom up techniques like that of Ju *et al.* does not require a graphene precursor like the method used by Park *et al.* affording its biggest advantage. In order to supersede this problem and inherent limitation, methods to produce graphene and its analogues with more basic precursors will need to be further developed. A variety of bottom-up approaches must be developed which can yield large quantities of graphene, GO, and rGO uniformly and efficiently for applications where graphene quantum dots are the stated goal.

Graphene quantum dots (GQD) are clusters of graphene only a few layers to a single layer thick, with lateral dimensions less than a few hundred nanometers. These structures are made directly from simple chemicals affording them the benefit of not requiring graphene as a precursor. A solution chemistry approach has been developed by the Li group[29-30] that yields very mono-dispersed graphene nanoparticles having similar properties to bulk graphene. Although this method proves to be effective for yielding graphene nanomaterials without the use of graphene as a precursor, however, methods such as this requires a lengthy stepwise process which yields just over 1 %. Graphene quantum dots have also been produced by heating glucose solutions with microwaves, and yield graphene nanoparticles with sizes between 10-21 nm.[15] Evidence for graphitic character is often noted by

observations via FTIR, and XPS spectra, but these nanoparticles often have considerable oxidation making them more akin to graphene oxide nanoparticles with little graphitic character.

Bottom up methods like using carbon from soot, with sources such as natural gas,[31-32] candle soot[33] and biomass (corn stalks)[34] are yielding results. However, attempt to influence sp^2 character directly by using carbon sources with greater sp^2 content has not been made before, which is the focus of this study. Control of the graphitic structure as well as elemental doping with hetero atoms can play a profound roll by directing specificity of the interactions and is well documented to influence catalytic activity.[35-40] Control of these structural characteristics could provide a basis for understanding the influence of doping on the sensing of analytes. We were unable to find any reports of nitrogen doped graphene used to detect vapors in chemsensors. We report here in both characterization as well as sensor applications of carbon quantum dots doped with nitrogen for the facile detection of solvent vapors with a high degree of specificity.

3.2 Experimental

3.2.1 Materials for Resistivity Sensing Procedure for Carbon Quantum Dots

Toluene (99.9 %, Fisher Scientific), nitric acid (HNO_3, 69.8 %, Fisher Scientific), CCl_4 (Sigma Aldrich 99.9 %), $CHCl_3$ (Macron B# 0000067764), CH2Cl2 (HPLC Grade 99.8 % EMD), acetone (Histological Grade, HG, Macron), isopropanol (HG Fisher), methanol (99 % Fisher), ethanol (Reagent Grade J.T. Baker), tetrahydrofuran (HPLC Grade Fisher 99.9 %), Pyridine (99.9 %, Fisher Scientific),

Pipiridine (Acros 99+%), sodium carbonate (Na_2CO_3, 99+%, Aldrich), and sodium hydroxide (NaOH, 99+%, Fisher Scientific) were used as received. Water was supplied from a Barnstead Nanopure Water System (18.3 MΩ cm).

3.2.2 Synthesis of Nitrogen Doped and Undoped Carbon Quantum Dots

Graphene Oxide Nanoparticles were prepared by modifying a procedure used previously by this lab.[32] A repurposed oil lamp with a fiberglass wick was used to burn a minimum of 100 mL of fuel with the addition of a calculated amount of dopant, 20 ml of pyridine. Burns were carried out using a single lamp at a time with a ceramic crucible upturned to catch the soot released from incomplete combustion. Lamps were rinsed with fuel when switching dopants or fuels between burns. The crucible was kept 4 to 5 inches over the wick; and burns lasted for approximately two and half hours. Burns with more than 20 ml of pyridine did not maintain combustion and so soot was not used due to the incomparability of the burns.

Soot was allowed to cool on the stand, after which the soot was scraped off the crucible and used as is without further modification. Oxidation of the soot to nanoparticles was done by weighing 0.35 g of soot into a 500 mL round bottom flask along with 40 mL of concentrated nitric acid diluted with 100 mL of nanopure water. This solution was then stirred for 16 ± 1 hr under reflux and cooled naturally to room temperature. Once cool, solutions were neutralized by using both sodium hydroxide and sodium carbonate. Purification was carried out via dialysis (cutoff mw 2000 Da) for 3 days. Further purification was carried out as flocculates were noted after dialysis. The solution was centrifuged at 5500 rpm for 5 min with the supernatant

being retained. The precipitate was discarded; this process was repeated 4 times. After purification the solution displayed no flocculates and no precipitate after the 4th and often the 3rd cycle. Multiple batches were combined to acquire enough nanoparticles to perform characterization and sensing experiments. Samples are labeled as follows; Toluene soot nanoparticles, TS, pyridine doped nanoparticles produced with 100 ml Toluene with 20 ml of added pyridine are labeled as P20.

3.2.3 Resistivity Setup and Sensing Procedure for Vapor Detection

Solvent setting setup photographed Figure 3.1, is constructed of a 20 ml scintillation vial with twin needles passed through the cap epoxied into place along with an interdigitated electrode. This vial is then completely sealed with epoxy, except the two needles through which N_2 could be added to purge the vessel as well as the analyte solvent can be added via a micro syringe. Epoxy was added to the side of the vial to prevent it from rolling or moving during measurements.

Stock solutions, of 10 mg/ml of the TS and P20 samples, the same two solutions were used to make all films used in the conductivity measurements. Pipetting a 20 μl aliquot was used to create a hemispherical drop over the interdigitated array, which was subsequently dried under a 100 watt bulb. The droplet was large enough to cover the array and did not need to be spread. Samples were remade if they were off-center or deformed when dry. Samples were not recycled for solvent testing purposes only fresh films were used to remove worries about chemical modification or contamination of the particles.

Figure 3.1: Picture of IDA electrode set-up, with coins shown for scale. Needle inlets, two, are located below the IDA electrode which faces up. One needle is large enough to allow for a smaller needle to be threaded through it to add the microliters of solvent.

Instrumentation used:

HRTEM Measurements: High Resolution Transmission Electron Micrographs were taken using a Phillips CN300/FEG operated at 300 kV.

AFM: Atomic Force Microscopy micrographs were taken using a Picoscan 2100.

Raman Measurements: Spectra were taken using a Delta NU 532 nm Raman spectrometer with microscope attachment on glass slides, aluminum foil and CdSe. Different substrates were compared, no substrate effect was observed. Samples were deposited from solution in water and dried under a 100 w flood light.

Dynamic Light Scattering: DLS data was taken using DynaPro Nano Star at multiple concentrations, a minimum of three results averaged. Only values that were present in multiple trials were used. Small percent by mass or percent by intensity values, less than 2 %, were discarded as were values larger than 1 μm in diameter, which were always less than 5 % of the intensity at maximum and unrepeatable run to run.

X-Ray Photoelectron Spectroscopy: XPS measurements were done using a PHI 5400/XPS instrument equipped with an Al Kα source operated at 350 W and at 10^{-9} Torr.

FTIR Measurements: FTIR spectra were taken using a Perkin-Elmer Precision Spectrum One spectrometer. Samples were deposited from solution in water onto a CdSe window and dried under a 100 W flood light. Spectra were taken at 1 cm^{-1} resolution and 8 scans were taken and averaged.

UV-Vis Measurements: Spectra were taken using a HP 8452A diode array spectrometer with a resolution of 2 nm. Concentration was adjusted till the absorbance was near 1 at 250 nm. PL measurements were done subsequently on the same sample at the same concentration. Spectra are shown normalized.

Photoluminescence Measurements: PL measurements were taken using a Varian Cary Eclipse Fluorescence Spectrophotometer and normalized for concentration using absorbance values at 250 nm the same normalization constant was used to normalize both sets of spectra, spectra are shown normalized.

Resistivity Measurements: Measurements were conducted using an IDA electrode (25 pairs 3 mm x 5 μm x5 μm ABTECH). Sweeps were conducted going from -0.8 volts to 0.8 volts at 50 mV per second with the reference electrode being placed with the counter electrode. Films were deposited from a solution 1 mg / ml using 20 μl, deposited using an Accumax pipette resulting in a final film considerably thicker than the 5 μm IDA finger and covering it entirely. The solution was dried under a 120 W incandescent bulb for 30+ min and then transferred to the vial (vial was screwed on over the IDA). 2 min of nitrogen is flowed through the cell to remove residual moisture and purge the cell of any water vapor. Initial conductivity is then assessed and normalized against.

3.3 Results and Discussion of Vapor Sensing Experiments

Figures 3.2 & 3.3 shows a current responses to linear sweep voltammetry with particles TS and P20, with sweeps from -0.8 to +0.8 volts, with steady additions of $CHCl_3$ added via Hamilton microliter syringe at ambient temperature in 1 μL increments to start. Allowing 5 min evaporation time between additions and taking the scan there after, solvents readily evaporated in that time with the vial relatively unsaturated. The response was calculated using all the data points between -0.6 and -0.35 volts and used to get a slope, R, the ensemble resistance, which is then used to calculate the ensemble conductivity shown in Eq(1). Equation 1 has L is the IDA electrode interfinger gap (5 μm), and A is the film cross-section area approximated by (finger height 5 μm x finger length 3 mm).

$$\text{Equation 1} \quad \sigma = \frac{1}{49R}\frac{L}{A}$$

The films response to solvents showed remarkable response to a wide variety of solvents with incredible differences in sensitivity due to very small doping levels. Although not competitive with other chemiresistor on sensitivity our chemical specificity is quite remarkable. In addition our facile doping method resulted in some dramatic conductivity differences between samples which we ascribe to the nitrogen doped and undoped nature of the samples. Using such a simple doping method and achieving such profound results shows promise as a sensing technique if the method can be optimized. Other hetero atoms may provide even more selectivity channels.

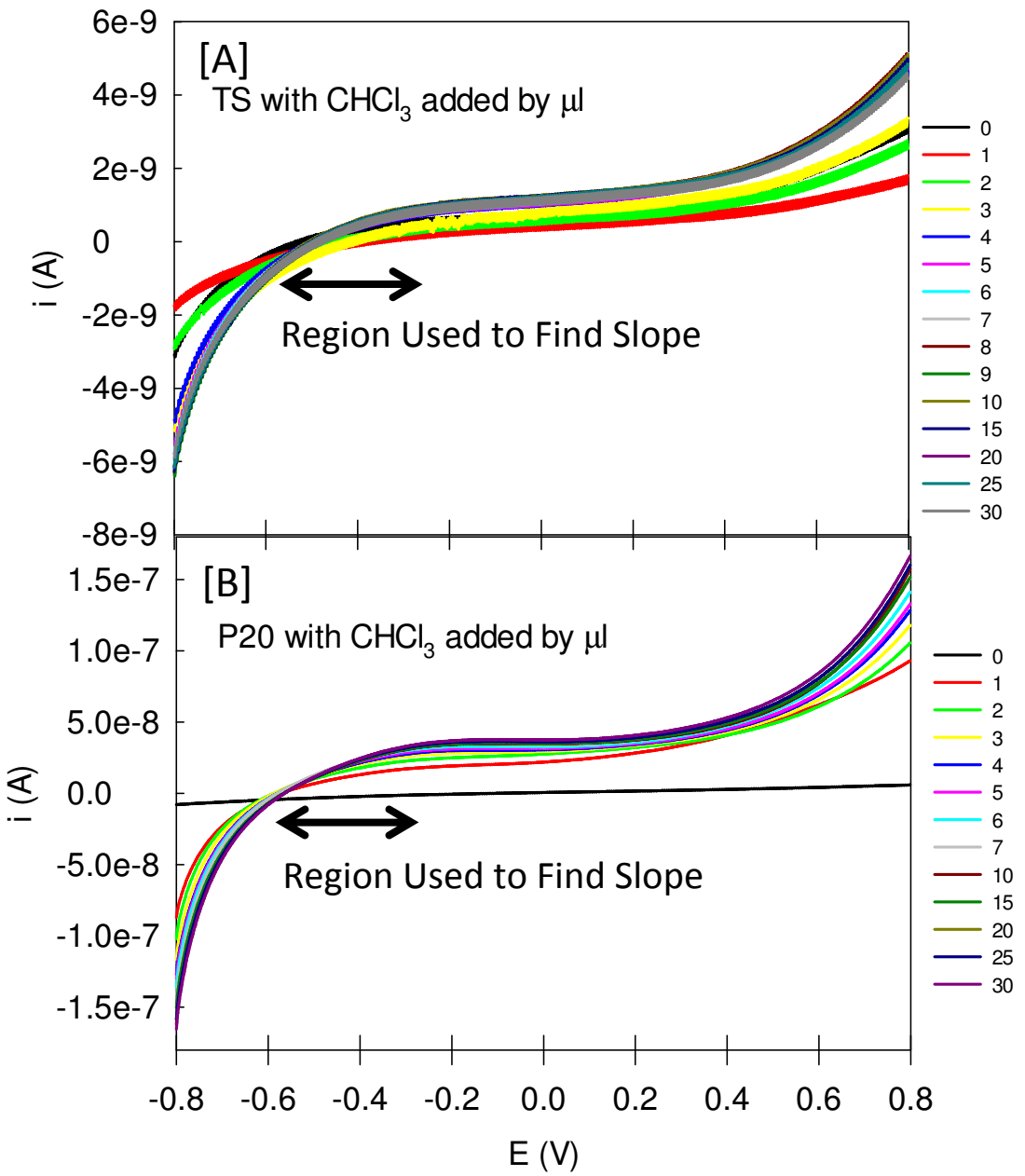

Figure 3.2: Linear sweep voltammograms are run from negative to positive. Plots A&B are with additions of chloroform and labeled with each addition. The conductivity response for these two experiments is shown in Figure 3.4, the slope between -0.6 and 0.35 volts is used to make Figure 3.6.

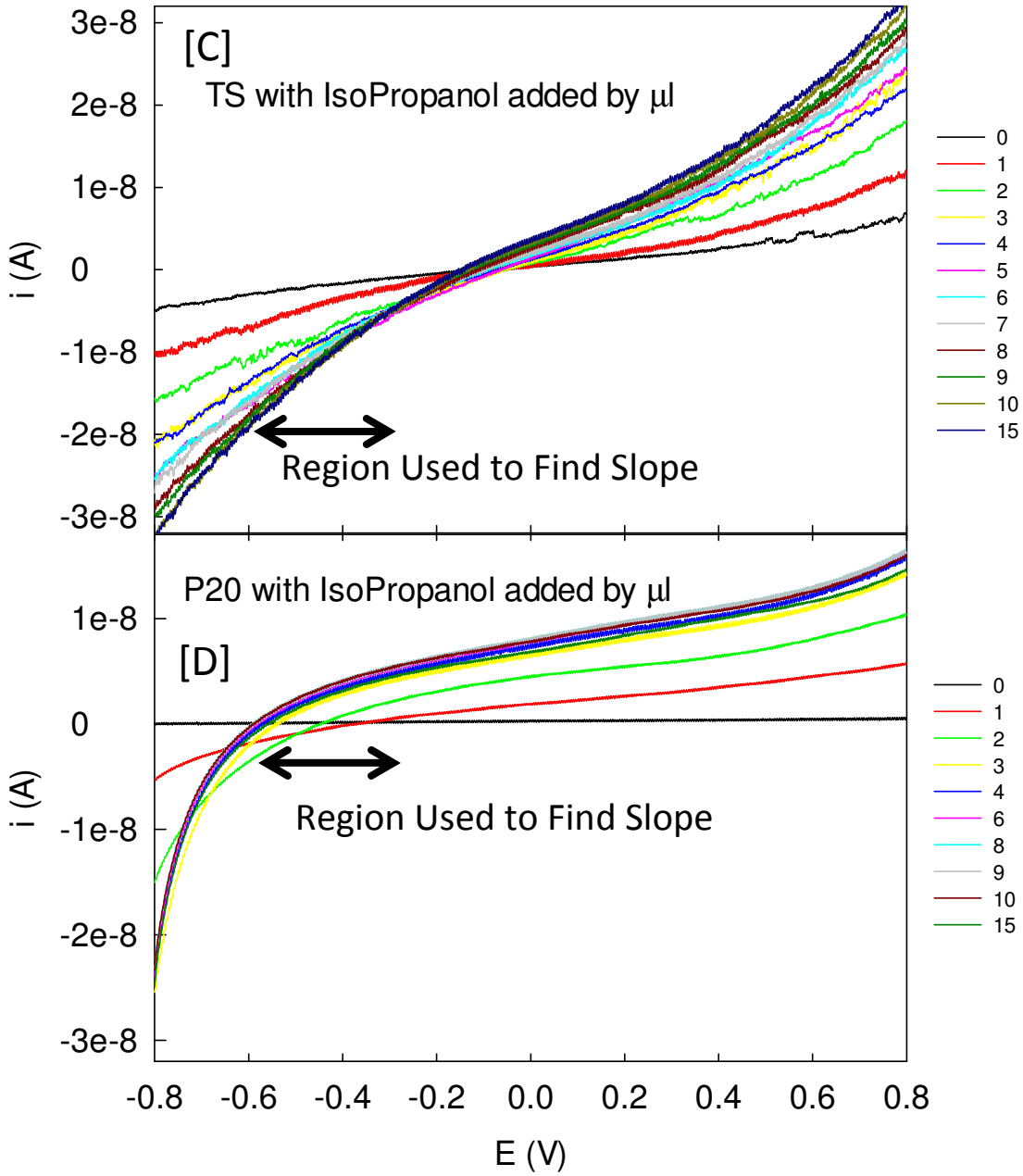

Figure 3.3: Linear sweep voltammograms are run from negative to positive. Plots C&D are with additions of isopropanol and labeled with each addition. The conductivity response for these four experiments is shown in Figure 3.5, the slope between -0.6 and 0.35 volts is used to make Figure 3.6.

The region between -0.6 and -0.35 volts shows the least current offset across all samples. The initial slope is taken, after 2 min of drying with nitrogen gas to assure that no appreciable water vapor remains within the vial; the nitrogen also further dries the sample. The response to drying by nitrogen is rapid showing little change after the first 30 seconds. The initial slope is normalized to 1 and subsequent slopes being plotted as percent changes there from. The slope is proportional to the conductivity and the percent change is plotted vs. solvent volume to give response curves. The value for the second 1 μL addition was used as the response for all samples, except THF where the scan was corrupted and so the third 1 μL addition was used for both samples. Figure 3.4 displays slope change percentages in response to additions of chloroform to the sample vial, pictured in Figure 3.2.

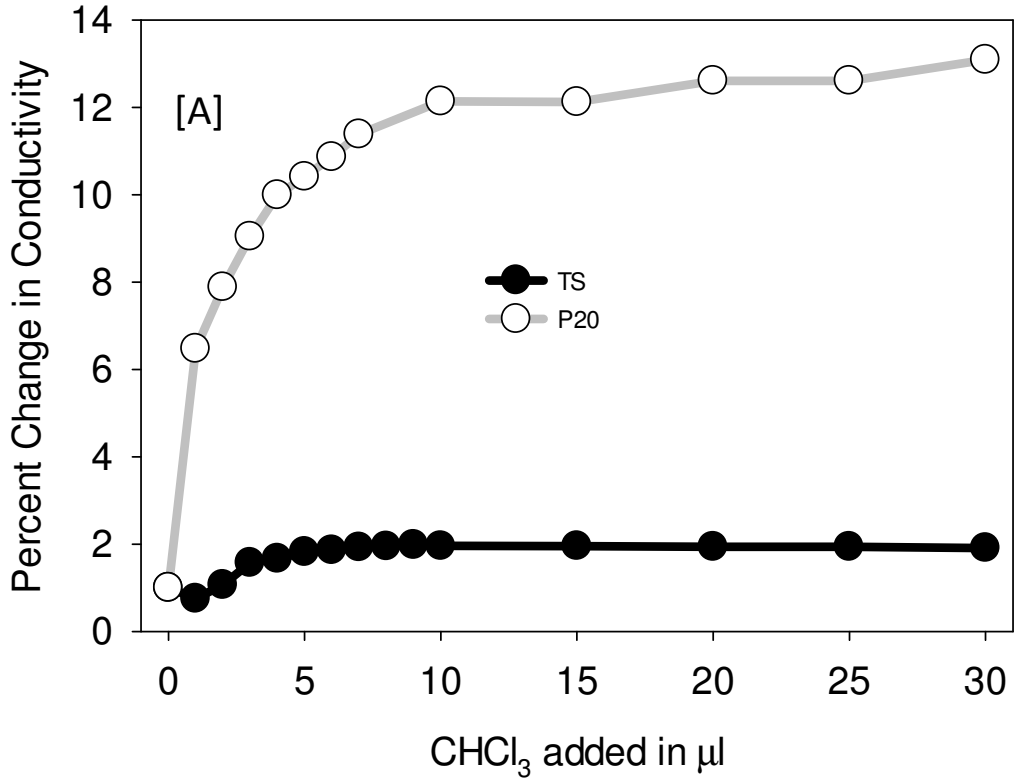

Figure 3.4: Percent change in conductivity is normalized to initial conductivity for each film sample is plotted on the y-axis, added solvent volume is plotted in microliters on the x-axis. The response with additions of chloroform is shown.

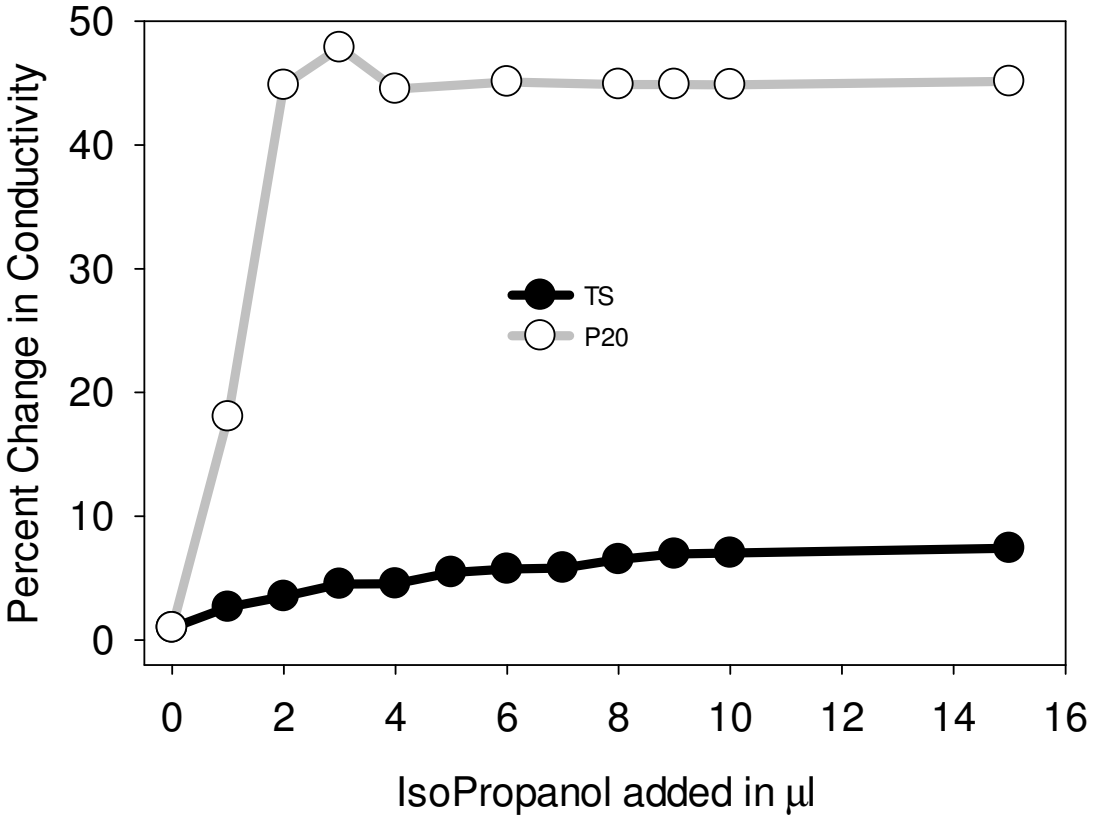

Figure 3.5: Percent change in conductivity is normalized to initial conductivity for each film sample is plotted on the y-axis, added solvent volume is plotted in microliters on the x-axis. The response with additions of isopropanol is shown.

We attribute the increase in conductivity of the sample to improved redox hopping. Plotting the second microliter addition accounts for induction periods present in some samples for the first microliter. Note, for the TS sample, Figure 3.4, the first addition shows a slight decline not representative of the samples over all response. Supplemental information contains plots for all samples. Not all samples could be tested out to 30 µL, which was treated as the end point for most samples, due to saturation of the vapor. Comparison at saturation would be inconsistent as the saturation point varies by volume sample to sample.

Plotting the response of the second addition of solvent vs. the solvents themselves, ordered by increasing polarizability, yields Figure 3.6. The figure shows a trend for both samples in their response to solvents relative polarity. The samples are not soluble in any of these solvents, only water. However visually the samples do look moistened to the eye by exposure to solvent vapors but no corresponding trend was observed.

The conductivity response of most chemiresistors is exactly the opposite of what we observe, where the addition of vapor causes a decrease in conductivity through a number of mechanisms. Swelling is most often cited as the cause by increases distances between conductive elements and thereby reducing conductivity. A second mechanism is noted working by altering the band structure of the material[41].

We see a strong increase in conductivity for samples interacting with the solvent vapor. Miller *et al.* observe similar conductivity increases for polymer systems[42] and even graphene oxide systems.[43] The Miller *et al.* point to a mechanism of redox hoping and conjugated polymers. They state that some of their systems show increases of conductivity by up to a factor of 10^6. Although our samples do not show such profound increases in conductivity we do show remarkable selectivity responses. For example the response to ethanol with the TS sample is three times that of the P20 particles. The stabilization of redox hopping sites makes sense for that of the pyridine doped sample, P20 with respect to sensitivity to piperidine and pyridine. Interactions between nitrogen in the analyte likely stabilize the redox sites by providing an electron donor pair at the right energy. An explanation for the

sensitivity of the P20 sample to isopropanol is more difficult to explain, perhaps conformational changes in the film allow for greater contact between nanoparticles increasing conductivity. It is noted that the TS sample also shows increasing conductivity when exposed to isopropanol. Miller *et al.* also point to morphological changes due in great part to improved plasticization that could improve conductivity. Our samples experienced strong hysteresis effects, we ascribe to a lack of crosslinking between particles or suspension in a matrix, and so cycling (exposure with drying and re-exposure) was not observed to have reproducible results.

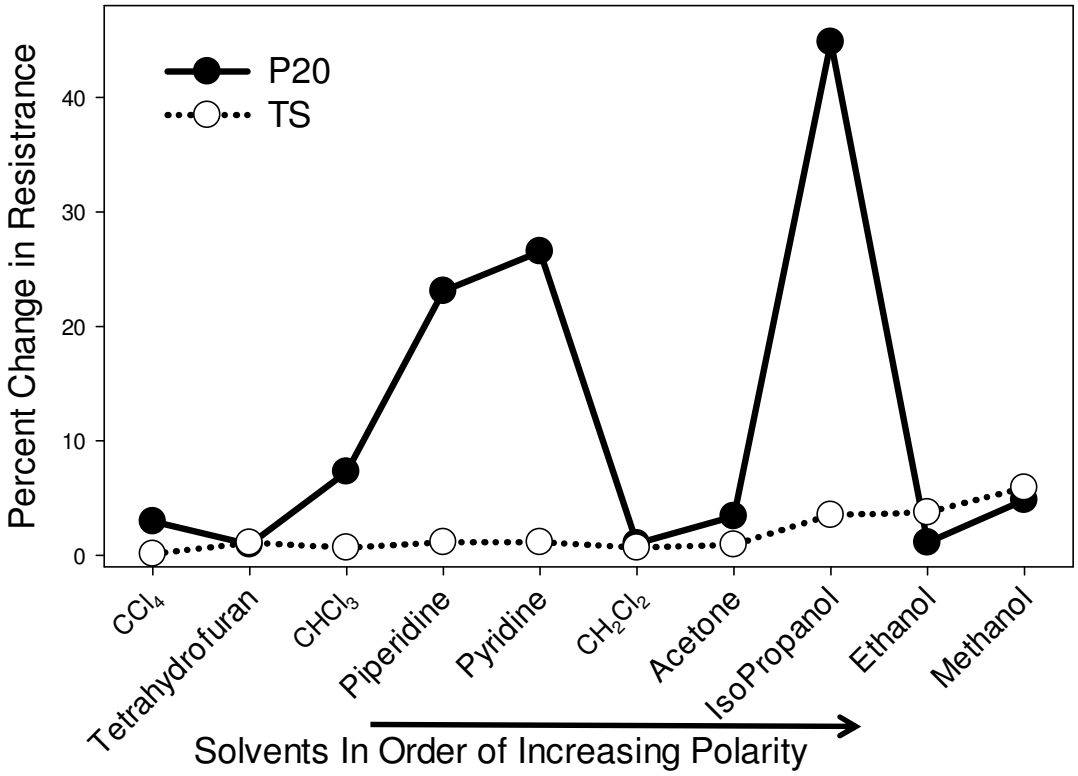

Figure 3.6: Plots of percent change in conductivity of each sample for the 2nd microliter (3rd in the case of tetrahydrofuran) addition is plotted with respect to the solvents which have been put in order of relative polarity, increasing to the right.

Utilization as sensors is one possible application of these particles, also of interest is the particles themselves. Carbon quantum dots produced from sp^2-carbon fuels showed a distinct layered structure, notable via TEM and AFM micrographs in Figure 5 and 6 respectively. The samples all demonstrate planar morphologies with distinct thicknesses. The thicknesses observed are also consistent with layered structures similar to that of graphene oxide, often close to the 0.4 nm height of GO, Figure 3.8. Modal height values become apparent when observed as a histogram, Figure 3.9. Layering though does not necessarily imply graphitic character.

Dynamic light scattering, DLS, measures the particle ensemble and the data reflects the finding from TEM and AFM measurements, as shown in Table 3.1. The as-prepared nanoparticles are significantly larger than those produced previously using natural gas soot, radii of ~21 nm.[15] Due to the inhomogeneous nature of the nanoparticles, modeling the nanoparticles as amorphic flat sheets is beyond the capacity of the DLS, possibly resulting in larger or smaller hydrodynamic radii than would be found using a more discerning method.

Raman spectra, Figure 3.10, show very distinct evidence for the presence of graphitic carbon. With both G and D bands clearly evident in both sets of nanoparticles the ratio between them is consistent or even better than that of graphene oxide produced from graphene directly by other groups.[39, 44] These are unreduced particles and display these peaks by simply drying directly from aqueous solutions. Ratio's for G : D bands are calculated using heights of the G and D peaks at 1357 and 1600 cm^{-1} after baseline correction and normalization using the D peak to standardize the peak sizes for plotting purposes, Table 3.1. Of possible concern for interpretation of the Raman data is the possibility of contamination with aromatic structures, such as coronene, phenanthrene, and others. However many of these have extremely strong photoluminescent properties that would make them evident if they comprised enough of the sample to contribute to the Raman spectrum. Also these aromatic molecules often have side bands that would have similar strength to those of the G and D bands, none of which were observed.

Absorption of conjugated alkenes is observed at 1600 cm^{-1} in the FTIR, Figure 3.13, which would be expected of samples containing graphitic carbon shown in supplemental information. Amorphous carbon is difficult to observe via FTIR or Raman and so may comprise a significant portion of the sample which is difficult to assess through multiple methods. Because of the mixed morphology of the nanoparticles it is likely that the graphitic domain within each nanoparticle is relatively small possibly with more than one domain per nanoparticle.

Fitting the pyridinic nitrogen in the toluene soot, TS, sample is shown mostly to act as an upper bound on the nitrogen content as the noise is relatively high the peak could be non-extant. The peak near 406 eV is ascribed to nitro groups bound to the carbon lattice.[45-47] The nitration is likely imparted by Nitric acid and helps to maintain the strong solubility we see for these particles. Analysis of the XPS spectra shows slight discrepancies between carbon content and oxygen content, when considering oxidized carbon vs. oxygen content. Sensitivity factors of 0.296, 0.711 and 0.477 were used for carbon, nitrogen, and oxygen respectively, Table 3.2.

Strong trends in the photoluminesecene properties are not noted. Both nanoparticles are excited between 315 and 320 nm and emit between 305 and 320 nm. The samples' UV-Vis profiles were normalized at 250 nm, the normalization value was used to scale the PL spectra, both sets of spectra are shown in Figure 3.11 along with the normalized UV-Vis spectra inset.

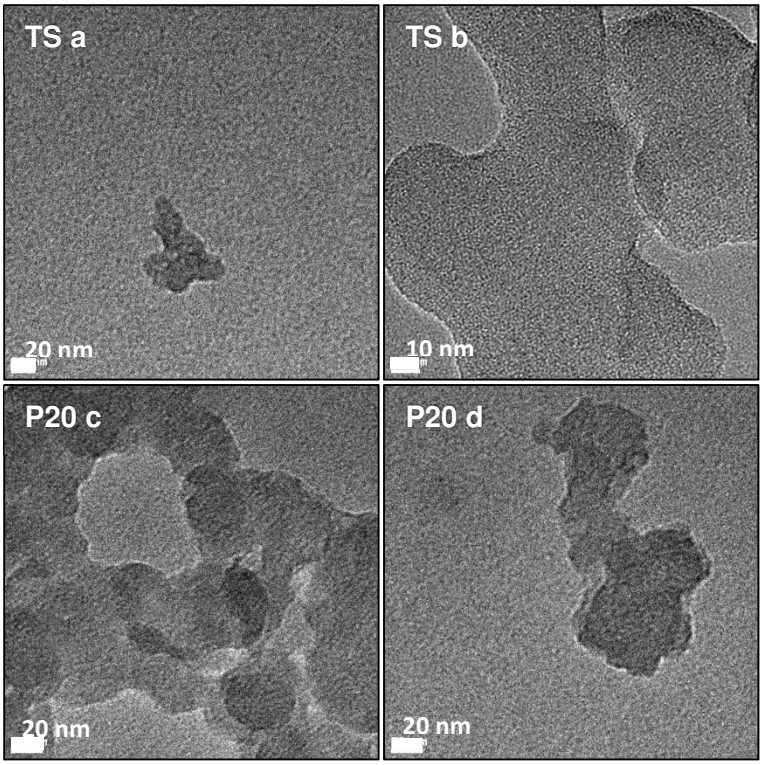

Figure 3.7: TEM micrographs of carbon soot nanoparticles sizes were similar to those observed via DLS and AFM. Micro graphs a & b are of TS soot nanoparticles c & d as sample P20. Layering can easily be observed for many of the samples both in TEM as well as AFM. Micrographs were all taken using Silicon substrate.

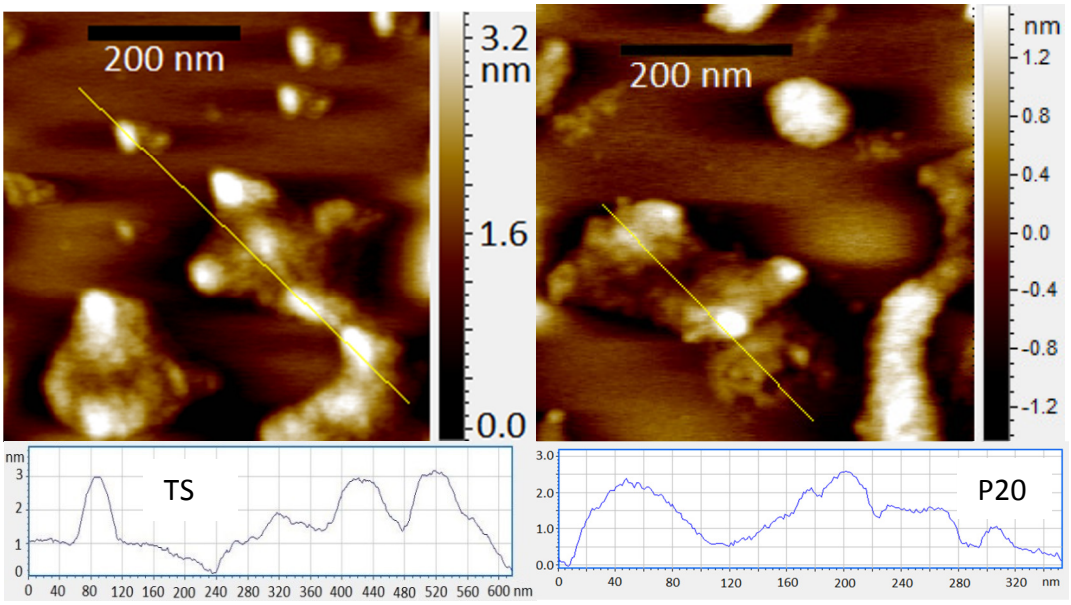

Figure 3.8: AFM micrographs of carbon soot nanoparticles taken on mica. Note that the lateral dimension of the particles far exceeds the height of individual nanoparticles. The particles are likely semi amorphic and acquire a more planer shape when dry. Graphitic regions are likely interspersed with less aromatic regions.

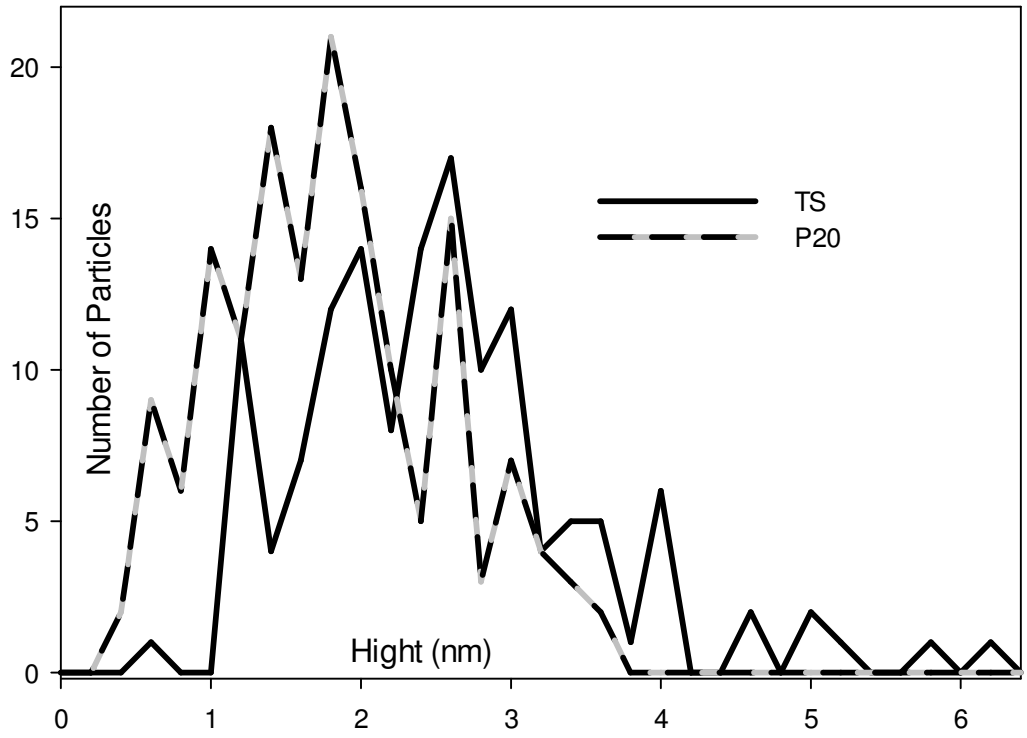

Figure 3.9: Histograms of particles measured for both TS and P20 nanoparticles. Note intermittent height values displayed by particles, spacing between peaks is most often multiples of 0.4 nm measured in 0.2 nm intervals. Values are tabulated in Table 3.1.

Table 3.1: Tabulated heights of nanoparticles as measured by AFM, Raman & DLS Data

	Average Height (nm)	Median Height (nm)	Standard Deviation (nm)	Mode (nm)	# of particles	Range (nm)
TS	2.5	2.4	1.0	2.6	141	6.2 – 0.6
P20	1.6	1.8	0.8	1.6	159	4.0 – 0.2

Raman & DLS Data

	Ratio G : D	Sample	Average D (nm)	Primary D (nm)	Comp by Mass	Secondary D (nm)	% Comp by Mass
Toluene	1.12	TS	182.1	229.9	57.0%	106.0	43.1%
P20	1.09	P20	230.1	230.1	100.0%		

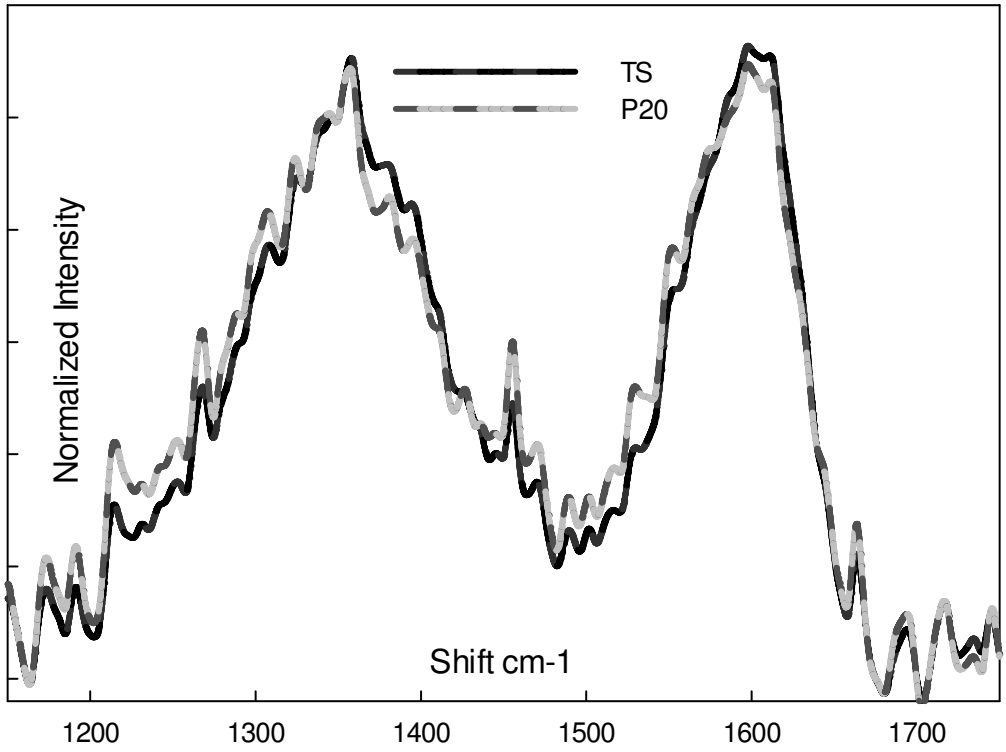

Figure 3.10: Raman spectra for TS and P20 nanoparticles, note that the spectra have been baseline corrected and normalized at 1350 cm^{-1} to remove differences in total intensity response. The G : D ratio is calculated at 1357 and 1600 cm^{-1} after this baseline correction, and shown for in Table 3.1.

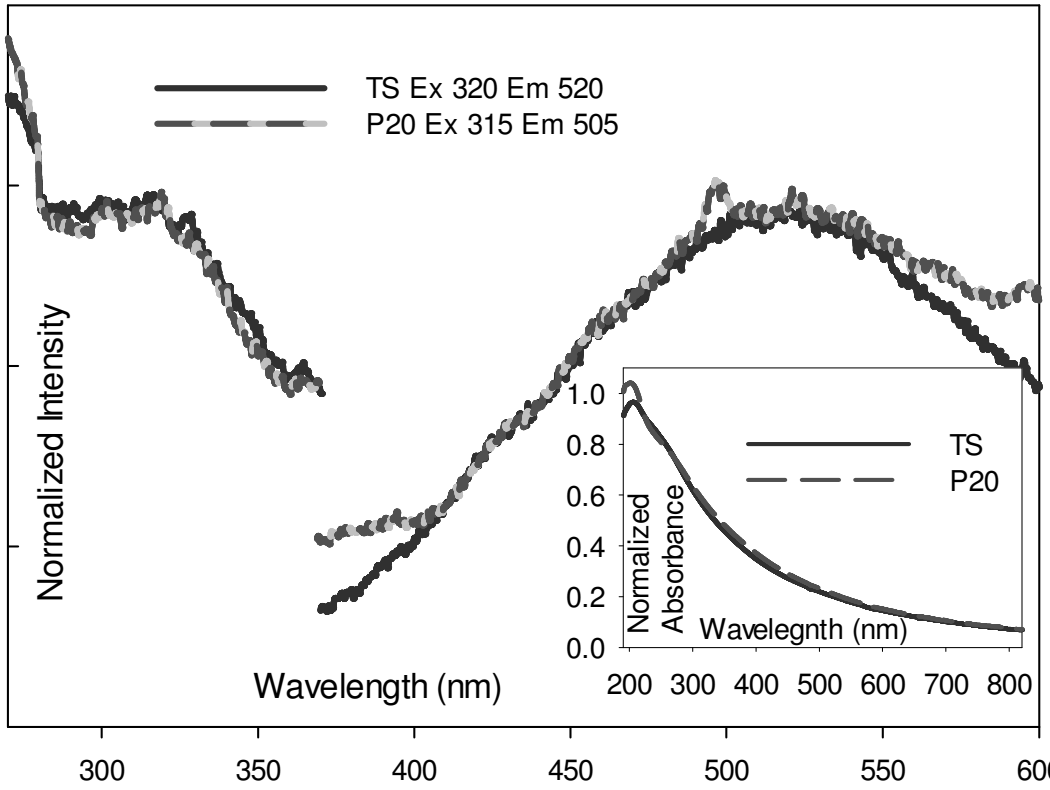

Figure 3.11: Photoluminescence for the both TS and P20 nanoparticles look quite similar. Inset is the UV-Vis profile of the nanoparticles base lined at 250 nm using a single scalar multiplier which was used for the photo luminescence data as well. Excitation and emission values are; TS excitation 320 nm & emission 520 nm, P20 excitation 315 nm & emission 505 nm.

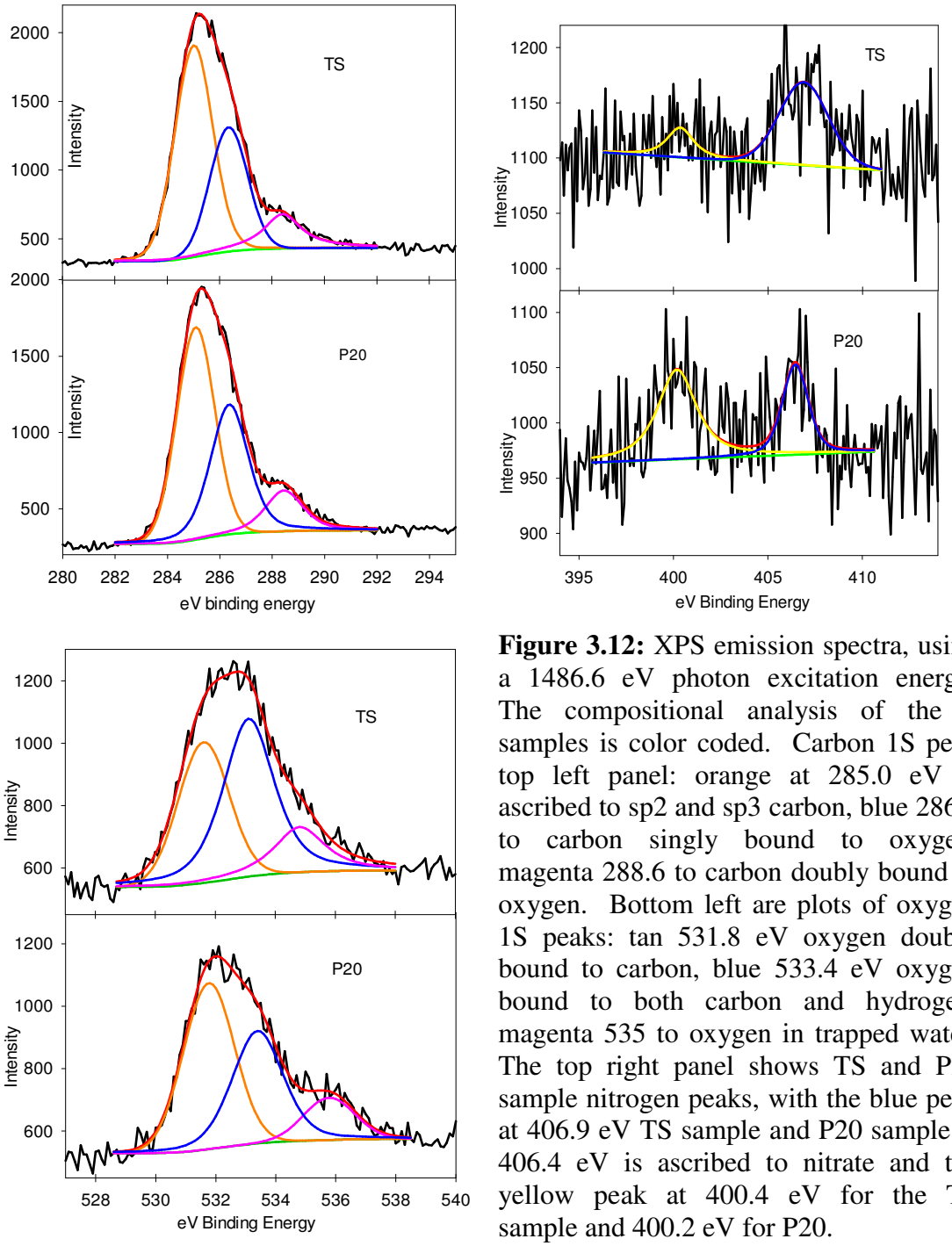

Figure 3.12: XPS emission spectra, using a 1486.6 eV photon excitation energy. The compositional analysis of the 2 samples is color coded. Carbon 1S peak top left panel: orange at 285.0 eV is ascribed to sp2 and sp3 carbon, blue 286.3 to carbon singly bound to oxygen, magenta 288.6 to carbon doubly bound to oxygen. Bottom left are plots of oxygen 1S peaks: tan 531.8 eV oxygen doubly bound to carbon, blue 533.4 eV oxygen bound to both carbon and hydrogen, magenta 535 to oxygen in trapped water. The top right panel shows TS and P20 sample nitrogen peaks, with the blue peak at 406.9 eV TS sample and P20 sample at 406.4 eV is ascribed to nitrate and the yellow peak at 400.4 eV for the TS sample and 400.2 eV for P20.

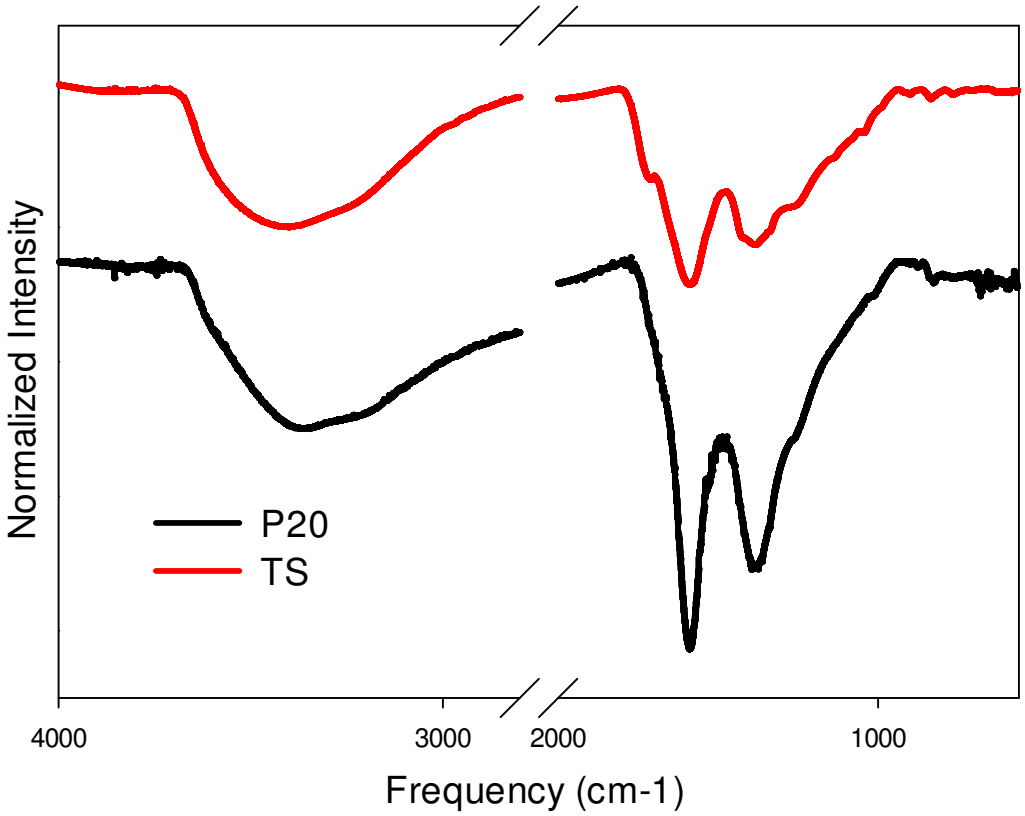

Figure 3.13: FTIR spectra for TA and P20 nanoparticles, the broad peak at 3400 cm-1 is the vibrational stretch of the O-H bond present in alcohols and carboxylic moiety's (and residual water) within the sample. The shoulder in the peak is indicative of carboxylic acid but the presence of other O-H moieties is also likely. A peak centered at 1734 cm-1 could be cyclo-ketones there is a peak near 1275 cm-1 to corroborate this there is also a strong peak at 1387 cm-1 to corroborate carboxylic acid.

Table 3.2: Results of XPS experiments on Carbon Nanoparticles

Sample	Peak Allocation	Position (eV)	Peak Area	% Composition
	Carbon SP2 &			
TS	SP3	285.02	2763.2	43.3%
C : O	**C**-O	286.35	1798.9	28.2%
4.5	O**C**O or **C**=O	288.40	626.1	9.8%
C : N	Ketone	531.77	1120.7	7.3%
125.1	Alcohol	533.43	1649.8	10.8%
CO & COO				
: O	Water	534.81	425.1	
2.1	Nitrate	406.89	252.1	
	Prydinic &			
	Pyrrolic	400.35	66.8	0.6%
	Carbon SP2 &			
P20	SP3	285.06	2529.2	43.8%
C : O	**C**-O	286.34	1651.3	28.6%
5.7	O**C**O or **C**=O	288.41	578.8	10.0%
C : N	Ketone	531.77	1131.5	8.2%
27.0	Alcohol	533.39	877.0	6.3%
CO & COO				
: O	Water	535.78	291.7	
2.7	Nitrate	406.45	166.6	
	Prydinic &			
	Pyrrolic	400.21	284.1	3.1%

3.4 Conclusions Concerning Vapor Sensing Experiments

Carbon nanoparticles were made displaying graphitic like character as observed by Raman, XPS and FTIR. Doping with nitrogen was carried out by adding nitrogen containing compounds to the precursor fuel which resulted in increased pyridinic and pyrolic. All samples were noted to have strong scattering via both PL and UV-Vis profiles indicative of nanoparticles. DLS and TEM both observed larger nanoparticles than those achieved by other bottom up methods, with TEM, and AFM showing that they were thin structures. The method proved efficacious, yielding both larger nanoparticles than those normally produced using bottom up techniques but also substantially increasing their sp^2 carbon content. The particles were also used to form a thin film over an interdigitated array which was found to be sensitized to different solvents by addition of nitrogen into the carbon nanoparticles toward Nitrogen containing compounds as well as chlorocarbons making it ideal for electronic nose applications.

3.7 References

1. Wilson, A. D.; Baietto, M., Applications and Advances in Electronic-Nose Technologies. *Sensors-Basel* **2009,** *9* (7), 5099-5148.

2. Ramgir, N. S., Electronic Nose Based on Nanomaterials: Issues, Challenges, and Prospects. *ISRN Nanomaterials* **2013,** *2013*, 21.

3. Chiu, S.-W.; Tang, K.-T., Towards a Chemiresistive Sensor-Integrated Electronic Nose: A Review. *Sensors (Basel, Switzerland)* **2013,** *13* (10), 14214-14247.

4. Medhekar, N. V.; Ramasubramaniam, A.; Ruoff, R. S.; Shenoy, V. B., Hydrogen bond networks in graphene oxide composite paper: structure and mechanical properties. *Acs Nano* **2010,** *4* (4), 2300-6.

5. Lee, C.; Wei, X.; Kysar, J. W.; Hone, J., Measurement of the elastic properties and intrinsic strength of monolayer graphene. *Science* **2008,** *321* (5887), 385-8.

6. Geim, A. K.; Novoselov, K. S., The rise of graphene. *Nat Mater* **2007,** *6* (3), 183-91.

7. Dreyer, D. R.; Jia, H. P.; Todd, A. D.; Geng, J.; Bielawski, C. W., Graphite oxide: a selective and highly efficient oxidant of thiols and sulfides. *Organic & biomolecular chemistry* **2011,** *9* (21), 7292-5.

8. Wei, Z.; Wang, D.; Kim, S.; Kim, S. Y.; Hu, Y.; Yakes, M. K.; Laracuente, A. R.; Dai, Z.; Marder, S. R.; Berger, C.; King, W. P.; de Heer, W. A.; Sheehan, P. E.; Riedo, E., Nanoscale tunable reduction of graphene oxide for graphene electronics. *Science* **2010,** *328* (5984), 1373-6.

9. Eda, G.; Fanchini, G.; Chhowalla, M., Large-area ultrathin films of reduced graphene oxide as a transparent and flexible electronic material. *Nature nanotechnology* **2008,** *3* (5), 270-4.

10. Kim, T. Y.; Lee, H. W.; Stoller, M.; Dreyer, D. R.; Bielawski, C. W.; Ruoff, R. S.; Suh, K. S., High-performance supercapacitors based on poly(ionic liquid)-modified graphene electrodes. *Acs Nano* **2011,** *5* (1), 436-42.

11. Bae, S.; Kim, H.; Lee, Y.; Xu, X.; Park, J.-S.; Zheng, Y.; Balakrishnan, J.; Lei, T.; Ri Kim, H.; Song, Y. I.; Kim, Y.-J.; Kim, K. S.; Ozyilmaz, B.; Ahn, J.-H.; Hong, B. H.; Iijima, S., Roll-to-roll production of 30-inch graphene films for transparent electrodes. *Nat Nano* **2010,** *5* (8), 574-578.

12. Kim, K. S.; Zhao, Y.; Jang, H.; Lee, S. Y.; Kim, J. M.; Kim, K. S.; Ahn, J.-H.; Kim, P.; Choi, J.-Y.; Hong, B. H., Large-scale pattern growth of graphene films for stretchable transparent electrodes. *Nature* **2009,** *457* (7230), 706-710.
13. McAllister, M. J.; Li, J.-L.; Adamson, D. H.; Schniepp, H. C.; Abdala, A. A.; Liu, J.; Herrera-Alonso, M.; Milius, D. L.; Car, R.; Prud'homme, R. K.; Aksay, I. A., Single Sheet Functionalized Graphene by Oxidation and Thermal Expansion of Graphite. *Chem Mater* **2007,** *19* (18), 4396-4404.

14. Sun, J.; Hu, S.-L.; Du, X.-W.; Lei, Y.-W.; Jiang, L., Ultrafine diamond synthesized by long-pulse-width laser. *Appl Phys Lett* **2006,** *89* (18), 183115-183115-3.

15. Hu, S.-L.; Niu, K.-Y.; Sun, J.; Yang, J.; Zhao, N.-Q.; Du, X.-W., One-step synthesis of fluorescent carbon nanoparticles by laser irradiation. *J Mater Chem* **2009,** *19* (4), 484-488.

16. Kroto, H. W.; Heath, J. R.; O'Brien, S. C.; Curl, R. F.; Smalley, R. E., C60: Buckminsterfullerene. *Nature* **1985,** *318* (6042), 162-163.

17. Kozlov, B. N.; Kirillov, S. N.; Mamyrin, B. A. In *Formation of fullerenes in laser ablation of graphite in a vacuum*, 1997; pp 233-238.

18. Gómez-Navarro, C.; Weitz, R. T.; Bittner, A. M.; Scolari, M.; Mews, A.; Burghard, M.; Kern, K., Electronic Transport Properties of Individual Chemically Reduced Graphene Oxide Sheets. *Nano Lett* **2007,** *7* (11), 3499-3503.

19. Hummers, W. S.; Offeman, R. E., Preparation of Graphitic Oxide. *J Am Chem Soc* **1958,** *80* (6), 1339-1339.

20. Chen, J.; Yao, B.; Li, C.; Shi, G., An improved Hummers method for eco-friendly synthesis of graphene oxide. *Carbon* **2013,** *64* (0), 225-229.

21. Lotya, M.; Hernandez, Y.; King, P. J.; Smith, R. J.; Nicolosi, V.; Karlsson, L. S.; Blighe, F. M.; De, S.; Wang, Z.; McGovern, I. T.; Duesberg, G. S.; Coleman, J. N., Liquid phase production of graphene by exfoliation of graphite in surfactant/water solutions. *Journal of the American Chemical Society* **2009,** *131* (10), 3611-20.

22. Suk, J. W.; Piner, R. D.; An, J.; Ruoff, R. S., Mechanical properties of monolayer graphene oxide. *Acs Nano* **2010,** *4* (11), 6557-64.

23. Jung, I.; Dikin, D. A.; Piner, R. D.; Ruoff, R. S., Tunable electrical conductivity of individual graphene oxide sheets reduced at "low" temperatures. *Nano letters* **2008,** *8* (12), 4283-7.

24. Dikin, D. A.; Stankovich, S.; Zimney, E. J.; Piner, R. D.; Dommett, G. H.; Evmenenko, G.; Nguyen, S. T.; Ruoff, R. S., Preparation and characterization of graphene oxide paper. *Nature* **2007,** *448* (7152), 457-60.

25. Park, S.; An, J.; Jung, I.; Piner, R. D.; An, S. J.; Li, X.; Velamakanni, A.; Ruoff, R. S., Colloidal suspensions of highly reduced graphene oxide in a wide variety of organic solvents. *Nano letters* **2009,** *9* (4), 1593-7.

26. Li, X.; Wang, H.; Robinson, J. T.; Sanchez, H.; Diankov, G.; Dai, H., Simultaneous Nitrogen Doping and Reduction of Graphene Oxide. *J Am Chem Soc* **2009,** *131* (43), 15939-15944.

27. Park, J. E.; Jang, Y. J.; Kim, Y. J.; Song, M. S.; Yoon, S.; Kim, D. H.; Kim, S. J., Sulfur-doped graphene as a potential alternative metal-free electrocatalyst and Pt-catalyst supporting material for oxygen reduction reaction. *Phys Chem Chem Phys* **2013,** *16* (1), 103-9.

28. Ju, J.; Chen, W., Synthesis of highly fluorescent nitrogen-doped graphene quantum dots for sensitive, label-free detection of Fe (III) in aqueous media. *Biosensors and Bioelectronics* **2014,** *58* (0), 219-225.

29. Li, L.; Wu, G.; Yang, G.; Peng, J.; Zhao, J.; Zhu, J.-J., Focusing on luminescent graphene quantum dots: current status and future perspectives. *Nanoscale* **2013,** *5* (10), 4015-4039.

30. Yan, X.; Cui, X.; Li, B.; Li, L.-s., Large, Solution-Processable Graphene Quantum Dots as Light Absorbers for Photovoltaics. *Nano Lett* **2010,** *10* (5), 1869-1873.

31. Huang, J.; Deming, C. P.; Song, Y.; Kang, X.; Zhou, Z. Y.; Chen, S., Chemical analysis of
surface oxygenated moieties of fluorescent carbon nanoparticles. *Nanoscale* **2012,** *4* (3), 1010-5.

32. Tian, L.; Ghosh, D.; Chen, W.; Pradhan, S.; Chang, X.; Chen, S., Nanosized Carbon Particles From Natural Gas Soot. *Chem Mater* **2009,** *21* (13), 2803-2809.

33. Su, Z.; Zhou, W.; Zhang, Y., New insight into the soot nanoparticles in a candle flame. *Chemical communications* **2011,** *47* (16), 4700-2.

34. Li, Y.; Xu, L.; Chen, T.; Liu, X.; Xu, Z.; Zhang, H., Carbon nanoparticles from corn stalk soot and its novel application as stationary phase of hydrophilic interaction chromatography and per aqueous liquid chromatography. *Analytica chimica acta* **2012,** *726*, 102-8.

35. Lin, Z. Y.; Waller, G. H.; Liu, Y.; Liu, M. L.; Wong, C. P., 3D Nitrogen-doped graphene prepared by pyrolysis of graphene oxide with polypyrrole for electrocatalysis of oxygen reduction reaction. *Nano Energy* **2013,** *2* (2), 241-248.

36. Lin, Z. Y.; Waller, G.; Liu, Y.; Liu, M. L.; Wong, C. P., Facile Synthesis of Nitrogen-Doped Graphene via Pyrolysis of Graphene Oxide and Urea, and its Electrocatalytic Activity toward the Oxygen-Reduction Reaction. *Adv Energy Mater* **2012,** *2* (7), 884-888.

37. Shao, Y. Y.; Zhang, S.; Engelhard, M. H.; Li, G. S.; Shao, G. C.; Wang, Y.; Liu, J.; Aksay, I. A.; Lin, Y. H., Nitrogen-doped graphene and its electrochemical applications. *J Mater Chem* **2010,** *20* (35), 7491-7496.

38. Luo, Z. M.; Yang, D. L.; Qi, G. Q.; Shang, J. Z.; Yang, H. P.; Wang, Y. L.; Yuwen, L. H.; Yu, T.; Huang, W.; Wang, L. H., Microwave-assisted solvothermal preparation of nitrogen and sulfur co-doped reduced graphene oxide and graphene quantum dots hybrids for highly efficient oxygen reduction. *J Mater Chem A* **2014,** *2* (48), 20605-20611.

39. Geng, D. S.; Chen, Y.; Chen, Y. G.; Li, Y. L.; Li, R. Y.; Sun, X. L.; Ye, S. Y.; Knights, S., High oxygen-reduction activity and durability of nitrogen-doped graphene. *Energ Environ Sci* **2011,** *4* (3), 760-764.

40. Sheng, Z. H.; Shao, L.; Chen, J. J.; Bao, W. J.; Wang, F. B.; Xia, X. H., Catalyst-Free Synthesis of Nitrogen-Doped Graphene via Thermal Annealing Graphite Oxide with Melamine and Its Excellent Electrocatalysis. *Acs Nano* **2011,** *5* (6), 4350-4358.

41. Dan, Y.; Lu, Y.; Kybert, N. J.; Luo, Z.; Johnson, A. T. C., Intrinsic Response of Graphene Vapor Sensors. *Nano Lett* **2009,** *9* (4), 1472-1475.

42. Miller, L. L.; Bankers, J. S.; Schmidt, A. J.; Boyd, D. C., Organic vapors, organic polymers and electrical conductivity. *Journal of Physical Organic Chemistry* **2000,** *13* (12), 808-815.

43. Smirnov, V. A.; Denisov, N. N.; Ukshe, A. E.; Shulga, Y. M., Conductivity of graphene oxide films: Dependence from solvents and photoreduction. *Chem Phys Lett* **2013,** *583* (0), 155-159.

44. Ahmed, M. S.; Han, H. S.; Jeon, S., One-step chemical reduction of graphene oxide with oligothiophene for improved electrocatalytic oxygen reduction reactions. *Carbon* **2013,** *61* (0), 164-172.

45. Zhang, L.; Yu, J.; Yang, M.; Xie, Q.; Peng, H.; Liu, Z., Janus graphene from asymmetric two-dimensional chemistry. *Nat Commun* **2013,** *4*, 1443.

46. Bekyarova, E.; Itkis, M. E.; Ramesh, P.; Berger, C.; Sprinkle, M.; de Heer, W. A.; Haddon, R. C., Chemical Modification of Epitaxial Graphene: Spontaneous Grafting of Aryl Groups. *J Am Chem Soc* **2009,** *131* (4), 1336-1337.

47. Lomeda, J. R.; Doyle, C. D.; Kosynkin, D. V.; Hwang, W.-F.; Tour, J. M., Diazonium Functionalization of Surfactant-Wrapped Chemically Converted Graphene Sheets. *J Am Chem Soc* **2008,** *130* (48), 16201-16206.

Chapter 4

Donor-Acceptor Intraparticle Transfer of Metal-Ligand Systems

4.1 Introduction of Molecular Dyads and Metal Nanoparticles

Looking at smaller systems probing electron transfer can be accomplished by moving from CQDs and GQDs to metallic nanoparticles which have donor and acceptor moieties covalently attached. Systems with both donor and accepter functionality are known as molecular dyads. Conventional molecular dyads refer to a class of functional molecular complexes that consist of an electron-donating moiety and an electron–accepting counterpart linked by a chemical bridge. Upon photoirradiation, effective intramolecular electron and/or energy transfer may occur, leading to the emergence of unprecedented optical and electronic properties that may be exploited for diverse applications in, for instance, molecular electronics, electroluminescence, and organic photovoltaics.[1-3] Of these, anthracene derivatives have been used rather extensively as effective electron acceptors with apparent emission in the blue region, whereas common electron acceptors include derivatives of triphenylamine, carbazole, and phenothiazine that are known to facilitate hole transport (high hole mobilities) because of the electron-rich nitrogen. In fact, a series of studies have been reported in the literature that involve such a donor-acceptor molecular architecture. For instance, Mori et al.[4] prepared copolymers with anthracene units embedded in the polymeric backbone along with side chains of triphenylamine, carbazole, or phenothiazine moieties. The resulting materials exhibited characteristic fluorescence energy transfer, as confirmed by UV-vis and fluorescence measurements. Tao and coworkers[5] and Lee *et al*.[6] synthesized a series of molecular dyads based on anthracene-triphenylamine derivatives and used these

materials to make highly efficient blue organic light-emitting diodes. In other studies,[7-8] it was found that molecular dyads with anthracene derivatives and triarylamine hole stabilizers linked by π-conjugated bithiophene bridges exhibited superior intramolecular charge transfer from triarylamine to anthracene, which might be exploited for the preparation of small-molecule organic solar cells. Intramolecular electron and energy transfer was also observed with triphenylamine–bound zinc porphyrins.[9] For instance, Ezoe *et al*.[10] prepared a diarylurea-linked zinc porphyrin–anthracene dyad and observed intromolecular excitation energy transfer from anthracene to the zinc chromophore.

In these earlier studies, the efficiency of intramolecular energy/electron transfer and hence the optical/electronic properties of the molecular dyads are sensitively dependent upon the nature of the chemical bridges that link the donor and acceptor moieties. Whereas conventionally such chemical linkers are aliphatic fragments that covalently bond to the donor and acceptor termini, nonbonding interactions have also been used as a tool to arrange donor-acceptor dyads, such as H-bonding, salt bridges, and hydrophobic interactions.[11-15] For instance, Kercher et al.[16] used a coordination compound, a scandium(III) acetylacetonate derivative, as the core and promoter of the dyad formation by noncovalent assembly of both an energy-donating ruthenium(II) bipyridine complex and an energy-accepting anthracene derivative, and observed effective quenching of the fluorescence of the ruthenium chromophore by a fast intercomponent triplet-triplet energy-transfer process.

With this arises an immediate question. That is, is it possible to use metal nanoparticles as a unique structural scaffold to create functional dyads (or even multiads)? There are at least two advantages. Similar to the above study where an organometallic complex is used as the core to form a dyad structure,[16] such a nanoscale architecture will significantly reduce the synthetic effort. Furthermore, it has long been known that nanoparticles can be chemically decorated with multiple functional groups,[17-18] which renders it possible to incorporate diverse and multiple functional moieties onto the nanoparticle surface, leading to the ready formation of a wide range of dyad (multiad) structures. More significantly, recently it has been found that organic functional ligands may be bound onto the metal core surface by different interfacial bonding interactions. Such unique chemistry may be exploited for further manipulation of the electronic interactions between the particle-bound functional moieties and hence the nanoparticle optical and electronic properties. For instance, when functional groups are bound onto the nanoparticle surface by π conjugated metal-ligand bonds, effective intraparticle charge delocalization occurs between the particle-bound functional moieties,[19-22] which may be further manipulated by the core valence states or external electrostatic polarization.[23-25] This is in sharp contrast with mercapto-functionalized nanoparticles where the metal-sulfur bonds lack interesting chemistry.

It is within this context that this work was designed and carried out. In the present study, both derivatives of triphenylamine and anthracene were covalently bound onto ruthenium nanoparticle surface by conjugated metal-ligand bonds by

olefin metathesis reactions of 1-decyne-functionalized ruthenium nanoparticles with 4-ethynyl-*N*,*N*-diphenylaniline and vinylanthracene. Spectroscopic as well as photoelectrochemical measurements indicated that upon photoirradiation, effective intraparticle charge transfer occurred from the triphenylamine group to the anthracene moiety, a behavior consistent with those of conventional molecular dyads.

4.2 Experimental

4.2.1. Chemicals Synthesis & Resistivity Sensing of Ruthenium Nanoparticles

Ruthenium chloride hydrate ($RuCl_3 \cdot xH_2O$, ACROS), sodium acetate (NaOAc, 99.0 %, MC&B), 9-vinylanthracene (VAN, 97%, Sigma-Aldrich), 1-decyne (95.0%, TCI America), 1,2-propanediol (99.5%, Sigma-Aldrich), triphenylamine (TPA, 98%, Sigma-Aldrich), and other solvents were obtained from typical commercial sources and used without further treatment. Water was supplied by a Barnstead Nanopure water system (18.3 MΩ·cm). The synthesis and characterization of 4-ethynyl-*N*,*N*-diphenylaniline (EDPA) has been described previously in detail.[26]

4.2.2. Synthesis & Functionalization of Ruthenium Nanoparticles

The synthetic procedure of ruthenium nanoparticles has been detailed previously.[21] In brief, a round bottom flask with 170 mL of 1,2-propainediol was set in a heating mantle with a slow bubble of nitrogen. A measure of $RuCl_3$ 0.05 g is dissolved in a small amount of ethanol then added to the flask, along with a six molar equivalent of sodium acetate. The solution was subject to thermal refluxing for 2 h, and the appearance of a dark brown color signified the formation of “bare” ruthenium colloids. The solution was then cooled down to room temperature, and a calculated

amount of 1-decyne (typically at three-fold molar excess of $RuCl_3$) dispersed in 20 mL of toluene was added into the solution. The solution was then mixed by magnetic stirring overnight, resulting in the extraction of the nanoparticles into the toluene phase, as manifested by the dark brown color in the toluene phase and the colorless appearance of the propanediol phase. This was due to the self-assembly of 1-decyne onto the ruthenium colloid surface forming ruthenium-vinylidene conjugated bonds at the metal-ligand interface. The toluene phase was then collected and the solvents were removed by rotary evaporation. The resulting solids were then rinsed extensively with methanol to remove excessive free ligands, affording 1-decyne-passivated ruthenium nanoparticles, which were denoted as RuHC10. The average core size of RuHC10 nanoparticles was 2.12 ± 0.72 nm, as determined by transmission electron microscopic measurements.[21]

Surface functionalization of the RuHC10 nanoparticles was then carried out by metathesis reactions of the nanoparticles with olefin or acetylene derivatives (Scheme 1).[21] In a typical experiment, 20 mg of RuHC10 nanoparticles was dispersed in 0.3 mL of dichloromethane with a calculated amount of EDPA, VAN or a binary mixture of EDPA and VAN (at a molar ratio of 1:1) under magnetic stirring for 2 d. The resulting nanoparticles after purification were denoted as Ru(EDPA), Ru(VAN), and Ru(EDPA/VAN), respectively.

Spectroscopic characterizations by ^{1}H-NMR measurements were performed with a Varian Unity 500 MHz NMR spectrometer using concentrated solutions of the nanoparticles in CD_2Cl_2. The absence of any sharp spectral features indicated that the

nanoparticles were free of excessive ligands. To quantify the surface concentration of the functional ligands, the nanoparticle cores were dissolved in a dilute aqueous KCN solution and the organic components were extracted by CH_2Cl_2 for ^1H NMR measurements. Based on the ratios of the integrated peak areas of the aromatic protons and the methyl protons, the surface coverage of the TPA moieties of the Ru(EDPA) nanoparticles was estimated to be 40.1%; in Ru(VAN), the concentration of the anthracene moieties was 9.9%; and in Ru(EDPA/TPA), the concentrations of the TPA and anthracene moieties were 25.2% and 35.8%, respectively (Figure 4.6). UV-Vis spectra were acquired with an ATI Unicam UV4 spectrometer at 2 nm resolution by using a 1 cm quartz cuvette. Photoluminescence measurements were carried out using a PTI fluorospectrometer with the same solutions as those for UV-vis studies. FTIR spectra were obtained with Perkin-Elmer Spectrum One Spectrometer at a resolution of 1 cm^{-1}, where the samples were prepared by dropcasting a concentrated solution of the nanoparticles onto a ZnSe disk.

4.2.3 Electrochemical Procedure for Probing Intraparticle Electron Transfer

Electrochemical studies were carried out with a CHI 710 Electrochemical Workstation using a 3 mL quartz cuvette as the electrochemical cell. A gold disk sealed in glass tubing was used as the working electrode which was bended at the end so that the gold disk was facing sideways (for photoirradiation). The electrode was first polished by 0.03 μm alumina slurries and then sonicated in Nanopure water. The gold electrode was further treated by rapid potential cycling in H_2SO_4 within the potential range of –0.2 V to +1.2 V at a potential sweep rate of 10 V/s, until a well-

defined voltammetric feature for a clean gold surface was obtained, from which the effective electrochemical surface area was determined (ca. 1.3 mm^2). A Ag/AgCl wire and a platinum coil were used as the reference and counter electrode, respectively. The electrolyte solution was deaerated with nitrogen for 5 min and then blanketed with an atmosphere of nitrogen during the entire experimental procedure. The voltammograms were acquired both in the dark and under UV photoirradiation (365 nm, 6 W).

4.3 Results & Discussion of Electrochemical Studies

Previously it has been found that acetylene derivatives may self-assemble on metal nanoparticle surfaces forming metal-vinylidene interfacial linkages by a tautomeric rearrangement process, and the resulting nanoparticles can undergo metathesis reactions with other acetylene or vinyl derivatives for further surface functionalization, with the functional units bound onto the nanoparticle surface by conjugated metal-carbon π bonds (Scheme 1).[27] As mentioned earlier, the successful incorporation of the triphenylamine and anthracene moieties onto the ruthenium nanoparticle surface was firstly confirmed by ^{1}H NMR measurements (Figure 4.6). The structures of the organic capping ligands were further examined by FTIR spectroscopic measurements. Figure 4.1 depicts the FTIR spectra of the Ru(EDPA), Ru(VAN), and Ru(EDPA/VAN) nanoparticles, along with those of the monomeric EDPA and VAN. There are several features that warrant special attention here. First, for the three nanoparticle samples (solid curves), three spectral features can be identified between 2100 cm^{-1} and 1900 cm^{-1} at 2056 cm^{-1}, 1976 cm^{-1} and 1950 cm^{-1},

which may be accounted for by the self-assembly of the terminal acetylene moieties onto the Ru particle surface forming ruthenium-vinylidene (Ru=C=CH–, Scheme 1) interfacial linkages. For comparison, the C≡C vibration of EDPA monomers (dashed black curve) can be found at 2104 cm^{-1} (and for 1-alkynes, this typically appears at ca. 2119 cm^{-1}). The apparent red-shift of the vibrational features of the nanoparticle-bound C≡C moieties as compared to those of monomers of acetylene derivatives was ascribed to the intraparticle charge delocalization as a result of the conjugated metal-ligand interfacial bonding interactions, as observed previously.[21]

Scheme 4.1 Schematic of ruthenium nanoparticles functionalized with (i) EDPA, (ii) VAN or (iii) both.

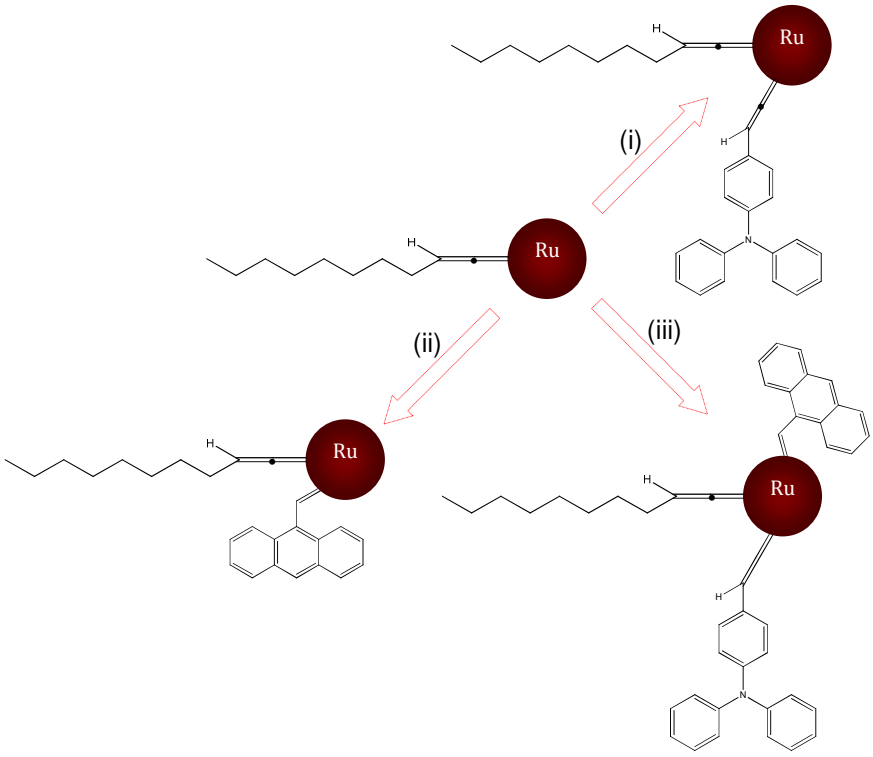

Second, in contrast to the spectral profiles of monomeric EDPA and VAN ligands (dashed curves), a new vibrational band can be rather clearly seen at 804 cm^{-1} for the three nanoparticles (solid curves). This may be ascribed to the bending vibration of the vinylidene =C–H moiety (Scheme 1), in good agreement with results of trisubstituted alkenes.[28] In fact, such a spectral feature has also been observed previously with ruthenium nanoparticles functionalized with 1-alkynes (though it was not explicitly identified at that time),[27] whereas for ruthenium nanoparticles functionalized with acetylide derivatives (i.e., deprotonated alkynes),[20] no such feature was observed as no vinylidene moieties were formed at the metal-ligand interface.

Third, the nanoparticles exhibited no features around 3300 cm–1, indicating that the samples were free of excessive monomeric ligands (note that EDPA monomers display a band at 3288 cm–1 which is due to the terminal ≡C–H vibration).[27] In addition, the aromatic C=C vibrational stretches can be identified between 1400 cm–1 and 1600 cm–1 for both the nanoparticles and monomeric ligands, again, consistent with the incorporation of EDPA and VAN ligands onto the nanoparticle surface.

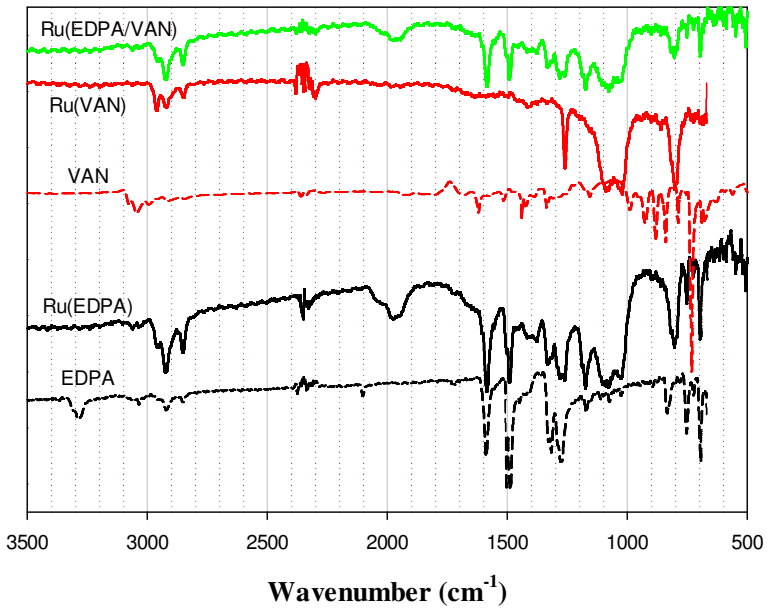

Figure 4.1: FTIR spectra of Ru(EDPA), Ru(VAN) and Ru(EDPA/VAN) nanoparticles (solid curves), along with those of the monomeric EDPA and VAN ligands (dashed curves).

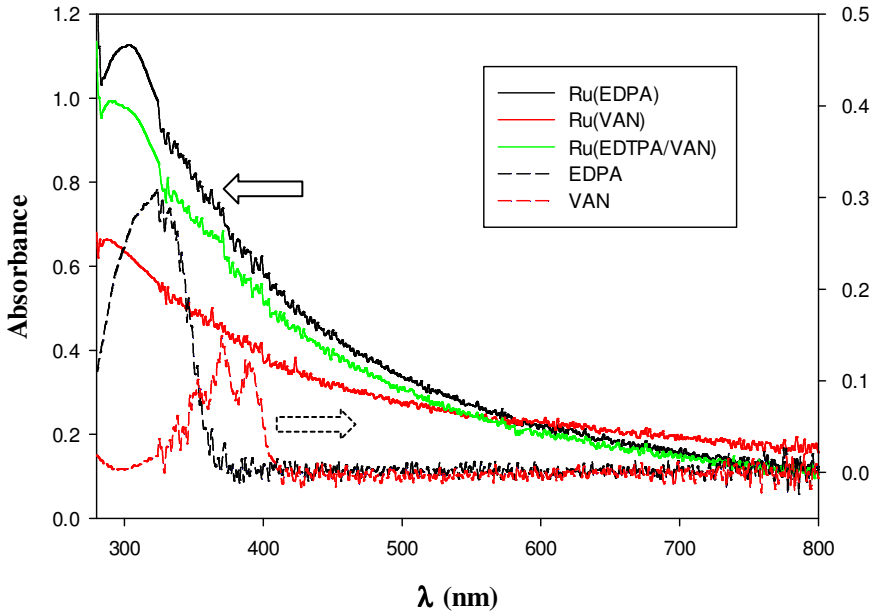

Figure 4.2: UV-Vis absorption spectra of Ru(EDPA), Ru(VAN), and Ru(EDPA/VAN) nanoparticles (solid curves), as well as monomeric EDPA and VAN (dashed curves) in CH_2Cl_2. The left y-axis is for the nanoparticles whereas the right y-axis is for the monomeric ligands.

The optical properties of the chemically-functionalized nanoparticles were then investigated by UV-vis and fluorescence spectroscopic measurements. Figure 4.2 depicts the UV-vis absorption spectra of the Ru(EDPA), Ru(VAN) and Ru(EDPA/VAN) nanoparticles as well as the monomeric EDPA and VAN ligands. First, it can be seen that the three nanoparticle samples all exhibited an exponential-decay profile, due to the so-called Mie scattering as anticipated for nanosized metal nanoparticles.[29] Second, EDPA monomers (black dashed curve) exhibit a broad absorption band at ca. 322 nm, which may be ascribed to the n-π^* transition involving the central N atom.[5,30] In the Ru(EDPA) nanoparticles (solid black curve), this band blue-shifted somewhat to 302 nm. For monomeric VAN (dashed red curve), several absorption features can be identified between 350 nm and 400 nm which can be ascribed to the π-π* vibronic transitions of the molecules; and such characteristics can also be vaguely observed with the Ru(VAN) nanoparticles (solid red curve).[31] For the Ru(EDPA/VAN) nanoparticles (solid green curve), one can see that the absorption features of both the triphenylamine and anthracene cores can be identified in the regions of 300 – 330 nm and 330 – 400 nm, respectively. Again, this is consistent with the successful incorporation of both functional moieties onto the nanoparticle surface.

As both functional moieties were bound onto the ruthenium nanoparticle surface by Ru=C π bonds, effective intraparticle charge transfer occurred from the electron-donating triphenylamine core to the electron-accepting anthracene moiety upon photoirradiation, as revealed in photoluminescence measurements. From Figure

4.3, it can be seen that for the monofunctionalized nanoparticles of Ru(EDPA) and Ru(VAN), the photoluminescence profiles were characteristic of the respective functional moiety, though with some discrepancy. For instance, monomeric EDPA ligands showed a well-defined excitation peak (λ_{ex}) at 330 nm and an prominent emission one (λ_{em}) at 400 nm (dashed black curves), whereas for the Ru(EDPA) nanoparticles, the excitation peak position was found to red-shift somewhat to 340 nm, and the corresponding emission spectrum exhibited two major peaks at 384 nm and 414 nm, along with a shoulder at 442 nm (solid black curves), as summarized in Table 4.1. In contrast, for monomeric VAN (dashed red curves), two excitation peaks can be found at 371 and 385 nm and two emission peaks at 409 and 427 nm; yet for the Ru(VAN) nanoparticles (solid red curves), the excitation peak position blue-shifted rather markedly to 347 nm and the emission profiles entailed a broad band centered at around 460 nm (Table 4.1). This is completely different from that observed in a previous study with carbene-stabilized ruthenium nanoparticles that were partially functionalized with vinylanthracene,[31] where a small red-shift was actually observed of the excitation peak position for the particle-bound anthracene moieties along with a decreasing Stokes shift between the emission and excitation peaks, as compared to those of the monomeric ligands. While the details are not clear at this point, this discrepancy may be ascribed to the interactions between the π electrons of the anthracene and vinylidene/carbene moieties and hence different chemical environments for the anthracene units.

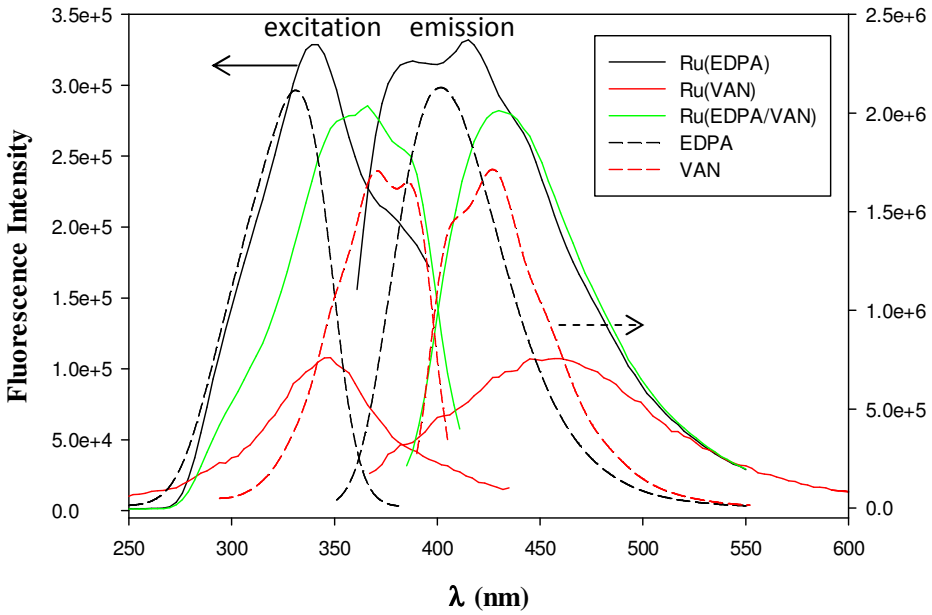

Figure 4.3: Excitation and emission spectra of Ru(EDPA), Ru(VAN), and Ru(EDPA/VAN) nanoparticles (solid curves), as well as monomeric EDPA and VAN (dashed curves) in CH_2Cl_2. The left y-axis is for the nanoparticles whereas the right y-axis is for the monomeric ligands. The solutions were the same as those in Figure 4.2.

For the nanoparticles co-functionalized with both EDPA and VAN (green curves), the photoluminescence properties are more complicated, as depicted by the green curves. The most prominent excitation and emission peaks can be found at 365 nm and 431 nm (Table 4.1). Both the excitation and emission profiles resemble neither those of Ru(EDPA) nor those of Ru(VAN) in panel (A), suggesting a rather efficient mixing of the electronic energy levels of the particle-bound triphenylamine and anthracene moieties and hence the formation of new energy structures, most probably as a result of the conjugated metal-ligand interfacial bonds. In fact, one can see that the excitation peak position was intermediate in position and energy between those of Ru(EDPA) and Ru(VAN), whereas the emission peak position was lower than etherthose of Ru(EDPA) or Ru(VAN). These observations suggest that the

Ru(EDPA/VAN) nanoparticles behaved analogously to molecular dyads based on the triphenylamine-anthracene pairs with a conjugated chemical linker and effective transfer of charge rather than energy occurred between the particle-bound triphenylamine and anthracene moieties.

For comparison, in a recent study Tang and coworkers[32] designed and synthesized star-shaped tris(4-anthracene-phenyl)amine, a compound with a triphenylamine core decorated with three peripheral anthracene units, and observed a single prominent fluorescence emission peak at 464 nm in chloroform, along with three absorption peaks at 350nm, 368 nm, and 388 nm in UV-vis absorption measurements, which were attributed to the anthracene units (another peak at 310 nm was assigned to the absorption of the triphenylaimine unit). These results suggested little electronic coupling between the triphenylamine and anthracene moieties because of a large dihedral angle between them. In contrast, for tris(4-phenanthrene-phenyl)amine where the triphenylamine core was now decorated with phenanthrene, because the twist angle between the phenanthrene plane and the phenyl ring was small, extensive conjugation occurred between the triphenylamine moiety and the substituted phenanthrene, leading to the appearance of only one absorption peak at 345 nm, along with a photoluminescence emission peak at 425 nm, which was attributed to the π-π^* transition of the entire molecule.

Table 4.1. Summary of excitation and emission peak positions of Ru(EDPA), Ru(VAN), and Ru(EDPA/VAN) nanoparticles and the corresponding monomeric ligands

	EDPA	**VAN**	**Ru(EDPA)**	**Ru(VAN)**	**Ru(EDPA/VAN)**
λ_{ex} (nm)	**330**	**371, 385**	**340**	**347**	**365**
λ_{em} (nm)	**400**	**409, 427**	**384, 414**	**460**	**431**

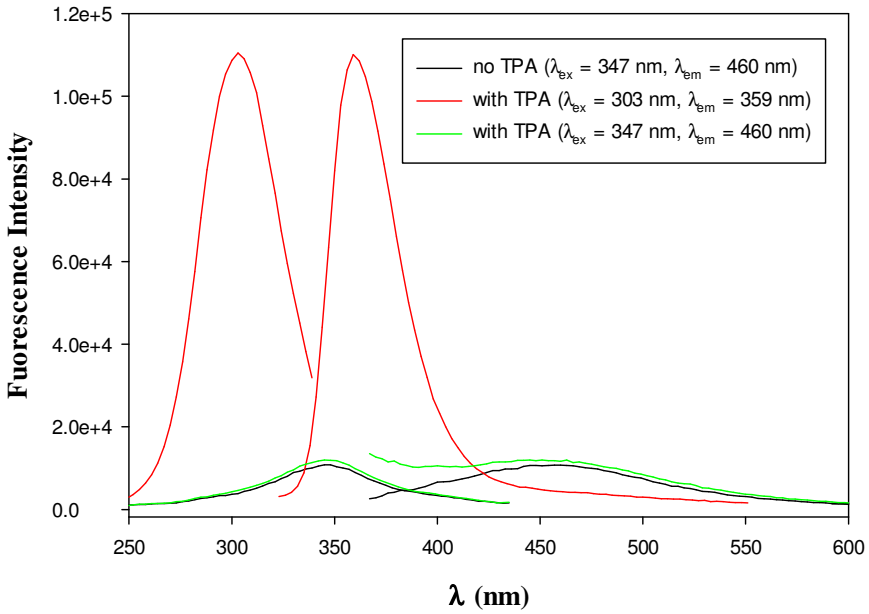

Figure 4.4: Excitation and emission spectra of Ru(VAN) nanoparticles in the absence (black curves) and presence (red and green curves) of monomeric triphenylamine ligands in CH_2Cl_2. The concentration of the nanoparticle was 0.1 mg/mL and that of triphenylamine was 1 nM.

Such intraparticle charge delocalization is likely facilitated by through-bond interactions.[19] In fact, this hypothesis was further supported by a control experiment where monomeric triphenylamine was added to a solution of Ru(VAN) nanoparticles and there were virtually no interactions between the triphenylamine and anthracene moieties. Figure 4.3 depicts the excitation and emission spectra of Ru(VAN) nanoparticles in the absence and presence of 1 nM monomeric triphenylamine. It can be seen that at λ_{ex} = 347 nm, the emission profiles of the Ru(VAN) nanoparticles remained virtually unchanged regardless of the addition of triphenylamine monomers; and when collected at λ_{em} = 360 nm, the excitation curves remained the same as well (black and green curves). In addition, when excited at λ_{ex} = 303 nm, the mixed solution of Ru(VAN) and triphenylamine exhibited an emission spectrum that is

consistent with that of triphenylamine monomers showing a single peak at λ_{em} = 359 nm. These observations indicate that in the mixed solution of Ru(VAN) and triphenylamine, the two functional moieties were rather independent of each other with minimal energy transfer and through-space charge transfer did not occur.

Note that in previous studies,[21,27] we demonstrated that the particle-bound acetylene moieties behaved analogously to diacetylene derivatives and exhibited apparent photoluminescence as a result of intraparticle charge delocalization. However, such emissions were not resolved here as those from the triphenylamine and anthracene moieties were markedly more intense.

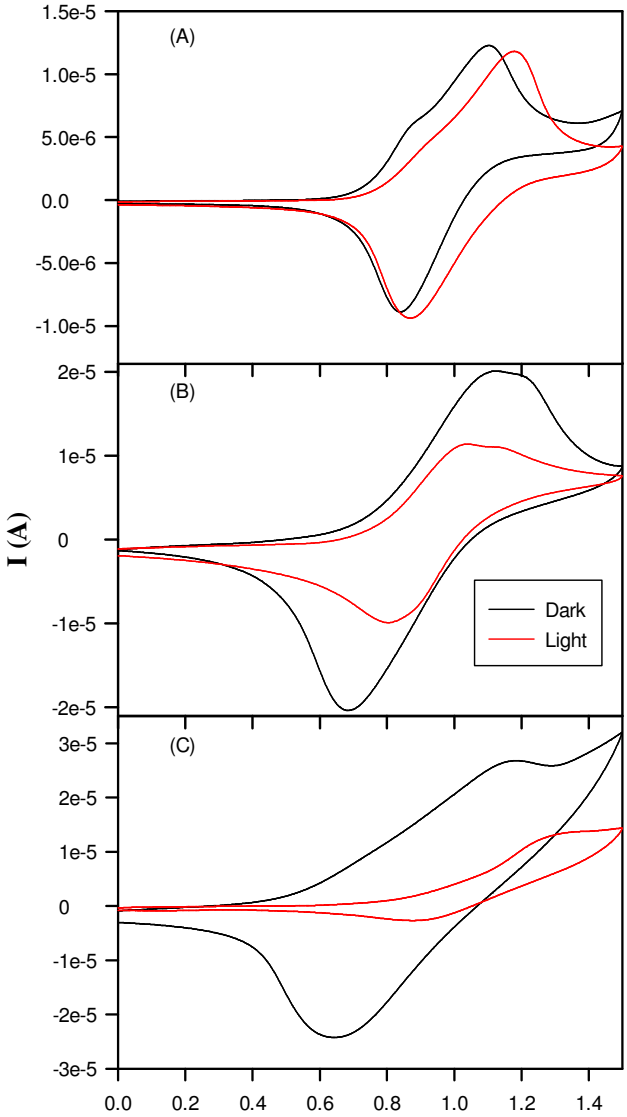

Figure 4.5: Cyclic voltammograms acquired in the dark (black curves) and under photoirradiation (red curves) of (A) monomeric EDTA, (B) Ru(EDPA), and (C) Ru(EDPA/VAN) nanoparticles in CH_2Cl_2 with 0.1 M TBAP. The concentration of monomeric EDPA in (A) is ca. 2.2 mM, and the nanoparticle concentrations in (B) and (C) are both about 0.7 mg/mL. The area of the gold electrode was 1.3 mm^2, and potential sweep rate 50 mV/s.

Electrochemical measurements further demonstrated that effective photo-induced charge transfer occurred in Ru(EDPA/VAN) nanoparticles. Figure 4.5 shows the cyclic voltammograms of a gold disk electrode in a deaerated solution of (A)

monomeric EDPA, (B) Ru(EDPA) and (C) Ru(EDPA/VAN) in CH_2Cl_2 with 0.1 M TBAP in the dark (black curves) and upon the exposure to UV light irradiation (366 nm, red curves) — note that the triphenylamine moiety emits photoluminescence strongly under photoexcitation at this wavelength (Figure 4.4). In panel (A), one can see that (i) a pair of voltammetric peaks appeared within the potential range of +0.70 and 1.50 V, (ii) the formal potential can be identified at +0.97 V in the dark and +1.02 V under UV photoirradiation, and (iii) the voltammetric peak currents remained virtually unchanged in the dark and under photoirradiation. These voltammetric features may be ascribed to the redox reaction of the triphenylamine moieties involving the formation of a cationic radical, $EDPA^{+\bullet} + e^- \leftrightarrow EDPA$.[30,32] The fact that the voltammetric profiles remained practically unchanged before and after photoirradiation indicated that the EDPA molecules were photochemically stable and the lifetime of the photoexcited state was significantly shorter than the voltammetric time scale.

In panel (B), Ru(EDPA) nanoparticles exhibited somewhat different voltammetric characteristics. Again, a pair of voltammetric peaks cane seen both in the dark and under UV photoirradiation, with the formal potentials very close to each other, at 0.90 and 0.92 V, respectively. Yet, the voltammetric currents diminished by about 50% under UV photoirradiation as compared to those acquired in the dark. Such a behavior is drastically different from that of monomeric EDPA in panel (A). This may be attributed to the conjugated metal-ligand interfacial bonding interactions that facilitate charge transfer of the particle-bound functional moieties to the

nanoparticle cores. That is, under UV photoirradiation, the photoexcited electrons might be effectively transferred to the metal cores, as it has been found previously that the metal core electrons serve as the effective conducting medium for intraparticle charge delocalization between particle-bound functional groups.[19]

With the attachment of electron-accepting anthracene moieties onto the nanoparticle surface also by conjugated metal-ligand interfacial bonds, the photoelectrochemical behaviors of the particle-bound triphenylamine moieties became more interesting. In panel (C), one can see that in the dark, again, a pair of voltammetric peaks can be identified with the formal potential of +0.91 V. However, under UV photoirradiation, the voltammetric peaks almost disappeared completely. This may be accounted for by the presence of electron-accepting anthracene moieties on the nanoparticle surface that further facilitate charge transfer from the photoexcited triphenylamine moieties to the nanoparticle cores and then to the anthracene centers. The photo-induced depletion of the triphenylamine valence electrons thus led to the diminishment of the corresponding voltammetric features. These results are consistent with the photoluminescence observations presented above, suggesting that with the nanoparticle core serving as the conducting medium, the particle-bound triphenylamine and anthracene moieties indeed behaved analogously to molecular dyads based on these two functional units bridged by conjugated chemical spacers.

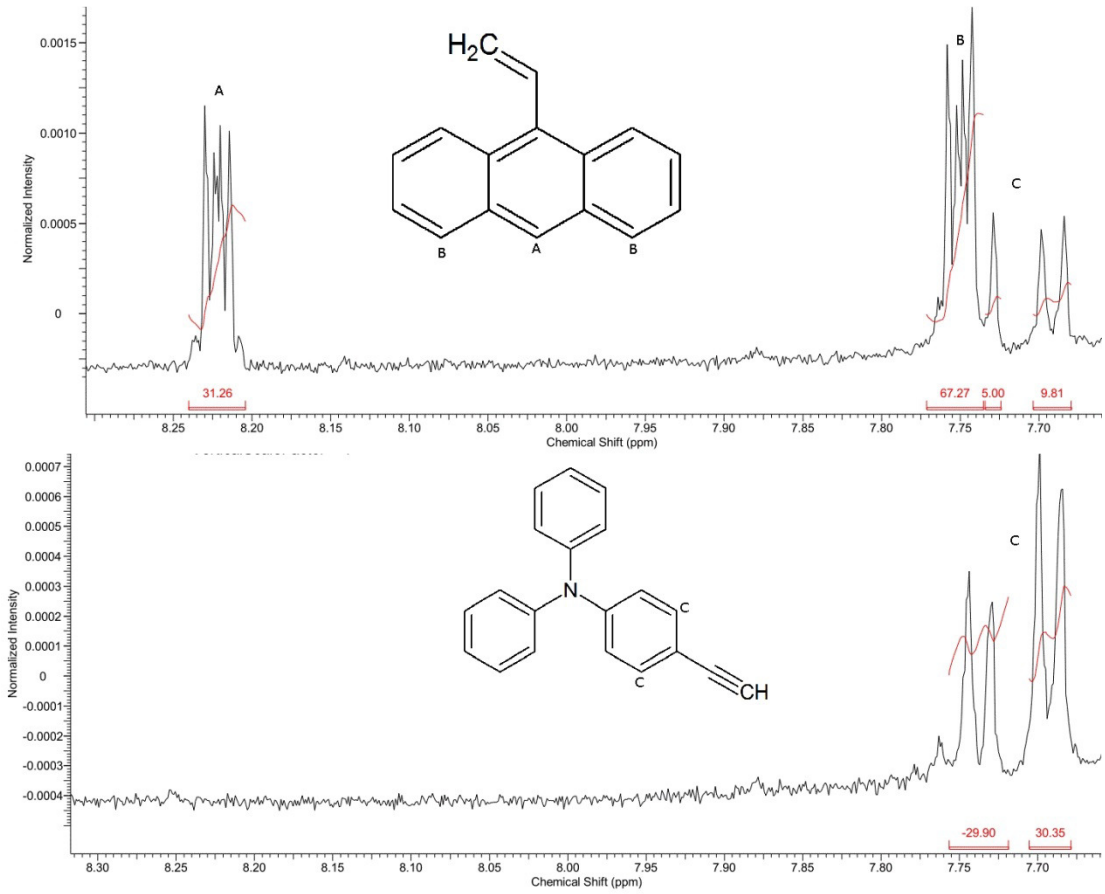

Figure 4.6: Calculation of ligand coverage and ratios done by NMR spectra of Ru(EDTA) and Ru(EDTA & VAN) nanoparticle ligands. Peak A in the top plot corresponds to one proton which can be used to deconvolute peak B from peak C which allows for integrations of the aromatic region to be attributed to each of the ligand species specifically and compared to the aliphatic region

4.4 Conclusions on Intraparticle Transfer

When functional moieties are bound onto metal nanoparticle surfaces by conjugated metal-ligand interfacial bonding interactions, effective intraparticle charge delocalization occurs. For nanoparticles co-functionalized with derivatives of triphenylamine and anthracene, the resulting nanoparticles exhibited spectroscopic and electrochemical characteristics that are consistent with conventional molecular dyads based on the same electron-donating and –accepting units. Significantly, it was found that photoluminescence emission of the Ru(EDPA/VAN) nanoparticles was completely different from those of the monofunctionalized Ru(EDPA) and Ru(VAN) nanoparticles, suggesting effective mixing of the π electrons between the triphenylamine and anthracene moieties. Furthermore, in photoelectrochemical studies, the particle-bound triphenylamine moieties exhibited a pair of well-defined voltammetric peaks in the dark due to the redox reactions involving the formation of cationic radicals; yet upon exposure to UV photoirradiation, the peak currents diminished drastically, which was ascribed to the rapid transfer of photogenerated electrons from the triphenylamine units to the anthracene ones. This is most likely facilitated by the conjugated metal-ligand bonds and hence low interfacial contact resistance. Such a unique property should be of vital importance in the development of small-molecule organic solar cells or light-emitting diodes.[5-8]

4.5 References

1. Raymo, F. M.; Tomasulo, M., Electron and energy transfer modulation with photochromic switches. *Chem Soc Rev* **2005,** *34* (4), 327-336.

2. Verhoeven, J. W., On the role of spin correlation in the formation, decay, and detection of long-lived, intramolecular charge-transfer states. *J Photoch Photobio C* **2006,** *7* (1), 40-60.

3. Lin, Y. Z.; Li, Y. F.; Zhan, X. W., Small molecule semiconductors for high-efficiency organic photovoltaics. *Chem Soc Rev* **2012,** *41* (11), 4245-4272.

4. Mori, H.; Tando, I.; Tanaka, H., Synthesis and Optoelectronic Properties of Alternating Copolymers Containing Anthracene Unit in The Main Chain by Radical Ring-Opening Polymerization. *Macromolecules* **2010,** *43* (17), 7011-7020.

5. Tao, S.; Zhou, Y. C.; Lee, C. S.; Lee, S. T.; Huang, D.; Zhang, X. H., Highly efficient nondoped blue organic light-emitting diodes based on anthracene-triphenylamine derivatives. *J Phys Chem C* **2008,** *112* (37), 14603-14606.

6. Lee, K. H.; You, J. N.; Kwon, H. J.; Kim, Y. K.; Yoon, S. S., Synthesis and Electroluminescent Properties of Blue Fluorescent Triphenylamine Substituted Anthracene Derivatives for OLEDs. *Mol Cryst Liq Cryst* **2010,** *530*, 204-211.

7. Choi, H.; Ko, H. M.; Cho, N.; Song, K.; Lee, J. K.; Ko, J., Electron-Rich Anthracene Semiconductors Containing Triarylamine for Solution-Processed Small-Molecule Organic Solar Cells. *Chemsuschem* **2012,** *5* (10), 2045-2052.

8. Thomas, K. R. J.; Singh, P.; Baheti, A.; Hsu, Y. C.; Ho, K. C.; Lin, J. T., Electro-optical properties of new anthracene based organic dyes for dye-sensitized solar cells. *Dyes Pigments* **2011,** *91* (1), 33-43.

9. Huang, C. W.; Chiu, K. Y.; Cheng, S. H., Novel spectral and electrochemical characteristics of triphenylamine-bound zinc porphyrins and their intramolecular energy and electron transfer. *Dalton T* **2005,** (14), 2417-2422.

10. Ezoe, M.; Minami, T.; Ogawa, Y.; Yagi, S.; Nakazumi, H.; Matsuyama, T.; Wada, K.; Horinaka, H., Intramolecular excitation energy transfer in diarylurea-linked zinc porphyrin-anthracene dyads. *Photoch Photobio Sci* **2005,** *4* (8), 641-646.

11. Ghaddar, T. H.; Castner, E. W.; Isied, S. S., Molecular recognition and electron transfer across a hydrogen bonding interface. *J Am Chem Soc* **2000,** *122* (6), 1233-1234.

12. Ward, M. D.; Barigelletti, F., Control of photoinduced energy transfer between metal-polypyridyl luminophores across rigid covalent, flexible covalent, or hydrogen-bonded bridges. *Coordin Chem Rev* **2001,** *216*, 127-154.

13. Nelissen, H. F. M.; Schut, A. F. J.; Venema, F.; Feiters, M. C.; Nolte, R. J. M., Switch-on luminescence detection of steroids by tris(bipyridyl)ruthenium(II) complexes containing multiple cyclodextrin binding sites. *Chem Commun* **2000,** (7), 577-578.

14. Kaifer, A. E., Interplay between molecular recognition and redox chemistry. *Accounts Chem Res* **1999,** *32* (1), 62-71.

15. Billing, R.; Rehorek, D.; Hennig, H., Photoinduced Electron-Transfer in Ion-Pairs. *Topics in Current Chemistry* **1990,** *158*, 151-199.

16. Kercher, M.; Konig, B.; Zieg, H.; De Cola, L., Photoinduced energy- and electron-transfer processes within dynamic self-assembled donor-acceptor arrays. *J Am Chem Soc* **2002,** *124* (38), 11541-11551.

17. Templeton, A. C.; Wuelfing, M. P.; Murray, R. W., Monolayer protected cluster molecules. *Accounts Chem Res* **2000,** *33* (1), 27-36.

18. Rotello, V. M., *Nanoparticles : building blocks for nanotechnology*. Kluwer Academic/Plenum Publishers: New York, 2004; p x, 284 p.

19. Chen, W.; Chen, S. W.; Ding, F. Z.; Wang, H. B.; Brown, L. E.; Konopelski, J. P., Nanoparticle-mediated intervalence transfer. *J Am Chem Soc* **2008,** *130* (36), 12156-12162.

20. Chen, W.; Zuckerman, N. B.; Kang, X. W.; Ghosh, D.; Konopelski, J. P.; Chen, S. W., Alkyne-Protected Ruthenium Nanoparticles. *J Phys Chem C* **2010,** *114* (42), 18146-18152.

21. Kang, X. W.; Zuckerman, N. B.; Konopelski, J. P.; Chen, S. W., Alkyne-Functionalized Ruthenium Nanoparticles: Ruthenium-Vinylidene Bonds at the Metal-Ligand Interface. *J Am Chem Soc* **2012,** *134* (3), 1412-1415.

22. Kang, X. W.; Song, Y.; Chen, S. W., Nitrene-functionalized ruthenium nanoparticles. *J Mater Chem* **2012,** *22* (36), 19250-19257.

23. Kang, X. W.; Zuckerman, N. B.; Konopelski, J. P.; Chen, S. W., Alkyne-Stabilized Ruthenium Nanoparticles: Manipulation of Intraparticle Charge Delocalization by Nanoparticle Charge States. *Angew Chem Int Edit* **2010,** *49* (49), 9496-9499.

24. Kang, X. W.; Chen, W.; Zuckerman, N. B.; Konopelski, J. P.; Chen, S. W., Intraparticle Charge Delocalization of Carbene-Functionalized Ruthenium Nanoparticles Manipulated by Selective Ion Binding. *Langmuir* **2011,** *27* (20), 12636-12641.

25. Kang, X. W.; Li, X.; Hewitt, W. M.; Zuckerman, N. B.; Konopelski, J. P.; Chen, S. W., Manipulation of Intraparticle Charge Delocalization by Selective Complexation of Transition-Metal Ions with Histidine Moieties. *Anal Chem* **2012,** *84* (4), 2025-2030.

26. Tong, Q. X.; Lai, S. L.; Chan, M. Y.; Lai, K. H.; Tang, J. X.; Kwong, H. L.; Lee, C. S.; Lee, S. T., High T-g triphenylamine-based starburst hole-transporting material for organic light-emitting devices. *Chem Mater* **2007,** *19* (24), 5851-5855.

27. Kang, X. W.; Chen, S. W., Electronic conductivity of alkyne-capped ruthenium nanoparticles. *Nanoscale* **2012,** *4* (14), 4183-4189.

28. Larkin, P., *Infrared and raman spectroscopy : principles and spectral interpretation*. Elsevier: Amsterdam ; Boston, 2011; p x, 228 p.

29. Creighton, J. A.; Eadon, D. G., Ultraviolet Visible Absorption-Spectra of the Colloidal Metallic Elements. *J Chem Soc Faraday T* **1991,** *87* (24), 3881-3891.

30. Gao, W. Z.; Wang, S. R.; Xiao, Y.; Li, X. G., Synthesis and properties of new luminescent hole transporting materials containing triphenylamine and carbazole units. *Spectrochim Acta A* **2012,** *98*, 215-221.

31. Chen, W.; Pradhan, S.; Chen, S. W., Photoluminescence and conductivity studies of anthracene-functionalized ruthenium nanoparticles. *Nanoscale* **2011,** *3* (5), 2294-2300.

32. Tang, S.; Li, W. J.; Shen, F. Z.; Liu, D. D.; Yang, B.; Ma, Y. G., Highly efficient deep-blue electroluminescence based on the triphenylamine-cored and peripheral blue emitters with segregative HOMO-LUMO characteristics. *J Mater Chem* **2012,** *22* (10), 4401-4408.

Chapter 5

Summary of Research Results

5.1 Conclusions

In order to better understand electron transfer by inter and intrananoparticle systems a number of carbon nanoparticles were produced as well as metal nanoparticles. Using graphene quantum dots, GQDs, from carbon fiber the assessment of aqueous ions and their quenching capacity was conducted with results showing that a particular chemical hardness of 8.50 eV corresponding to nickelous ions were optimum for quenching. This was contrasted with nitrogen doped graphene quantum dots, nGQDS, which were most optimally quenched by 7.70 eV mercuric ions. Both showed strong sensitivity to the ions sensing concentrations as low as $1.6x10^{-6}$ M in an unoptimized system. Possible bias was observed with the nGQDs toward larger ions which could be of use if a sensor was developed. Both optimum hardness as well as size would be valuable factors. EDTA was observed to recover photo emission from the GQDs clustered around the same hardness values observed to quench. Also very intriguing results were observed for aluminum ions and a few others, with concentration dependent behavior that pointed to multiple quenching sites. The photo excitation values are also noted to follow that of the quenching hardness with bluer excitation values corresponding to harder quenchers.

Carbon nanoparticles were synthesized from soot produced by burning sp^2 enriched fuel, toluene and pyridine. Nanoparticles produced from this soot were observed to have Raman, XPS, and FTIR signatures of graphene. Along with considerable sp^2 character the samples were observed to take on a planer structure as observed by AFM with modal thicknesses. Doping of the nanoparticles was

undertaken by burning pyridine dissolved in with the toluene. Dopant levels were observed at ~3 % with interesting ramifications for solvent sensing. The enriched pyridinic and pyrolic content of the nanoparticles were possibly stabilized by nitrogen containing solvents and so showed dramatic increases in conductivity for nanoparticle films produced there from. The redox hopping mechanism may be added by an annealing mechanism allowing the particles to make better contact with one another. The response of the nanoparticle film for the nitrogen doped sample to isopropanol is a good indicator of this. Slight sensitivity to chloroform was also observed for the nitrogen doped sample.

To probe smaller systems of electron transfer metal nanoparticles were synthesized with donner acceptor moieties covalently bound to the nanoparticle core. Effective intraparticle charge delocalization was exhibited by observing electro-photochemical characteristics consistent with conventional molecular dyads. Which are normally constructed of a donating and accepting unit bound within the same organic molecule. Ruthenium nanoparticles functionalized with both with 4-ethynyl-*N*,*N*-diphenylaniline (EDPA) and 9-vinylanthracene (VAN) showed effective mixing of the π electrons between the moieties. Photoelectrochemcial studies showed the bound triphenylamine's well-defined voltammetric peaks in the dark could be diminished with UV-photoirradiation showing delocalization. The effect was even more pronounced with the addition of moieties of anthracene which could act as more permanent charge centers. The rapid transfer of photogenerated electrons donors to acceptors is most likely facilitated by the conjugated metal-ligand bonds and hence

low interfacial contact resistance. This is a unique property ideally suited to solar cells and light emitting diodes.

These results improve upon current understanding of electron transfer systems, by looking at under which conditions are required to facilitate motion from nanoparticles to ions. Ideal chemical hardness values could aid in the development of new ions sensors. Solvent vapor detectors could also be improved by functionalizing carbon nanoparticles that have ideal redox hopping sites for the needed analyte. Taking into account the possibility of annealing effects, which may need to be considered. Lastly photosystems might be improved by utilizing conjugated systems with donor acceptor dyads to facilitate electron transfer in systems of nanoparticle size, larger than those before developed.

5.2 Future Work

Of future interest are a number of possible experiments expanding on the works that have been outlined here. Avenues to further each project are listed here.

For the aqueous ion sensing project further tuning the GQDs such that a variety of ions can be sensed by PL methods, might elucidate functional groups that interact best with larger ions and which interact with smaller ions as well as tune the optimal hardness.

The solvent vapor sensing work might be aided by testing 2-butanol, which is a close analog of isopropanol. Also thiol compounds would be of interest as they are irritants. Already attempted were smaller ring systems with nitrogen, pyrrolidine and pyrrole but nether evaporated properly. However, but other nitrogen containing

compounds would also be intriguing to explore. Possibly the two trends could be better elucidated through further observation.

Lastly, it would be interesting to more thoroughly observe the donor acceptor diads by looking at both the donor's redox peak as well as acceptor. Anthracene's redox peak however is too negative to be easily observed. Acridine displays a redox peak closer to zero volts and could still act as an electron acceptor.